Optical Signal Generation, Stabilization, and Manipulation in Broadband Silicon Photonics

by

Emir Salih Magden
B.S., Tufts University (2012)
S.M., Massachusetts Institute of Technology (2014)

Submitted to the Department of Electrical Engineering and Computer Science
in Partial Fulfillment of the Requirements for the Degree of

Doctor of Philosophy in Electrical Engineering and Computer Science
at the

MASSACHUSETTS INSTITUTE OF TECHNOLOGY
February 2018

Signature redacted
Author...
Department of Electrical Engineering and Computer Science
November 21, 2017

Signature redacted
Certified by...
Michael R. Watts
Associate Professor of Electrical Engineering and Computer Science
Thesis Supervisor

Signature redacted
Certified by...
Leslie A. Kolodziejski
Professor of Electrical Engineering and Computer Science
Thesis Supervisor

Signature redacted
Accepted by...
Leslie A. Kolodziejski
Professor of Electrical Engineering and Computer Science
Chair, Department Committee on Graduate Students

Optical Signal Generation, Stabilization, and Manipulation in Broadband Silicon Photonics

by

Emir Salih Magden

Submitted to the Department of Electrical Engineering and Computer Science
on November 21, 2017
in Partial Fulfillment of the Requirements for the Degree of
Doctor of Philosophy in Electrical Engineering and Computer Science

Abstract

Together with the increasing number of applications in vastly different parts of the electromagnetic spectrum, more versatile, stable, and capable light generation and manipulation techniques are required in integrated photonics. In this thesis, using CMOS fabrication capabilities, and a single layer back-end deposition process, CMOS-compatible lasers are developed using aluminum oxide as the host medium. First, a low temperature deposition process is detailed, and erbium-based lasers are demonstrated in the C-band. Then, thulium is studied and characterized as a dopant for applications at longer wavelengths. On-chip frequency stability issues are addressed by investigating the thermo-optic characteristics of various CMOS-compatible media. Negative thermo-optic coefficient of titanium dioxide is utilized to compensate for the all-positive thermal index shifts in the Si/SiN waveguide platform. An athermal resonator with resonances that exhibit ultra-low thermal shifts is created and used to stabilize a continuous-wave laser. Compared to a conventional SiN resonator, the athermal resonator is shown to significantly reduce the frequency noise of a locked laser. Switching to design-based solutions, the concept of spectrally-selective waveguides that can spatially confine the mode depending on the wavelength are demonstrated for the first time. The spectrally-selective waveguides are then used to design and demonstrate the first on-chip transmissive dichroic filter with the sharpest roll-offs to date. Finally, directional coupler based solutions are studied to address wavelength selectivity for octave-wide signals, and propose designs for ultra-wideband couplers.

Thesis Supervisor: Michael R. Watts
Title: Associate Professor of Electrical Engineering and Computer Science

Thesis Supervisor: Leslie A. Kolodziejski
Title: Professor of Electrical Engineering and Computer Science

ACKNOWLEDGEMENTS

The years that I spent at MIT has been one of the most important periods of time in my life. Working with a great team of advisors, mentors, and colleagues on various projects was an amazing experience. I have many people to thank for the intellectual environment that was made possible for all the work presented in this thesis.

To begin with, I would like to express my gratitude to my co-advisor Prof. Michael Watts who has enabled all of the research in my thesis. Throughout my time here, we had more large research grants than many other groups, making it possible to work in an extremely well-equipped lab with a great team. Mike has been a tremendous help in my academic development and understanding the important problems in research. Through Mike's vision and passion, I also developed a great deal of skills in coming up with convincing answers and arguments to the intellectual problems we worked on. This is not a skill that one specifically sits down to teach or learn. One only learns this after being in our group for a long time and after working on the diverse projects we had. I don't think I would have been able understand how key this is if I had been in any other group. I am extremely luckly and thankful to have worked with Mike.

My career at MIT would not have been the same without my co-advisor Prof. Leslie Kolodziejski. Leslie has been one of my most valuable resources at MIT since my very first day. With her wealth of knowledge in the optical materials space, she has helped me understand deposition processes to a level that I could not have achieved anywhere else. I am grateful for her wisdom that led me many solutions even at the most challenging moments. She has also taught me many other research and management skills to become efficient at what I do extending well beyond lab work or simulations. These are valuable skills that one needs in a stressful environment, and those that I will rely on throughout the rest of my career. I am grateful to have had such a wonderful advisor, mentor, and an amazing resource.

I consider myself extremely lucky to have worked with a pioneer like Prof. Erich Ippen. His experience, valuable comments, amazing insight, and wonderful company has helped me get through some of the toughest challenges I faced during my PhD. His solutions to many of our problems that we discuss in our meetings have proven to be extremely useful, and intellectually stimulating. His encouragement and suggestions for all my thesis work and life beyond MIT are definitely key highlights from the time I spent here. I thank him greatly for all the valuable discussions and comments on thesis work and many of my papers.

I would also like to extend my gratitude to Prof. Franz Kaertner who has made himself available despite the time difference and his group of 50 other researchers. He has continually amazed me with his work ethic to a level that I can only aspire to mimic with my own group of students. I benefited immensely from his devotion to helping us and sharing his experience on an extremely wide range of technical fronts. I am thankful for all his help, and grateful to have worked with an amazing mentor like him.

I would like to thank all my professors and mentors at MIT and Tufts who have enabled me to achieve the work I have done so far. I especially thank Prof. Dirk Englund, Prof. Qing Hu, Prof. Peter Hagelstein, Prof. Terry Orlando, Prof. Rajeev Ram, Prof. Karl Berggren, Prof. Thomas Vandervelde, Prof. Hugh Gallagher, and Prof. Roger Tobin for everything they taught me in and outside of class. I am deeply grateful to have taken classes from and worked with such an amazing group of people.

MIT has been such a great place for not only doing research, but learning from people around me. Our previous group members have a special place for all they have helped me achieve. I would like to specifically acknowledge Prof. Jonathan Bradley, Dr. Gale Petrich, Dr. Diedrik Vermeulen, Dr. Zhan Su, Dr. Katia Shtyrkova, Dr. Purnawirman, Dr. Michael Peng, Dr. Michele Moresco, Dr. Erman Timurdogan, Dr. Ehsan Hosseini, Dr. Ben Moss, Dr. Jie Sun, Chris Poulton, and Matt Byrd for all their help in my experiments as well as for making my time at MIT fun and exciting. I would also like to thank our current group members including Dr. Alfonso Ruocco, Dr. Neetesh Singh, Dr. Ming Xin, Patrick Callahan, Kousuban Ravi, Nanxi Li, Manan Raval, Jelena Notaros, and Milica Notaros for all the intellectual discussions we had, and also for making my MIT career more fun than it would otherwise have been.

This work would not have been possible without the assistance of our lab staff and members of other groups including Gary Riggott, Kurt Broderick, Paul McGrath, Di Zhu, Tim McClure, Libby Shaw, Charlie Settens, Teresa Avila, Stacy McGrath. I am also thankful for the assistance of our department and graduate office staff including Janet Fischer, Kathleen McCoy, Alicia Duarte, Claire Benoit, Dave Foss, Bill Adams, and Bill Tilden who helped me with all my administrational requests and requirements.

None of this would have been possible without the continual support of my parents. They gave me the encouragement and motivation I needed throughout my studies and always supported me. Their dedication has made it possible for me to become the person I am today. I am grateful for all they have done for me, and all that they have enabled me to do. I would also like to thank my parents-in-law and sister-in-law for supporting me throughout this journey, and the environment they provided for me.

Before starting a PhD program, most people have some expectations of challenges to be faced and how difficult of a time it can really be. However, what most people do not realize is that PhD is a period of time where other people, especially your loved ones, constantly have to make sacrifices for you. And for that, I have my wife to thank, for this work would not have been possible without her love, support, and sacrifice.

Dedicated to my lovely wife Zeynep

CONTENTS

LIST OF TABLES

LIST OF FIGURES

LIST OF ACRONYMS

AWG	arrayed waveguide grating
BW	bandwidth
CMOS	complementary metal-oxide-semiconductor
CMP	chemical mechanical polishing
DC	directional coupler
DFB	distributed feedback
EDFA	erbium-doped fiber amplifier
EME	eigenmode expansion
FDE	finite difference eigenmode
FDTD	finite difference time domain
LIDAR	light imaging, detection, and ranging
MMI	multi-mode interference
MZI	Mach-Zehnder interferometer
OSA	optical spectrum analyzer
PD	photodetector
PDH	Pound-Drever-Hall
PECVD	plasma enhanced chemical vapor deposition
PID	proportional-integral-differential
PML	perfectly matched layer
PVD	physical vapor deposition
RBS	Rutherford back-scattering
RF	radio frequency
SC	supercontinuum
SEM	scanning electron microscope
SHG	second harmonic generator
SOI	silicon-on-insulator
TE	transverse electric
TEC	thermo-electric cooler
TM	transverse magnetic
WDM	wavelength division multiplexer
WG_A	waveguide A
WG_B	waveguide B
XPS	x-ray photoelectron spectroscopy

1 INTRODUCTION AND MOTIVATION

This chapter introduces some of the initial driving forces behind the advent of silicon photonics, discusses the design and testing cycle, and outlines how the thesis is organized into the subsequent chapters.

1.1 The Silicon Photonics Technology

Most of the information-based technology we know today has stemmed from one of the most influential innovations of all time in 1948: the transistor. After the demonstration of the first integrated circuit with two transistors in 1959, with fast-paced improvements in complementary metal-oxide-semiconductor (CMOS) technology, transistor gate lengths have shrunk from micrometer scales to the 14 nm nodes we now have in 2017. As a result of this integration density, standard CPUs today have billions of transistors where every single one performs within specification. Due to the profound impact of this fabrication quality on device performance, most state-of-the-art foundries have automated production lines where minimal human interference is required for most mass-produced wafers. As a result of this scaling

(Moore's Law), the manufacturing cost per transistor has also reduced dramatically to about a few microcents per transistor today.

Another method the CMOS industry has used to successfully increase computation speed is to use circuits with faster operating clocks. Similar to the integration density, clock speeds have also seen dramatic increases from just a few MHz around the beginning of the 1980s to the over 4 GHz clocks we have in modern microprocessors today. The increased clock speeds have also resulted in increased power and consequent cooling requirements. Therefore, processors consisting of multiple cores have been integrated in silicon chips where appropriately designed software applications can parallelize computation processes. When multiple components of a central processor are performing simultaneous tasks, the need for communication between different processor cores or various registers is also highly increased. As a result, running a multi-threaded computation does not simply decrease the computation time by a factor equal to the number of threads used. This latency in communication and the resulting bottleneck have been some of the initial driving forces behind the silicon photonics technology.

While addressing the increased communication bandwidth requirements in microprocessors, it is also important to keep power consumption to a minimum, and establish communication channels with minimum noise. Optical communication technologies frequently used in rack-to-rack interconnects can achieve low-power and low-noise data transmission in typical data centers today. Silicon photonics as a discipline aims to integrate functionalities required for optical communications just like in rack-to-rack data transmission, as well as to introduce novel on-chip capabilities for sensing, display, and computation applications.

Making use of the already developed CMOS fabrication capabilities, the photonics industry is currently going through the miniaturization trend the electronics industry went through in the second half of the 20th century. This is clearly seen in the comparison shown in Figure 1-1 where the cm-sized arrayed waveguide grating is compared to what is possible today with the integration density provided in the silicon-on-oxide (SOI) CMOS platform. With devices that can bend and route optical signals with physical dimensions comparable to the wavelength of light, device footprint has decreased by over 8 orders of magnitude. Partly due to the high index contrast between Si and its native oxide SiO_2, we now have easy access to foundries with capabilities that can fit hundreds of devices within a 10 mm^2 footprint.

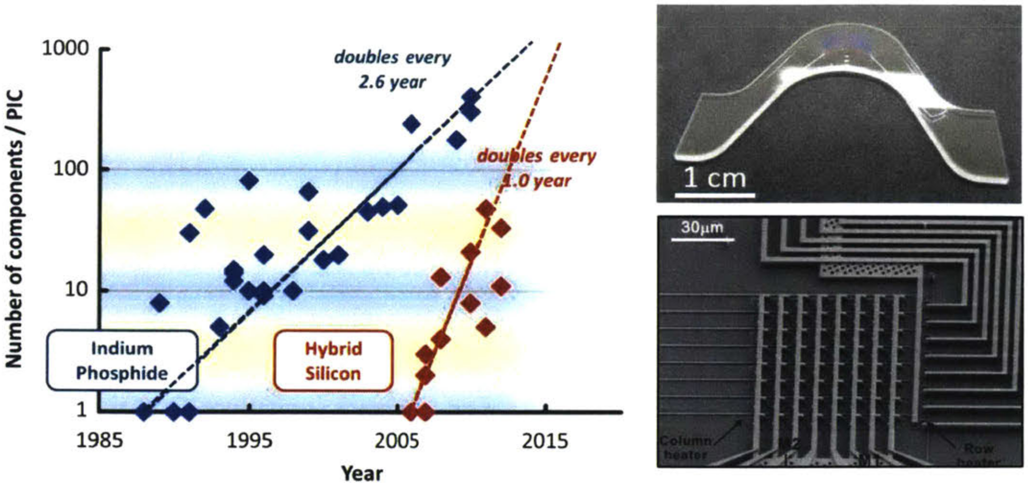

Figure 1-1: Scaling trends in integrated photonics technologies with two examples: A cm-scale AWG from the 1990s, and a collection of integrated phase shifters from a recent SOI fabrication run [1]

Another set of advantages stems from the material properties of Si itself. As a semiconductor material, one of the most useful properties of Si is that it can be doped in order to modify its electrical characteristics. With precise implantation technologies, doped Si allows us to integrate components such as resistors, diodes, and capacitors within silicon photonic devices, and control local electrical variables such as electric field and current density. With the capability of precise electrical control and readout, we are able to design and implement devices that can transduce information between the optical and electrical domains. Combined with the high refractive index contrast available in the SOI platform, the electro-optic and thermo-optic effects can be amplified in geometries where the guided optical mode can be geometrically confined to regions that have efficient electrical and thermal control.

When combined with the precise waveguide fabrication technology, these capabilities have allowed the photonics community to demonstrate many devices including low-loss waveguides, heaters, resonators, filters, modulators, detectors, phase shifters, etc. Some examples are shown in Figure 1-2 highlighting the fabrication capabilities and what is possible with the CMOS photonics technology today.

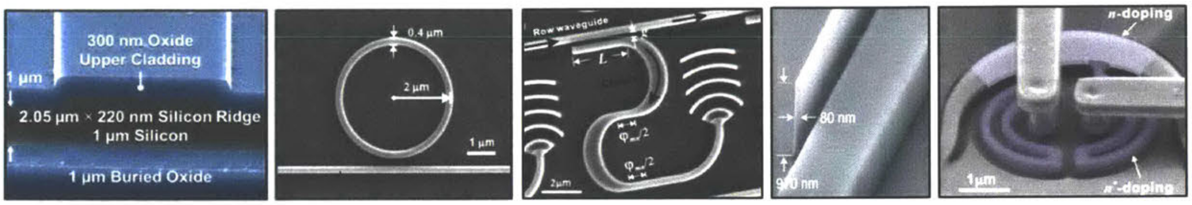

Ultralow-loss Si Resonator | 2 μm Radius Ring Resonator | Phase Shifter & Antenna | Polarization Splitter | Tunable Thermo-Optic Shifter

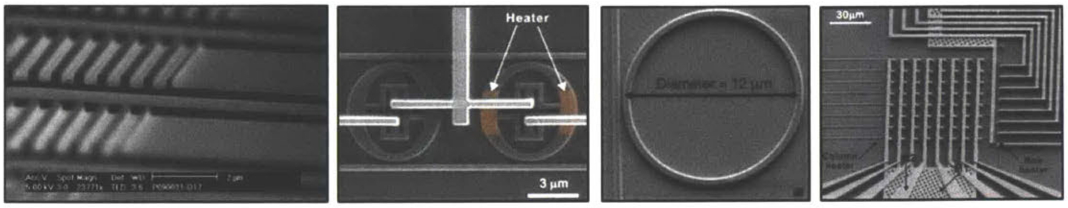

Grating Coupler | Tunable C-Band Filters | Electro-Optic Modulator | Active Phased Array

Figure 1-2: Example silicon photonic devices fabricated using SOI technology in a CMOS foundry [1-6]

1.2 The MIT Silicon Photonics Platform

For most of the fabrication in our projects, we have collaborated with the College of Nanoscale Science and Engineering (CNSE) at SUNY Polytechnic University. Working together with collaborators from UC Berkeley, we developed a platform that can integrate optical and electronic devices on the same die with the use of a wafer-bonding process. By making use of several layers of p- and n-type dopants and the available growth of Ge on Si, this platform makes it possible to actively control devices by the aforementioned electro-optic and thermo-optic effects. In addition to the Si and SiN layers used for passive waveguiding in the platform, we also added a back-end-of-line deposition process for rare-earth doped aluminum oxide for lasers and amplifiers. The fabrication stack is designed in a way that the only step after the CMOS processing is the deposition of the aluminum oxide layer into the previously etched trenches; and no further patterning or etching steps are required. A diagram of the process layers are shown in Figure 1-3. For the Si layer, there are full and partial etch layers that allow for finer control of light. There are multiple SiN layers with different thicknesses designed to assist in guiding light in and out of the Si waveguides, on- and off-chip coupling, and for lasers and amplifiers where the lateral mode guidance depends on the nitride stack. Two metal layers and vias are placed for interacting with the electrically-controlled devices. Having multiple metal layers allows design flexibility in wiring pads and contacts to the devices, which is especially useful from a system perspective when integrating more complicated circuits where a large number of electrical control signals are required.

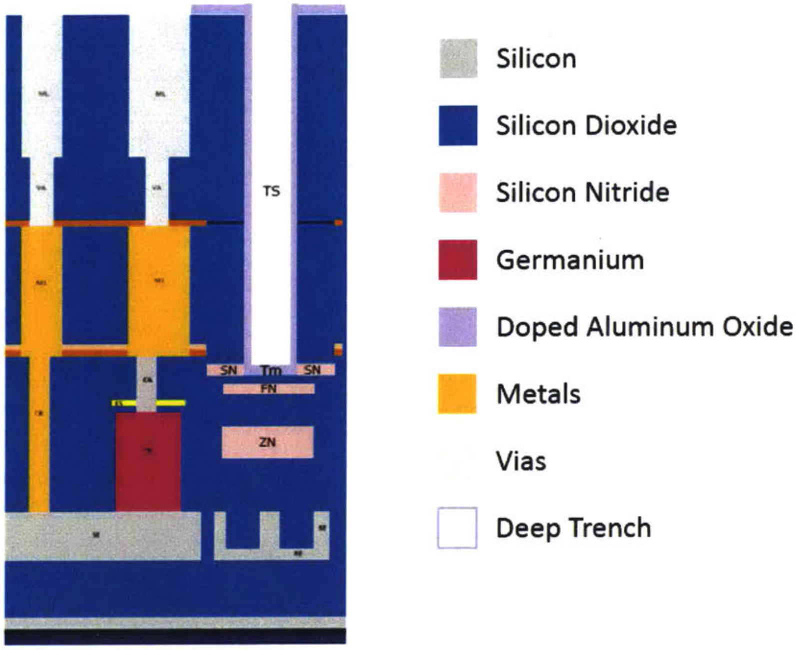

Figure 1-3: Diagram showing the cross-section of process layers for integrated photonics components showing layers for waveguiding and electrical control as well as trench for back-end-of-line aluminum oxide deposition

The lasers and amplifiers in this platform only make use of the SiN layers and deep trench etch for the back-end deposition of aluminum oxide. For rapid testing of these laser structures, there is therefore no need to integrate metal, via, or sometimes even Si layers into the process stack. This “SiN only” or “SiN and Si only” designs help improve the turnaround time of the fabrication process, and eliminate errors that might arise from fabrication complexity of the added layers. During the time that I spent at MIT, we have prepared many masks of both the “SiN-only” type, and of the fully integrated type. The design process for each one of these masks starts with specifications of design goals and target performance metrics. Then, using finite-difference eigenmode solutions (FDE/modesolver), finite-difference time-domain (FDTD) simulations, the eigenmode expansion (EME) method, and analytical coupled-mode theory, devices are designed and simulated to meet these specific metrics. After the device design is complete, layout is done using Cadence tools, although many other commercial layout packages exist. During this stage, it is a good idea to parametrize the devices as much as possible in order to streamline further system design tasks. Before the masks are ready to be sent for fabrication, they look like the examples shown below in Figure 1-4.

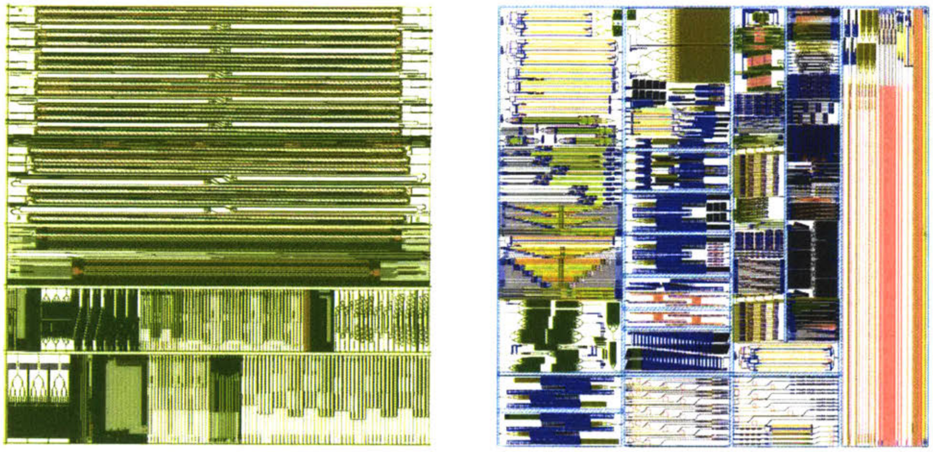

"SiN and Si only" Build Example

Fully Integrated Build Example

Figure 1-4: Examples of two types of masks prepared sed for silicon photonic design. "SiN and Si only" masks do not include electrically-controlled devices, whereas the "Fully Integrated Builds" have complete electro- and thermo-optic capability.

The last fabrication step is the back-end-of-line deposition of rare-earth doped aluminum oxide within the Microsystems Technology Laboratories and Nanoprecision Deposition Laboratory at MIT using reactive sputtering tools made by manufacturers AJA and KJL. This is a process that had been developed earlier on [7] and has been adapted for use in our platform due to low-noise and narrow linewidth performance of the resulting rare-earth-based lasers.

Fabricated materials, devices, and systems are tested for their performance using various optical and electronic equipment. Like most integrated photonics technology today, many devices and systems designed throughout my time at MIT have required multiple iterations of the design/fabricate/test phases. As expected, many devices still have room for improvement that can be realized by learning from previous results and slightly modifying the designs. These details are provided together with concluding remarks at the end of each chapter in relation to the material discussed in that chapter.

1.3 Organization of This Thesis

This thesis revolves around the development of new capabilities in the aforementioned silicon photonic platform with the use of new materials, novel device design, and system-level integration. Consequently, just like many photonic development efforts, the following chapters are presented in material→device→system order. The first two chapters focus on material-based solutions for integration of lasers and characterization of erbium- and thulium- doped gain media. The next chapter discusses the development and use of titanium dioxide from a device perspective in order to address thermal stability issues. The last two chapters focus on more advanced design techniques for spectral splitting/combining applications by making use of coupled-mode theory of guided optical modes.

In Chapter 2, the development of a new reactive sputtering method is discussed with the use of the substrate bias. The investigation focuses on the effects of deposition variables such as temperature and substrate bias on the resulting film quality. This chapter's focus is on the development of erbium doped aluminum oxide. Then, using a periodically varying structure, a distributed feedback laser is designed and fabricated. Laser characterization and threshold/efficiency performance metrics are presented. Then, the low temperature deposition is utilized for creating a fully-integrated on-chip communications link.

In Chapter 3, I study the erbium- and thulium- doped gain media in more detail. I develop a frequency-domain method to characterize not only the lifetime or the absorption cross-section in these media, but the full transfer function that models the rate equations. I first verify the model in doped silica fibers, and then use the model to characterize the newly developed thulium-doped aluminum oxide material.

In Chapter 4, I utilize the reactive sputtering technique to introduce titanium dioxide into our fabrication platform to make use of its negative thermo-optic coefficient. By adding a thin titanium dioxide layer, I create thermally stable reference resonators, and show effects of the layer thickness on the athermal behavior. I then lock an external laser to the athermal reference and characterize the phase noise of the resulting locked signal to evaluate the performance of the athermal resonator.

In Chapter 5, I review the basics of coupled mode theory and study how the power is distributed in a pair of coupled waveguides. Utilizing the findings here, I design a new type of waveguide cross-section in Si in order to spectrally separate a wide range of wavelengths. Using the novel spectrally-selective waveguides, I design and demonstrate the first broadband dichroic filter on-chip.

In Chapter 6, I use directional coupler-based designs to create more broadband couplers that can be used for wavelength splitting/coupling functionalities. I first investigate the spectral dependence of a directional coupler. Then, using an unbalanced interferometer idea, I create an ultra-broadband spectral splitter design that can be used for applications involving wideband signals like a frequency comb or a supercontinuum source.

2 CMOS-COMPATIBLE ERBIUM-DOPED LASERS

In this chapter, I first review the recently developed lower temperature deposition process for Al_2O_3:Er^{3+}, and characterize the resulting thin film for its optical characteristics. Then, I design, fabricate and test lasers that can operate using the lower temperature deposited gain medium. Finally, I design and test a system that can monolithically integrate the lower temperature laser, a modulator, a filter, and a detector on a Si chip for the first time, and characterize the system response of this fully-integrated communications link.

2.1 Lower Temperature Deposition of Amorphous Aluminum Oxide

The use of rare-earth-doped glass media in integrated optics applications has been studied for amplification and generation of light since its first demonstration in 1991 [8]. Of the numerous possible host glasses for rare-earth-dopants, the interest in amorphous aluminum oxide (Al_2O_3) has many reasons. Al_2O_3's higher refractive index than those of similar host media such as silica, phosphate glass, or fluoride glass enables higher integration density of optical components [9-12]. Al_2O_3 also provides good rare-earth ion solubility [13], and is more easily fabricated via physical vapor deposition techniques as compared to crystalline hosts that require epitaxial growth [14]. Moreover, smaller thermal and excitation-induced refractive index changes help provide more stable gain [15-18], making rare-earth-doped Al_2O_3 a potential gain medium with better noise performance than that of III-V semiconductors [19-22]. The wide gain-bandwidth of various rare-earth dopants also helps to achieve wavelength tunability and design flexibility throughout their emission spectra [23-26]. Such advantages have led to recent demonstrations of erbium-doped Al_2O_3 (Al_2O_3:Er^{3+}) waveguide amplifiers [27], as well as high-power, integrated continuous-wave and pulsed lasers [28-30].

For a waveguide material having such promising gain characteristics, a reliable and robust fabrication process is crucial. So far, the reactive radio frequency (RF) magnetron sputtering in a mainly argon (Ar) environment has been found to be the most reliable due to its relatively high-rate, OH-free deposition on large area substrates. However, although background optical losses as low as 0.11 dB/cm have been reported in undoped Al_2O_3 films that were deposited with this method, a deposition temperature of 550 °C was required in order to reduce the background loss [7]. Previously, it has been empirically shown that post-processing of CMOS wafers at temperatures over 425 °C to 525 °C can compromise the integrity of the metal contacts and vias by resistance increase and dopant activation [31-33], as shown in the examples in Figure 2-1.

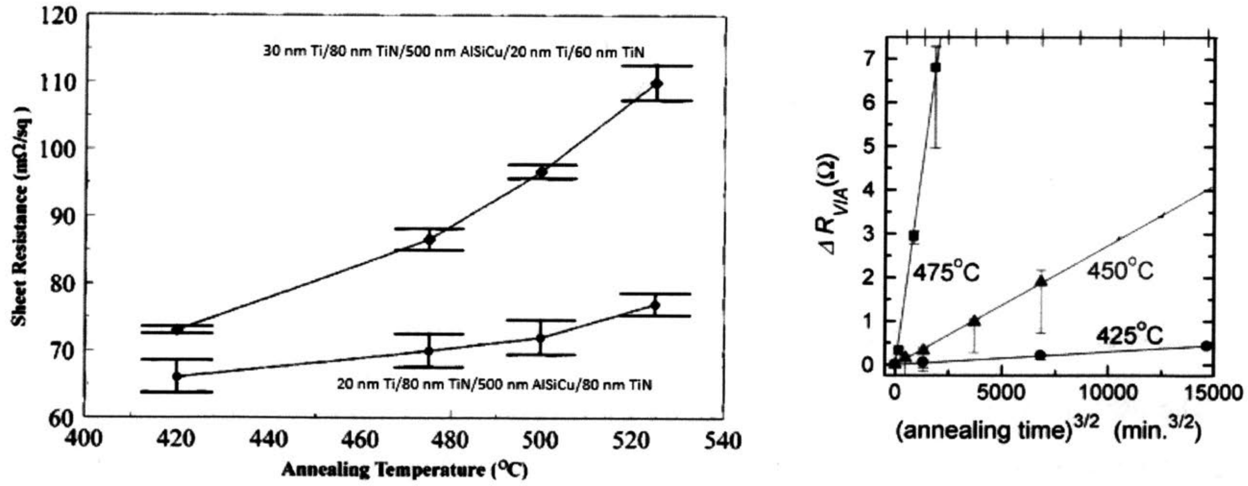

Figure 2-1: Resistance increase in various CMOS contacts and vias with post annealing temperatures over 425 °C, reproduced from [33] and [32]

This degradation in contacts and vias significantly limits the performance of an integrated optical system, where active devices such as modulators, filters, and detectors inherently require low-resistance contacts for high-speed operation. Therefore, for full monolithic integration of

CMOS and photonic structures on the same die, it is essential to develop a deposition procedure that can reliably yield low loss Al_2O_3 films at lower temperatures within CMOS post-processing thermal budgets. One way to improve the sputtered film quality is to use a substrate bias, where the substrate is bombarded by Ar^+ ions during deposition. This technique has been shown to enhance optical transmission, and improve film surface quality for other dielectrics such as TiN [34]. However, the effect of substrate bias on the Al_2O_3 film quality at CMOS-compatible temperatures has not been studied prior to the beginning of this project.

Here, we first investigate how the application of a substrate bias can compensate for the reduced deposition temperatures for reactively sputtered Al_2O_3. We determine the optimum fabrication parameters that yield the Al_2O_3 film with the lowest optical propagation loss, while still maintaining backend CMOS-compatibility. Using these parameters, we fabricate and characterize Al_2O_3:Er^{3+} films for use in active photonics devices. We then design, fabricate, and characterize a distributed feedback (DFB) laser that uses the newly developed Al_2O_3:Er^{3+} as its gain medium. Finally, we integrate the DFB laser together with other active silicon photonic components including tunable filters, modulators, and detectors and create a fully-integrated communications link on-chip.

2.2 Review of Al_2O_3 Material Development and Optimization

The Al_2O_3:Er^{3+} gain medium was developed just before the beginning of the thesis work outlined here, and was deposited using a Kurt J. Lesker Lab 18 thin film sputtering system with magnetron sputtering guns and RF power supplies. The system was consistently kept under vacuum with a base pressure of 10^{-7} Torr; and samples were loaded with the use of a load lock. The ability to separately control the target and substrate shutters allowed for a more reliable deposition process, yielding films with consistent quality and thickness. First, the undoped Al_2O_3 film was studied. The films were reactively sputtered from an Al target with 99.999 % purity in an Ar/O_2 environment of 3-5 mT process pressure as regulated primarily by the Ar flow rate. O_2 was separately introduced and the flow rate was kept around 4.0 - 4.3 sccm, after which the bias voltage on the Al target started to decrease significantly [35]. This allowed for high deposition rates (5 - 6 nm/min) of optical quality, stoichiometric Al_2O_3, without fully oxidizing the Al target. With this O_2 flow, an RF power of 400 W was applied to the Al target, resulting in a bias voltage of 210 V.

The optical quality of the sputtered Al_2O_3 films was characterized using a Metricon 2010/M prism coupling system with lasers at 633 nm, 829 nm, and 1550 nm. Film thickness, index, and propagation losses were measured using slab waveguides formed by 1 μm thick Al_2O_3 films deposited on thermally oxidized Si/SiO_2 substrates. The thermal oxide thickness was 6 μm. To obtain the optimum deposition parameters for the best optical quality Al_2O_3, a set of depositions was performed at temperatures ranging from 125 °C to 450 °C, and with substrate biases ranging from 0 W to 90 W.

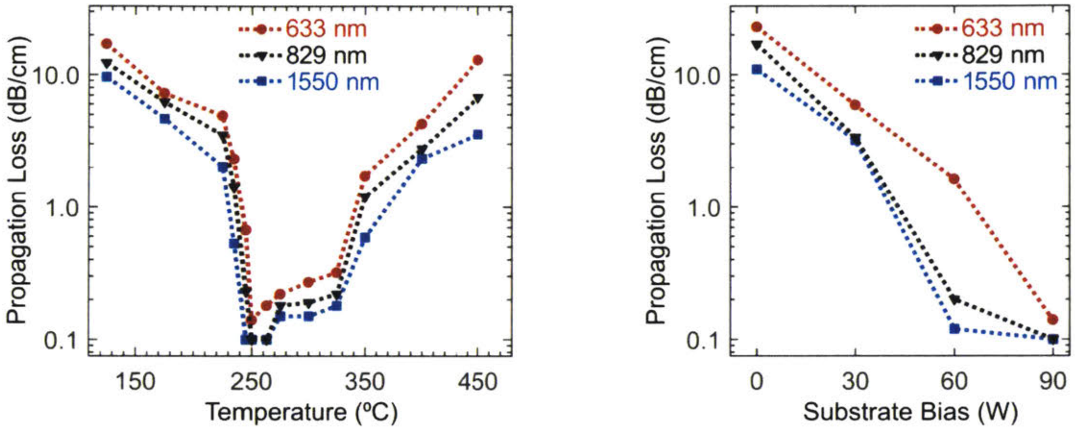

Figure 2-2: Dependence of propagation loss in the Al_2O_3 thin film on deposition temperature and the substrate bias. Temperature dependence on the left is with 90 W of substrate bias. Bias dependence on the right is at 250 °C deposition temperature.

Plotted in Figure 2-2 are propagation losses measured from films that were deposited with different substrate temperatures and different substrate biases. Films with the lowest optical losses were obtained at an optimum temperature of approximately 250 °C, and with the highest possible substrate bias of 90 W. The measured propagation loss in the Al_2O_3 film using these ideal parameters was as low as 0.1 dB/cm at 1550 nm where the refractive index was $n_{Al2O3} = 1.578$. At temperatures significantly below or above 250 °C, or with a smaller substrate bias, propagation losses over 10 dB/cm were measured.

At lower temperatures and insufficient substrate biases, the increased loss can be explained by the reduced surface mobility, which is known to cause clusters and voids in the deposited layer [7]. This is corroborated by the surface roughness measurements from films that were deposited with 0 W and 90 W of substrate biases at a temperature of 250 °C. According to the atomic force micrographs in Figure 2-3, for the film deposited without a substrate bias, a root mean square roughness (R_q) of 3.34 nm is obtained over a 1 μm^2 area; and a rough surface morphology is observed. In contrast, when 90 W of substrate bias is used, the surface roughness is reduced by almost an order of magnitude to $R_q = 0.35$ nm, providing a much smoother surface that can help achieve lower propagation losses. For films deposited at temperatures higher than 250 °C, R_q remained below 0.6 nm, indicating no significant contribution to the observed optical losses.

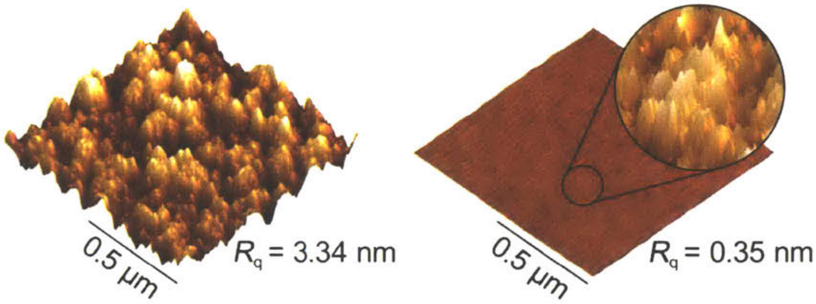

Figure 2-3: Atomic force micrographs of films deposited with no substrate bias (left), and 90 W of substrate bias (right)

The increased losses for temperatures higher than 250 °C can be explained by the enhanced surface mobility of the sputtered molecules [36], which can lead to formation of Al_2O_3 nanocrystals. Previously, nanocrystalline structure formation has been observed at temperatures much below those required for poly- or single-crystalline formation. Examples include nanocrystals synthesized at 280 °C for aluminum europium oxide ($(Al_{1-x}Eu_x)_2O_3$) [37], and sputtered at 200 °C and room temperature for tungsten oxide [38] and indium zinc oxide [39] respectively. Consequently, the application of substrate bias in combination with an increasing deposition temperature above 250 °C can lead to nanocrystal formation in the sputtered Al_2O_3 films. Increased optical losses at higher temperatures can be attributed to scattering from these nanoscale boundaries between the nanocrystals formed.

2.2.1 Refractive Index Measurements

In addition to achieving low loss at the lasing wavelengths, it is also crucial to determine the refractive index of the fabricated film precisely. It was previously mentioned that the prism coupling measurements yielded a refractive index of $n_{Al2O3} = 1.578$ for the lowest-loss film. However, measurements showed that the index depended heavily on the amount of substrate bias applied. Comparing films deposited with different amounts of substrate biases, we characterized the percentage of constituent atoms in the sputtered film by using an X-ray photoelectron spectroscopy (XPS) tool. Results are summarized in Figure 2-4. It was discovered that the difference in the refractive index of the films with and without substrate bias was correlated to the amount of Ar found in the films. For instance, with the use of a 90 W bias, approximately 3 % Ar was incorporated into the film. The refractive index was found to also decrease by approximately 3 % to 1.58-1.60 (90 W bias) from the nominal values of 1.65-1.67 (no bias). Therefore, the change in refractive index can be attributed to the constant Ar^+ bombardment of the substrate during deposition, which results in small amounts of Ar in the fabricated film.

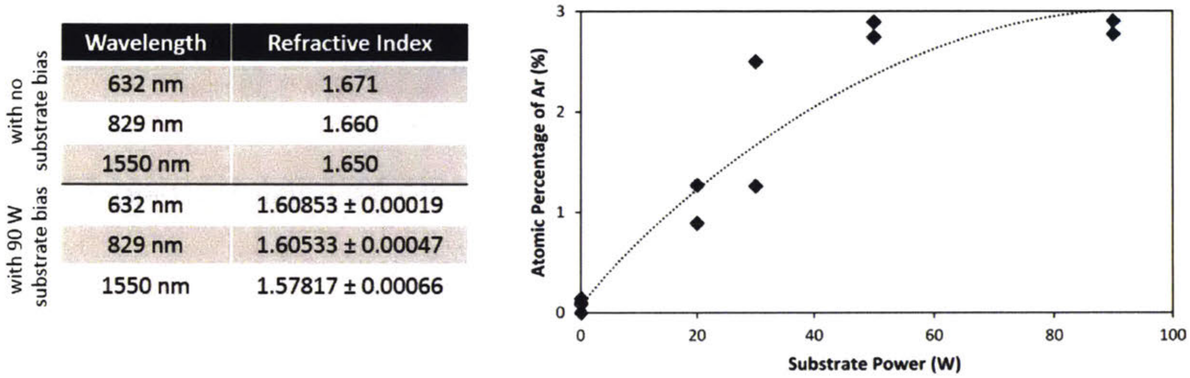

	Wavelength	Refractive Index
with no substrate bias	632 nm	1.671
	829 nm	1.660
	1550 nm	1.650
with 90 W substrate bias	632 nm	1.60853 ± 0.00019
	829 nm	1.60533 ± 0.00047
	1550 nm	1.57817 ± 0.00066

Figure 2-4: Refractive indices of and Ar atomic percentage in films with and without substrate bias. Refractive index variation calculated from measurements of multiple films with 90 W bias. Ar atomic percentage increase corresponds to the observed decrease in the refractive index.

2.3 Characterization of Er^{3+} Dopant Ions

Once the optimum deposition parameters have been determined for the undoped Al_2O_3, doped films were fabricated by means of co-sputtering where an Er and an Al target were simultaneously sputtered. The concentration of Er^{3+} ions was controlled by the bias voltage across the Er target during fabrication. Then, the dopant concentration is extracted from the linear relationship

$$\alpha(\lambda) = \alpha_0 + \alpha_{abs}(\lambda) = \alpha_0 + 10\log(e)\,\Gamma N_0 \sigma_{abs}(\lambda) \tag{2.1}$$

where $\alpha(\lambda)$ is the wavelength dependent absorption in dB/cm, α_0 is the background absorption due to scattering, Γ is the confinement factor in the doped gain medium, N_0 is the dopant concentration per unit volume in cm^{-3}, and $\sigma_{abs}(\lambda)$ is the absorption cross-section in cm^2. The factor of $10\log(e)$ is used to convert from cm^{-1} to dB/cm. Here, α_0 and Γ are assumed to be wavelength independent within the measurement window of 1505 nm - 1575 nm. Shown in Figure 2-5 are the absorption results as functions of wavelength for two films with erbium target voltages of $V_{Er} = 75$ V and $V_{Er} = 60$ V, as measured by the prism coupling method. In this measurement, light from an Agilent 81600B tunable laser source was coupled through a rotating prism to the slab modes in Al_2O_3 films sputtered on Si/SiO_2 substrates. The loss was characterized at each wavelength from the decay of the scattered light intensity along the propagation direction, as measured from a fiber mounted on a motorized stage. Background intensity was subtracted by setting the reading offset to zero when the incident light was turned off. The recorded intensity as a function of propagation length was then analyzed using an exponential fit. In the 1505 nm - 1575 nm wavelength range, the error in the exponential fits remained below $\pm$ 0.1 dB/cm.

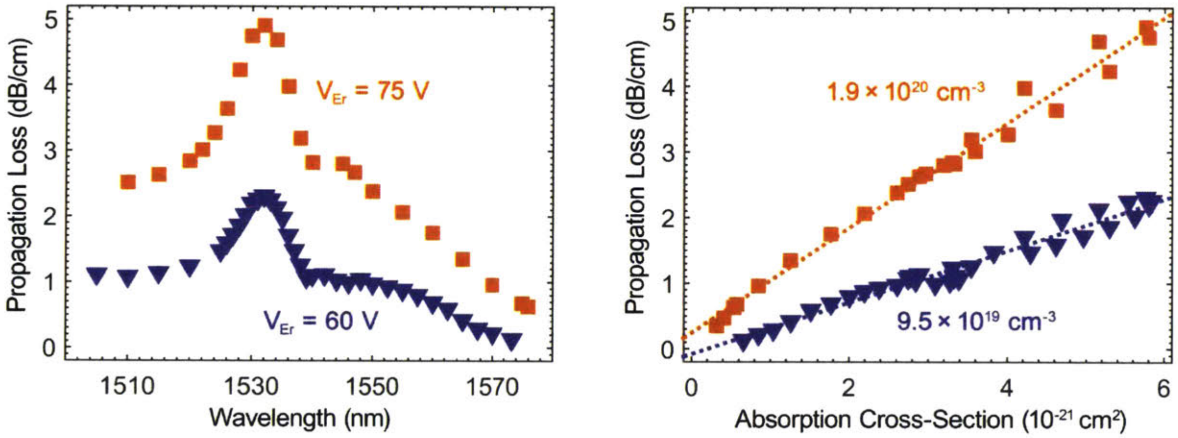

Figure 2-5: Absorption spectra and dopant concentration of films deposited with 60 V and 75 V of bias on the Er target

In order to determine N_0 and α_0, the absorption is replotted on the right in Figure 2-5 as a function of $\sigma_{abs}(\lambda)$, which was previously reported in [7] by Wörhoff et al. Then, according to the model in equation (2.1), each dataset is analyzed with a linear fit, yielding dopant concentrations of $N_{0,75V} = 1.9 \times 10^{20}$ cm^{-3} and $N_{0,60V} = 9.5 \times 10^{19}$ cm^{-3} for $V_{Er} = 75$ V and $V_{Er} = 60$ V respectively. Background losses on the order of 0.1 dB/cm were reliably achieved at both concentrations, as indicated by the vertical intercepts of the linear fits.

2.4 Laser Design and Characterization

After the spectral properties of the newly developed $Al_2O_3:Er^{3+}$ films were characterized, this gain material was used to design an optically-pumped, quarter-wave phase shifted DFB laser. The CMOS process flow and the laser design was planned in a way that allowed the laser to be fabricated in a 300 mm CMOS foundry with the exception of the back-end sputtered $Al_2O_3:Er^{3+}$ gain medium.

2.4.1 Laser Fabrication Process

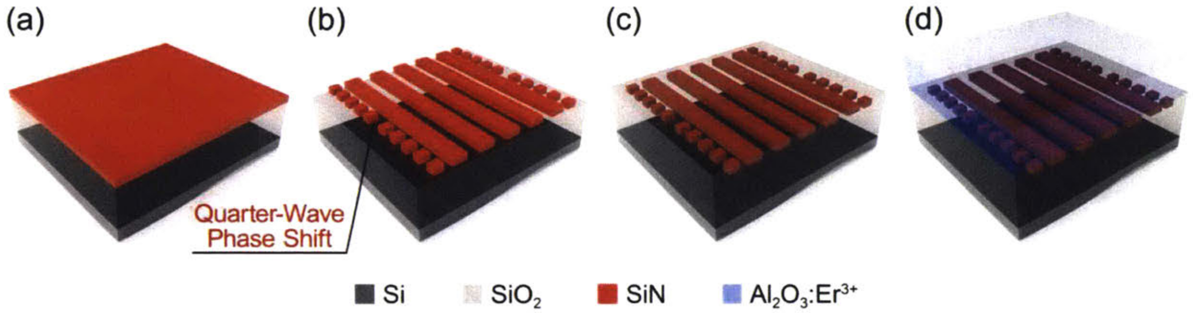

Figure 2-6: Fabrication process flow for the integrated DFB laser

The fabrication process flow is illustrated in Figure 2-6: First, a 6 μm thick layer of SiO_2 and a 200 nm thick layer of SiN were deposited by plasma-enhanced chemical vapor deposition (PECVD) in (a). In order to minimize absorption losses, the plasma conditions were optimized for a low hydrogen content in the deposited layers, while maintaining a high refractive index for the SiN. The SiO_2 and SiN layers were both chemically-mechanically polished (CMP) in order to achieve the accurate final thicknesses, and to reduce scattering losses due to surface roughness. The SiN layer was then patterned using 193 nm immersion lithography and reactive ion etching, creating the waveguide and feedback structures, and the quarter-wave phase shift as shown in (b). After the SiN layer, a thin layer of SiO_2 was deposited using PECVD, for which a final thickness of 100 nm was achieved using CMP, where the resulting structure is shown in (c). Finally, large trenches were etched on the die borders for fiber coupling. After the wafers were diced, the $Al_2O_3:Er^{3+}$ gain medium was deposited as a back-end process as indicated in (d), using the techniques described above.

2.4.2 Guided Modes and Distributed Feedback in the Laser Cavity

The laser was designed using the fundamental modes for both the pump and signal, in order to achieve maximum overlap within the gain medium, and to avoid any potential losses that would be observed by any higher order modes. It is possible to design a SiN waveguide using multiple core segments for more accurate control of the guided mode profiles. The specific goal of this segmented SiN design detailed in Figure 2-7 is to achieve high confinement and overlap of the fundamental transverse electric (TE) signal and pump modes within the gain medium. Compared to a single wider segment, multiple segments of SiN allow the fundamental TE modes to achieve good overlap with the gain medium, while still being laterally confined. These confinement and overlap factors are optimized with the design shown on the left in Figure 2-7, where the width of each SiN segment is $w_{SiN} = 450$ nm, and they are separated from each other by a gap of $g_{SiN} = 400$ nm. The thickness of the SiN layer and the vertical spacing from the gain medium are $h_{SiN} = 200$ nm and $h_{gap} = 200$ nm, as dictated by the CMOS fabrication process. The nominal thickness of the deposited $Al_2O_3:Er^{3+}$ layer was 1.2 μm, with a radial variation of approximately 5 % from the center to the edge of the 200 mm substrate holder.

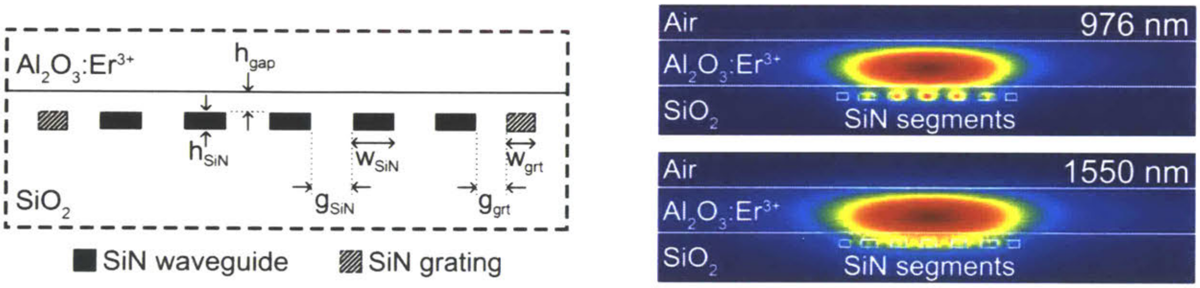

Figure 2-7: Cross-section of laser cavity showing the buried SiN waveguide and grating segments (not to scale). Fundamental TE modes of 980 nm pump and 1550 nm signal in the laser cavity.

Using these design parameters, the field profiles for the fundamental TE modes at the pump and signal wavelengths are simulated, and shown on the right in Figure 2-7. The gain medium confinement of the pump and signal modes are calculated to be $\Gamma_p = 0.841$ and $\Gamma_s = 0.828$ respectively. The intensity overlap of these two modes in the gain medium is $\gamma = 0.903$. This high overlap is enabled by the segmented SiN design, as it allows the shorter wavelength pump mode, which is otherwise mainly confined in the nitride layer in a single segment design, to expand into the gain medium. The pump-signal overlap γ is reduced when using the transverse magnetic (TM) mode for either the signal or the pump. Also, since the TM modes in this design can potentially suffer from coupling to substrate modes, more cavity losses would be expected. Moreover, the waveguide is also sufficiently birefringent that the TM mode resonance is outside of the C-band. Therefore due to their larger overlap factor, reduced in-cavity losses, and by appropriate grating design, fundamental TE signal and pump modes can provide the largest possible gain per unit length.

Feedback is provided by the buried SiN grating of width $w_{grt} = 300$ nm on either side of the waveguide segments. The grating is separated from the adjacent waveguide segment by a gap of $g_{grt} = 300$ nm. The grating strength is determined by how strongly the signal mode interacts with the grating, and is calculated as $\kappa = 7.56\ \text{cm}^{-1}$ between the forward and backward traveling modes in the 1.5 cm long laser cavity. Grating duty cycle was chosen to be 50 %. The grating period is calculated from the Bragg condition given by

$$\Lambda = \frac{\lambda_0}{2n_{\text{eff}}} \tag{2.2}$$

at the signal wavelength of $\lambda_0 = 1550$ nm. Considering the $Al_2O_3:Er^{3+}$ thickness variation, the period was varied from $\Lambda = 490$ nm to 496 nm, in order for the laser to operate within the 1530 nm - 1565 nm C-band.

2.4.3 Laser Performance and Characterization

The integrated laser is characterized using the setup shown in Figure 2-8. 976 nm fiber-coupled pump diodes were used with polarization controllers to pump the on-chip laser from both sides. Single-mode cleaved fibers were used to couple the pump and signal light on and off chip. The laser emission was collected by a fiber wavelength division multiplexer, and recorded using an optical spectrum analyzer.

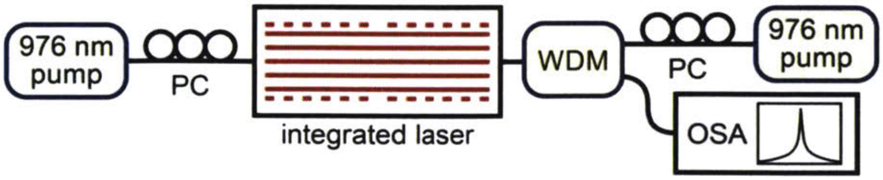

Figure 2-8: Diagram of the laser characterization setup

Using 220 mW of total on-chip pump power, a single-mode signal output of 2.6 mW is recorded at 1552.98 nm, where the emission spectrum is given in Figure 2-9. The output here is measured with a spectral resolution of 50 pm, the smallest available on a Yokogawa AQ6375 optical spectrum analyzer. No output above the noise floor is measured at any other wavelengths, as expected from the quarter-wave phase shifted DFB design. Moreover, the output wavelength matches well with the design target of 1550 nm for the TE signal mode, indicating single-mode TE output from the fabricated laser. This performance was achieved with an Er^{3+} doping concentration of $N_0 = 1.2 \times 10^{20}$ cm^{-3}.

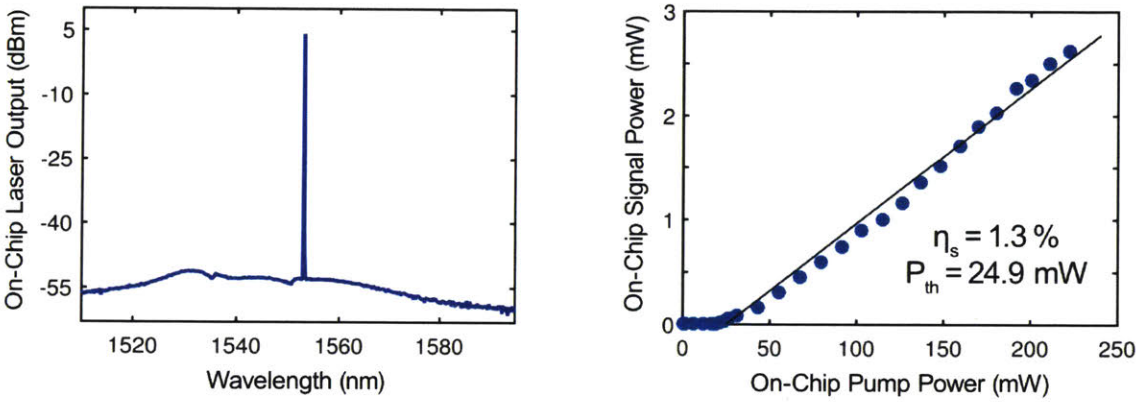

Figure 2-9: Laser emission spectrum and performance as measured by the output power with respect to the pump input power

Next, the laser performance is evaluated by measuring the output power at the signal wavelength as a function of pump power. The response plotted on the right in Figure 2-9 was recorded with the optimum pump polarization, corresponding once again to the maximum intensity overlap γ expected with TE pump and signal modes. The pump threshold was measured to be $P_{th} = 24.9$ mW. With increasing pump power over the threshold, the laser operated with a slope efficiency of $\eta_s = 1.3$ %. These results indicate similar performance to lasers whose gain media are fabricated at temperatures over 550 °C [40, 41], demonstrating the functionality of the newly developed 250 °C deposition process for the Al_2O_3:Er^{3+} gain medium. Potential improvements in the threshold and the slope efficiency can be achieved by recycling the residual pump back into the laser cavity. One can also enhance overall laser efficiency by improving pump coupling losses on-chip and to the gain medium.

2.5 Conclusion

I have demonstrated a substrate-bias-assisted sputtering method for the fabrication of undoped and rare-earth-doped Al_2O_3 thin films. The substrate bias allows for backend CMOS-compatible deposition temperatures as low as 250 °C. This deposition process allows us to integrate amplifiers and lasers with other active silicon photonic devices such as modulators, filters, and detectors that rely on low-resistance metal contacts and vias for high-speed operation. Additionally, other rare-earth-dopants such as neodymium, ytterbium, thulium, or holmium can also be co-sputtered with the 250 °C Al_2O_3 film. These dopants can be used in creating amplifiers and lasers at various near-to-mid infrared wavelengths for new applications. This marks an important step towards electronic-photonic integration for communications applications.

3 SPECTROSCOPY OF RARE-EARTH DOPED MEDIA

This chapter focuses on the development and the spectroscopy of the thulium-doped aluminum oxide ($Al_2O_3:Tm^{3+}$) medium. First, some fabrication details are provided. Then, methods for characterizing the newly developed material are studied. Experimental measurements of the excited state lifetime and absorption cross-sections are provided.

3.1 Fabrication Details for Thulium-doped Aluminum Oxide

The fabrication of $Al_2O_3:Tm^{3+}$ is carried out in a similar manner as $Al_2O_3:Er^{3+}$ developed previously, with the exception of the substrate bias. Al and Tm targets are simultaneously sputtered in a vacuum chamber using an Ar^+ plasma. All depositions were done using an AJA Orion sputtering tool with 300 W RF power supplies and 20 sccm (standard cubic centimeters per minute) mass flow controllers. The pressure in the sputtering chamber was controlled by the opening of the gate valve to the inlet of a turbomolecular pump. This gate valve position was adjusted automatically by a PID controller that matched the pressure reading in the chamber to the pressure setpoint provided by the user. This allowed the simultaneous setting of both the gas flows and the chamber pressure. A photograph of the AJA Orion sputtering system is shown in Figure 3-1.

Figure 3-1: A photograph of the AJA Orion sputtering tool located in EML of Microsystems Technology Laboratories at MIT, and a close-up view of the sputtering chamber with upside-down magnetron guns on the cover

Some sputtering systems have an important distinction in how they control the pressure in the chamber. By allowing the gate valve position to be adjusted by a quick PID controller, the AJA system allows independent control of gas flows and pressure. In contrast, the KJL Lab 18 system previously described achieves pressure control by direct control of the gas flow rates by the MFCs. In such systems, the gate valve typically doesn't move, or has only a number of position settings. Consequently, the flow rate directly determines the pressure of the chamber; and a PID controller is used for adjusting the MFC setpoints. The accuracy of both methods depend on the robustness of their respective PID controllers and the precision of the controlled variables (the gate valve position and the MFC flow rates respectively). However, from an operational perspective, it has proven to be useful to have independent control of both the flow rates and the chamber pressure, which can only be achieved by a moving gate valve as in the AJA system.

Al_2O_3:Tm^{3+} was sputtered reactively from separate Al and Tm targets in an Ar/O_2 environment. The process pressure was set at 3 mT, and was PID controlled by the gate valve position controller described above. The Ar flow rate was kept constant at 11 sccm. A 99.999 %

pure Al target was sputtered with an RF power of 200 W, yielding a bias voltage between 400-450 V. This bias voltage was manually maintained by controlling the O_2 flow into the chamber. Using a dedicated MFC, the O_2 flow was manually adjusted during deposition in order to produce stoichiometric Al_2O_3 at the substrate.

It is well known that excessive amounts of reactive gas flow (typically O_2 or N_2) causes target poisoning reactive sputtering due to the majority of the target surface being covered by an oxide or a nitride [42]. With a poisoned target, one effectively sputters from an oxide or a nitride target which can be useful in maintaining the desired oxide or nitride stoichiometry. However, a poisoned target also results in almost an order of magnitude slower deposition rates when compared to a non-poisoned target [35]. The goal of manually adjusting the O_2 flow during deposition is therefore to avoid poisoning the Al target while maintaining a high deposition rate. This is achieved with the O_2 flow that operates the target at the edge of poisoning, just before the bias voltage significantly drops. This flow rate depends on many factors such as the size of the vacuum chamber, how efficiently the chamber is pumped, and the positions of the gas inlets. For the specific AJA Orion tool used here, the appropriate O_2 flow at the beginning of the deposition was around 1.0-1.2 sccm, after which the bias dropped significantly. This flow rate had to be slowly increased during deposition to around 1.5 sccm, in order to keep a consistent bias on the Al target.

Upon consecutive depositions using the same Al target, the bias voltage on the Al target was observed to decrease. After approximately 10 runs, the Al bias remained around 370-400 V during deposition compared to the 400-450 V with a new target. Moreover, with an aging target, the deposition rate increased. Rates of up to 7.0 nm/min were recorded compared to the typical ~5 nm/min obtained with a new target. This can be attributed to the erosion pattern on the target surface as shown in Figure 3-2. The racetrack pattern visible on the target is due to the circular arrangements of the neodymium magnets in the magnetron sputtering gun that confine the Ar^+ ions close to the target surface. As a result, the area over which the Ar^+ ions are confined sputters more strongly, and causes the circular indentation. The increased surface area due to this uneven erosion can explain the increased sputtering yield. Since there was no way to monitor the deposited material thickness during deposition, the rate of the previous run was taken as reference for thickness control and deposition time. Despite the typical ±5 % change in the deposition rate between runs, referencing the deposition time on the previous run's deposition rate has been generally sufficient, as most of the integrated lasers were designed to tolerate small changes in layer thicknesses.

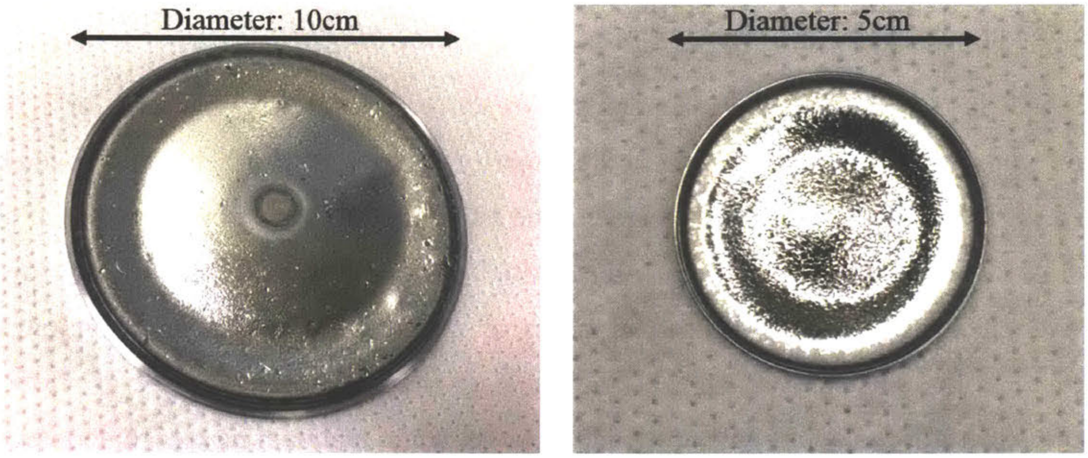

Figure 3-2: The circular erosion patterns on a used Al targets with 10 cm and 5 cm diameters. The circular arrangement of magnets on the sputtering gun "imprinted" on the targets after ~15 uses, as the target sputters more from the circular disk marked by these magnets.

A schematic drawing of the sputtering chamber is shown in Figure 3-3, reproduced from [43]. In this configuration, the targets are mounted inside sputtering guns facing downwards towards the substrate. The substrate is mounted on a rotating stage placed on top of two heating lamps that are capable of heating the substrate up to 600 °C. No load lock chamber was available in this system; so the chamber was vented each time a new deposition needed to be started. Although this may seem inconvenient at first, venting and cleaning the chamber with a household vacuum helped eliminate flakes and other particles that may have otherwise ended up in the deposited film. Before each run, the vacuum chamber was pumped down to below 10^{-4} Torr base pressure to eliminate contaminants including any remaining water vapor from the deposited film. During the last 20 min of this pump down procedure, the substrate heater was slowly ramped up to the deposition temperature of 550 °C to assist outgassing the chamber. Compared to the procedure described in Chapter 2, this process required a much higher temperature due to the absence of the substrate bias. This was followed by a 5 minute pre-deposition process onto the target shutters to clean the target surfaces of any contaminants or its native oxide layer. Then the deposition was carried out for the amount of time corresponding to the desired layer thickness, as calculated from the previous deposition rate.

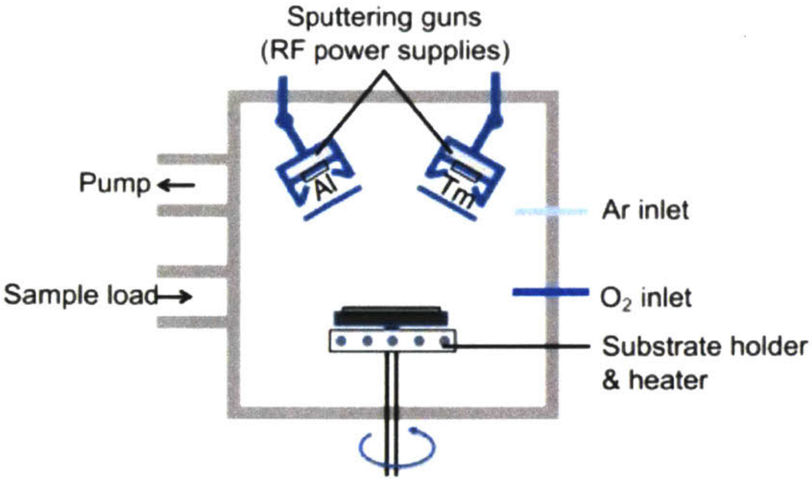

Figure 3-3: Schematic drawing of the sputtering chamber showing the Ar and O_2 gas inlets, Al and Tm sputtering sources, and the heated substrate holder.

3.2 Thulium Dopant Concentration

For a dopant whose absorption cross-sections are well known, it is relatively easy to calculate the atomic concentration per unit volume. By measuring absorption at a number of wavelengths, one can calculate the scaling factor between the absorption cross-section and this measured absorption. The dopant concentration is again calculated as shown in equation (2.1). As before, if the absorption cross-section $\sigma_{abs}(\lambda)$ is known at each wavelength, N_0 can be calculated from a linear fit between $\alpha(\lambda)$ and $\sigma_{abs}(\lambda)$. However, prior to this work, no measurements of $Al_2O_3:Tm^{3+}$ absorption cross-sections had been performed. Although Tm^{3+}-doped silica fiber had been previously studied [44], no information existed for the case of the alumina host.

To this end, in order to accurately characterize the absorption cross-sections, an independent measurement of dopant concentration has been performed. Using Rutherford back-scattering (RBS), atomic concentrations of Tm have been extracted for films deposited with different Tm^{3+} concentrations. Each film was deposited at a thickness of approximately 1 μm, on thermally-oxidized Si samples, where the thermal oxide thickness is 6 μm. An example RBS measurement is shown in Figure 3-4 where the measured spectrum is fitted to calculate the atomic concentrations of each element present in the film. For the example shown here, the fit to the top layer composition yielded atomic percentages of 39.502 %, 60.241 %, and 0.257 % for Al, O, and Tm respectively. The fit also yielded an atomic density of 0.940×10^{23} atoms/cm^3. Multiplying the atomic density with the percentage of the Tm atoms, we get a dopant concentration of 2.42×10^{23} cm^{-3} corresponding to the atomic concentration obtained when the Tm target is sputtered with 15 W of RF power.

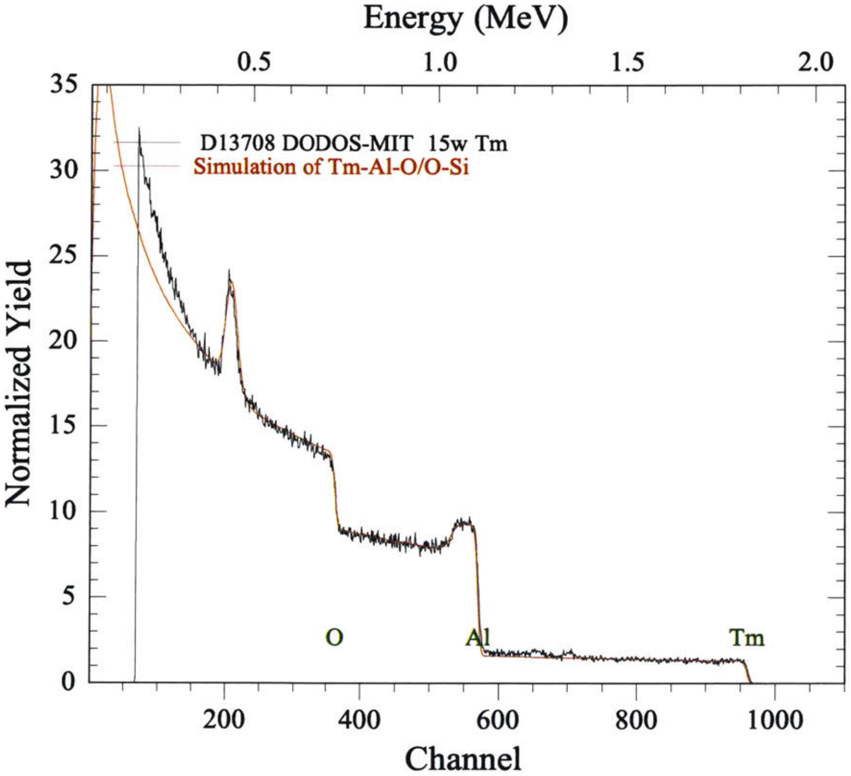

Figure 3-4: An example Rutherford back-scattering measurement for calculating Tm^{3+} dopant concentration in Al$_2$O$_3$:Tm^{3+} films

This measurement is then repeated for films deposited by using different RF powers delivered to the Tm target. The calculated concentration is then plotted against the RF power applied as shown in Figure 3-5. The exponential fit to the data is indicated by the dashed line, and is given by

$$N_0 = (0.0339 \times 10^{20}) P^{1.5909}\ \text{cm}^{-3} \tag{3.1}$$

3.3 Absorption Cross-Section at the Pump Wavelength

Once the concentration is known, the absorption cross-section can be calculated using the model in equation (2.1). For the first measurement around 785 nm, a Toptica DCL TA Pro tunable laser system with a tuning range of 770 nm to 800 nm was used. At each measurement wavelength and for each film with the known dopant concentration, the absorption in the fundamental slab mode in the $Al_2O_3:Tm^{3+}$ layer was characterized in the prism coupling setup. The intensity confinement factor of the fundamental slab mode was calculated as 0.968 at 785 nm, and was assumed to be constant for the 775-799 nm measurement window. Using the known concentration from the RBS measurements, the absorption cross-section was calculated for each wavelength and for each film with different Tm^{3+} concentrations. These results are plotted in Figure 3-6 showing the maximum measured absorption at 789 nm with an absorption cross-section of $(6.74 \pm 0.27) \times 10^{-21}$ cm^2. The absorption band has similar spectral structure to that observed in Tm^{3+}-doped fiber.

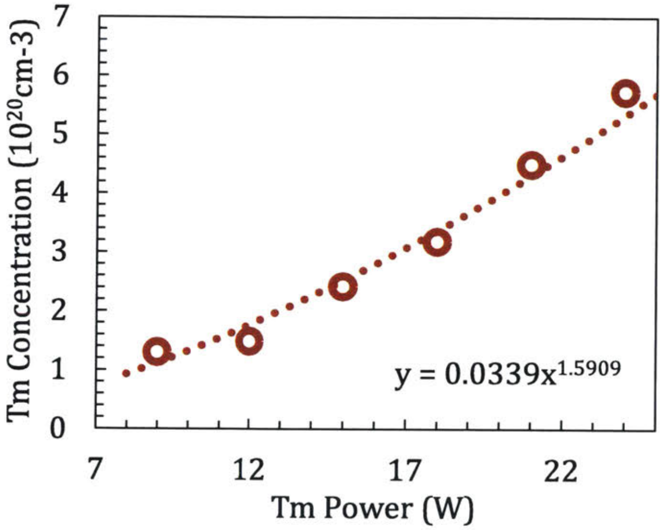

Figure 3-5: Tm^{3+} concentration in the sputtered film as a function of sputtering power delivered to the Tm target

3.4 Frequency-Domain Methods

The lifetime of the excited state (also referred to as the upper lasing state), together with the transition cross-sections, are essential pieces of information for understanding population level dynamics in gain media. Many optical phenomena including emission, absorption, saturation, and even high-order effects like energy transfer upconversion and cross-relaxation can be modeled by using excited state lifetimes and transition rates between energy states [45-49]. For $Al_2O_3:Tm^{3+}$, just like the absorption cross-sections, no accurate measurement of the excited state lifetime existed at the beginning of this project.

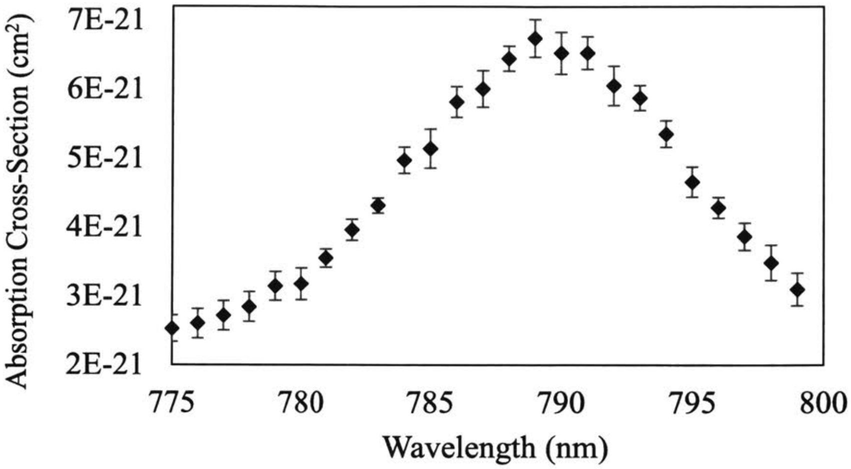

Figure 3-6: Absorption cross-section of Al_2O_3:Tm^{3+} from 775 nm to 800 nm

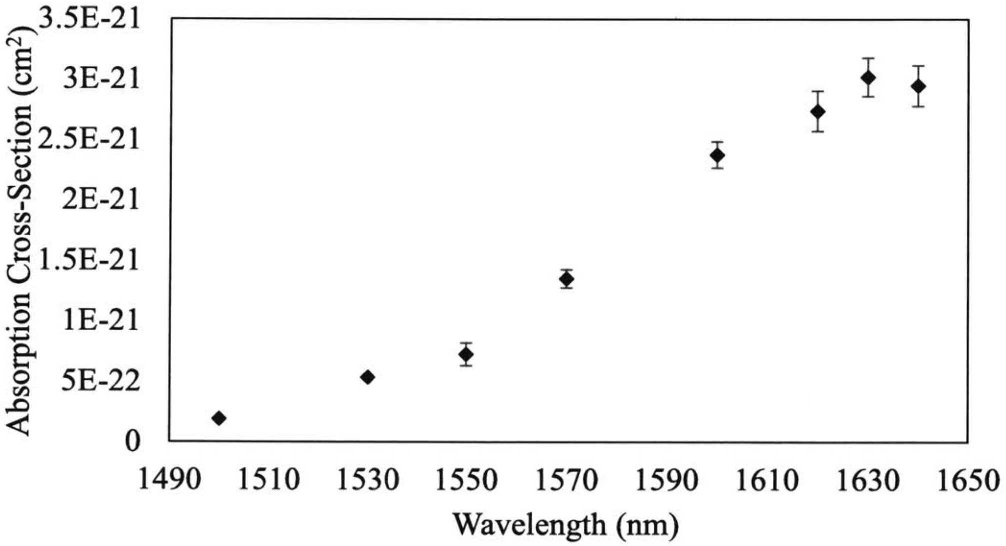

Figure 3-7: Absorption cross-section of Al_2O_3:Tm^{3+} from 1500 nm to 1640 nm

Typically, excited state lifetimes are measured using pulsed or square-wave excitation signals after which the system's expected low-pass transient response and the characteristic decay time are analyzed with an exponential decay [50]. In order to resolve the transient response, such time-resolved methods require pump excitations that are much shorter or that can be modulated with rise/fall times much faster than the lifetime to be measured [51]. Depending on the required duration, the excitation signal can be shaped with the use of a mechanical chopper [52], modulated by a pulsed electrical pump [53], or a pulsed source like a femtosecond laser can be used directly [54]. In all cases, a high responsivity photodetector is also typically required for a good signal-to-noise ratio at low input powers. In contrast to the fast excitation schemes, the low-pass characteristics of the system can be studied in the frequency domain by measuring its amplitude and phase response with a variable sinusoidal excitation. One example of a frequency domain measurement is the phase-shift method where the phase delay between the output signal and the excitation waveform is used to identify the system lifetime [55]. A similar family of methods include amplitude-based frequency-domain methods where the lifetime is measured by monitoring the pump frequency that halves the output intensity [56]. However, despite their versatility, the general family of frequency-domain spectroscopic techniques have not been studied in detail for characterization of solid state gain media. Moreover, no analyses on pump and signal power dependence or applications to measurements other than the lifetime have been found.

Here, I study the above described frequency-domain analysis in detail by deriving the complete transfer function between a modulated pump input and the signal output in rare-earth doped glass media. I analyze the dependence of system behavior on signal and pump rates in the frequency domain, and confirm the transfer function approximation by numerical simulations of the nonlinear rate equations. I then use this system description for accurately measuring the spontaneous emission lifetime and pump absorption cross-sections in rare-earth doped gain media. After verifying our methods in Er^{3+} and Tm^{3+}-doped fibers, we characterize $Al_2O_3:Tm^{3+}$ waveguides. These newly found parameters can be utilized to design more efficient amplifiers and lasers in the 1.8 – 1.9 um gain band of Tm^{3+}.

3.4.1 Two-Level Population Model with a Modulated Pump

To model a sinusoidally-modulated excitation in rare-earth doped media, we represent the gain medium with a two-level system. The use of a two-level system is validated by the assumption that rare-earth ions in any one of the higher energy states rapidly decay to the upper lasing state due to the short lifetimes in these higher energy states [47]. The populations of the two levels are governed by the rate equations that describe the rate of change of the number of rare-earth ions in the ground or excited states. Here, we will refer to the total population by N_t, the population in the ground state by N_0, and the population in the excited state by N_1, where

$N_0 + N_1 = N_t$ at all times. As N_t is constant, the rates of change of N_0 and N_1 have the same magnitude with opposite signs. This rate of change is dictated by stimulated signal and pump absorptions from the ground state, and the stimulated and spontaneous signal emission from the excited state as shown in Figure 3-8.

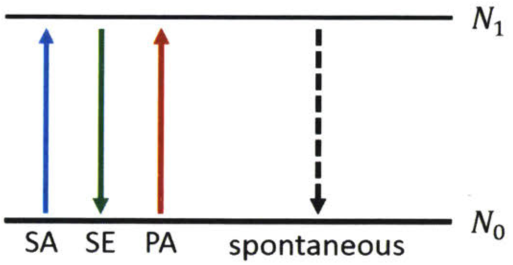

Figure 3-8: Two-level population model indicating signal absorption (SA), stimulated emission (SE), pump absorption (PA), and spontaneous emission.

The change in the population levels is described by

$$\begin{aligned}\frac{d}{dt}N_0 &= -\frac{d}{dt}N_1\\ &= \underbrace{-\sigma_{sa}\phi_s N_0 - \sigma_{pa}\phi_p N_0\big(1+m(t)\big)}_{\text{stimulated signal and pump absorption}} + \underbrace{\sigma_{se}\phi_s N_1}_{\substack{\text{stimulated}\\ \text{emission}}} + \underbrace{\frac{N_1}{\tau}}_{\substack{\text{spontaneous}\\ \text{emission}}}\end{aligned} \tag{3.2}$$

where ϕ_p and ϕ_s are the rates of pump and signal photons per unit area, σ_{sa}, σ_{pa}, σ_{se} are the signal absorption, pump absorption, and signal emission cross-sections, and τ the spontaneous emission lifetime. Pump and signal rates can be expressed as $\phi_{p,s} = I_{p,s}/\big(h\nu_{p,s}\big)$ where h is Planck's constant, $I_{p,s}$ are the intensities, and $\nu_{p,s}$ are the frequencies of the pump and signal photons respectively. Here, we have added a modulation term $m(t)$ to represent the introduced perturbation to the otherwise constant pump rate. In order to eliminate the excited state population N_1 from equation (3.2), we can rewrite it in terms of the total and ground state populations, and separate the modulation dependent pump absorption as follows.

$$\begin{aligned}\frac{d}{dt}N_0 &= -\sigma_{sa}\phi_s N_0 + \sigma_{se}\phi_s(N_t - N_0) - \sigma_{pa}\phi_p N_0\big(1+m(t)\big) + \frac{N_t - N_0}{\tau}\\ &= -N_0\left((\sigma_{sa}+\sigma_{se})\phi_s + \sigma_{pa}\phi_p + \frac{1}{\tau}\right) + N_t\left(\sigma_{se}\phi_s + \frac{1}{\tau}\right) - \sigma_{pa}\phi_p N_0 m(t)\end{aligned} \tag{3.3}$$

Then, using the coefficient of N_0 from equation (3.3), we can define an effective lifetime where

$$\frac{1}{\tau_{\text{eff}}} = (\sigma_{sa} + \sigma_{se})\phi_s + \sigma_{pa}\phi_p + \frac{1}{\tau}. \tag{3.4}$$

Using this definition, equation (3.3) can be rewritten as

$$\frac{d}{dt}N_0 = -\frac{N_0}{\tau_{\text{eff}}} + N_t\left(\sigma_{se}\phi_s + \frac{1}{\tau}\right) - \sigma_{pa}\phi_p N_0 m(t) \tag{3.5}$$

Moreover, if we choose to operate with a signal rate much less than the pump rate ($\phi_s \ll \phi_p$), the effective lifetime can be approximated by

$$\frac{1}{\tau_{\text{eff}}} \approx \sigma_{pa}\phi_p + \frac{1}{\tau} \tag{3.6}$$

This yields $1/\tau_{\text{eff}}$ as a linear function of ϕ_p, with a proportionality constant of σ_{pa} and a vertical intercept of $1/\tau$. From the description in equation (3.6), σ_{pa} and $1/\tau$ can be independently determined from a dataset of $(\phi_p, 1/\tau_{\text{eff}})$ pairs. Also, even if the exact pump rate ϕ_p cannot be characterized due to various pump coupling losses, as long as the pump power from the source is well known, the vertical intercept $1/\tau$ can still be precisely calculated.

3.4.1.1 Modulation to Population Levels

In order to decouple the modulation dependence from the nominal population levels, we let $N_0 = N_{0(\text{ss})} + \Delta N_0$, where $N_{0(\text{ss})}$ is the steady state population in the ground state, and ΔN_0 is the change introduced due to the pump modulation. In other words, $N_0 = N_{0(\text{ss})}$ when $m(t) = 0$. Consequently, the rates of change of N_0 and ΔN_0 are equal:

$$\frac{d}{dt}N_0 = \frac{d}{dt}\Delta N_0 \tag{3.7}$$

As $N_{0(\text{ss})}$ is the steady state population level with no pump modulation, it can be calculated from equation (3.5) by setting $m(t) = 0$.

$$\begin{gathered}\frac{d}{dt}N_{0(\text{ss})} = 0 = -\frac{N_{0(\text{ss})}}{\tau_{\text{eff}}} + N_t\left(\sigma_{se}\phi_s + \frac{1}{\tau}\right) \\ \Rightarrow N_{0(\text{ss})} = N_t\tau_{\text{eff}}\left(\sigma_{se}\phi_s + \frac{1}{\tau}\right)\end{gathered} \tag{3.8}$$

We can then use the rate of change and the steady state population from equations (5.1) and (3.8) to rewrite equation (3.5):

$$\begin{aligned}\frac{d}{dt}\Delta N_0 &= -\frac{N_0}{\tau_{\text{eff}}} + N_t\left(\sigma_{se}\phi_s + \frac{1}{\tau}\right) - \sigma_{pa}\phi_p N_0 m(t) \\ &= -\frac{N_{0(\text{ss})} + \Delta N_0}{\tau_{\text{eff}}} + N_t\left(\sigma_{se}\phi_s + \frac{1}{\tau}\right) - \sigma_{pa}\phi_p\left(N_{0(\text{ss})} + \Delta N_0\right)m(t) \\ &= -\frac{N_t\tau_{\text{eff}}\left(\sigma_{se}\phi_s + \frac{1}{\tau}\right) + \Delta N_0}{\tau_{\text{eff}}} + N_t\left(\sigma_{se}\phi_s + \frac{1}{\tau}\right) \\ &\quad - \sigma_{pa}\phi_p\left(N_{0(\text{ss})} + \Delta N_0\right)m(t)\end{aligned} \tag{3.9}$$

Simplifying equation (3.9) yields the nonlinear differential equation describing the "changing" part of the ground state population ΔN_0:

$$\frac{d}{dt}\Delta N_0 = -\frac{\Delta N_0}{\tau_{\text{eff}}} - \sigma_{pa}\phi_p\left(N_{0(\text{ss})} + \Delta N_0\right)m(t) \tag{3.10}$$

We can further simplify equation (3.10) by limiting the operation to cases where the steady state ground state population is much larger than the change in the ground state population: $N_{0(\text{ss})} \gg \Delta N_0$. This is possible for small modulation depths where $|m(t)| \ll 1$ resulting in small changes in the population levels. Under this assumption, we obtain the linear differential equation describing the change in the ground state population level given by

$$\frac{d}{dt}\Delta N_0 \approx -\frac{\Delta N_0}{\tau_{\text{eff}}} - \sigma_{pa}\phi_p N_{0(\text{ss})} m(t) \tag{3.11}$$

We can then evaluate the Laplace transform of both sides in equation (3.11) to get the transfer function between the pump modulation input and the resulting change in the ground state population level. This yields

$$s\Delta N_0(s) = -\frac{\Delta N_0(s)}{\tau_{\text{eff}}} - \sigma_{pa}\phi_p N_{0(\text{ss})} M(s) \tag{3.12}$$

Solving for the transfer function, we get

$$H_1(s) = \frac{\Delta N_0(s)}{M(s)} = -\frac{\sigma_{pa}\phi_p N_{0(\text{ss})}\tau_{\text{eff}}}{1 + s\tau_{\text{eff}}} \tag{3.13}$$

where $\Delta N_0(s)$ and $M(s)$ are Laplace transforms of ΔN_0 and $m(t)$ respectively. Equation (5.1) describes a single-pole low-pass filter with corner frequency $s_0 = 1/\tau_{\mathrm{eff}}$. Physically, the low-pass response of $H_1(s)$ indicates that the population levels will lag behind the modulation $m(t)$; and the system will respond to the modulation with a bandwidth determined by the effective lifetime τ_{eff}.

So far, we assumed that all the pump power input into the system goes into modulating the population levels where the signal mode spatially exists. Although this is a good approximation for fibers, many waveguides in the tight confinement regime have non-perfectly overlapping pump and signal modes due to strong waveguide dispersion. We must therefore include the pump-signal intensity overlap (Γ) within the gain medium by letting

$$\phi_p = \phi_{p0}\Gamma = \phi_{p0}\frac{\left|\iint_G e_p^* e_s\, da\right|^2}{\iint_\infty e_p^* e_p\, da \iint_\infty e_s^* e_s\, da} \tag{3.14}$$

where e_p and e_s are the electric fields at the pump and signal wavelengths, and G indicates cross-sectional boundary of the gain medium.

3.4.1.2 From Population Levels to the Change in Recorded Intensity

It is important to realize that $H_1(s)$ only represents the transfer function from the pump modulation $m(t)$ to the changing part of the ground state population level ΔN_0. Although the population level directly influences the absorption in the medium, it is not directly observable. To this end, we need to relate the population levels to a directly observable variable like the photodetector reading of the signal output intensity where the input is at a constant intensity. The following analysis is based on this two-stage system description illustrated in Figure 3-9 below.

Figure 3-9: Multi-stage system overview of two-level population model

We can describe the photodetector reading by the absorption modulated in the gain medium due to the changing population levels:

$$\begin{aligned} P_{out} &= P_{in} \exp(-\sigma_{sa} N_0 L + \sigma_{se} N_1 L) \\ &= P_{in} \exp\big((\sigma_{se} N_t - (\sigma_{sa} + \sigma_{se}) N_0) L\big) \\ &= P_{in} \exp\Big(\big(\sigma_{se} N_t - (\sigma_{sa} + \sigma_{se}) N_{0(\mathrm{ss})}\big) L\Big) \exp\big((-(\sigma_{sa} + \sigma_{se}) \Delta N_0) L\big) \\ &= P_T \exp\big((-(\sigma_{sa} + \sigma_{se}) \Delta N_0) L\big) \end{aligned} \tag{3.15}$$

where we defined the constant

$$P_T = P_{in} \exp\Big(\big(\sigma_{se} N_t - (\sigma_{sa} + \sigma_{se}) N_{0(\mathrm{ss})}\big) L\Big) \tag{3.16}$$

We make the same assumption that since ΔN_0 is small compared to $N_{0(\mathrm{ss})}$. Then, the time-dependent part in P_{out} can be approximated by a Taylor expansion:

$$P_{out} \approx P_T (1 - (\sigma_{sa} + \sigma_{se}) \Delta N_0 L) \tag{3.17}$$

We can also define the steady-state and time-dependent parts of the output signal power as $P_{out} = P_{out_{(ss)}} + \Delta P_{out}$, yielding

$$\begin{aligned} P_{out_{(ss)}} &= P_T \\ \Delta P_{out} &= -P_T (\sigma_{sa} + \sigma_{se}) \Delta N_0 L \end{aligned} \tag{3.18}$$

We can again evaluate the Laplace transform of both sides in equation (3.18) and obtain the transfer function between the changing population levels and the resulting change in the signal intensity:

$$H_2(s) = \frac{\Delta P_{out}(s)}{\Delta N_0(s)} = -P_{out_{(ss)}} (\sigma_{sa} + \sigma_{se})\, L \tag{3.19}$$

Here, since $P_{out_{(ss)}}$ is a constant, $H_2(s)$ is just a scaling factor, and indicates that there is no phase difference between the population level change and the signal output power. Therefore the only phase shift between the pump modulation and the signal output is due to $H_1(s)$.

Finally, the overall transfer function is given by the product of the individual transfer functions:

$$H(s) = \frac{\Delta P_{out}(s)}{M(s)} = \frac{\Delta N_0(s)}{M(s)}\frac{\Delta P_{out}(s)}{\Delta N_0(s)} = H_1(s)H_2(s) \tag{3.20}$$

Evaluating equation (3.20), we get

$$H(s) = \sigma_{pa}\Phi_p N_{0(\mathrm{ss})}\tau_{\mathrm{eff}}P_{\mathrm{out(ss)}}(\sigma_{sa} + \sigma_{se})L\frac{1}{1 + s\tau_{\mathrm{eff}}} \tag{3.21}$$

According to the low-pass frequency dependence indicated in equation (3.21), the signal output power will lag behind the pump modulation by an amount determined by the effective lifetime τ_{eff}. For modulations slower than τ_{eff}, the signal tracks the modulation closely, since the system is able to effectively respond to changes within its bandwidth. For modulations with time scales quicker than τ_{eff}, the system will attenuate the change in the signal output power, due to the low-pass filter response.

3.4.2 Numerical Simulations of Signal Output

In order to validate the approximations we made in the derivation of the low-pass response model in equation (3.21), we investigate numerical solutions to equation (3.2) using various pump modulation parameters. For these numerical solutions, we assumed typical spectroscopic parameters from rare-earth doped glasses where $N_t = 10^{20}$ cm^{-3}, $\sigma_{pa,sa,se} \approx 10^{-21}$ cm^2, and $\tau =$ 500 μs in a 10 cm long fiber with mode diameter of 5 μm. Unless indicated otherwise by the variables in each numerical simulation, a pump modulation frequency of $f = 2$ kHz, a signal input power of $P_{\mathrm{in}} = 10$ μW, and a steady-state pump power of 300 mW were used, yielding $2\pi f\tau_{\mathrm{eff}} \approx 0.5$.

First, we characterize the system response as a function of the modulation amplitude m_0 using a sinusoidal pump modulation of the form $m(t) = m_0\sin(2\pi f t)$. In Figure 3-10, we plot the normalized signal output in arbitrary units for $0.1 < m_0 < 0.9$. With increasing m_0, the signal output deviates from the sinusoidal response predicted by the linear system model in equation (3.21). For instance when $m_0 = 0.9$, the output signal tends to quickly saturate before the end of the first half-cycle of the pump modulation, due to the large initial increase in the pump rate. This large pump power also results in the near-complete population depletion of the ground state, saturating the amplifier and flattening the otherwise sinusoidal output signal level. In contrast, for small m_0, the output signal remains sinusoidal and can be modeled with the transfer function approximation above. Consequently, we set $m_0 = 0.1$ for all subsequent simulations and measurements.

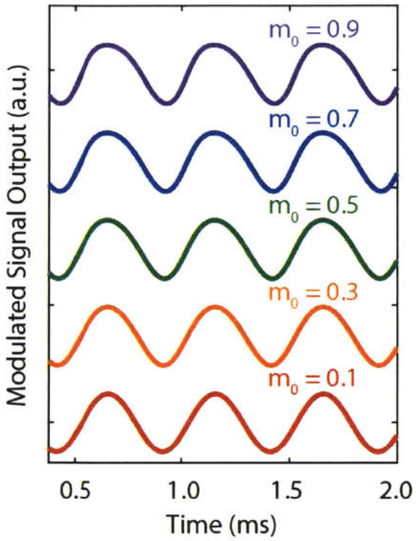

Figure 3-10: Signal output waveform as a function of modulation amplitude m_0

Next, we study the effects of the pump modulation frequency on the resultant signal. In Figure 3-11, we plot the signal output waveform with pump modulation frequencies from 50 Hz to 20 kHz with a nominal pump power of 300 mW. For each modulation frequency, the variation in the signal output ΔP_{out} is normalized to its own steady state value of $P_{\text{out(ss)}}$. The dashed line indicates the expected 3 dB system bandwidth of $f = 1/2\pi\tau_{\text{eff}}$ where τ_{eff} is calculated with the spectroscopic parameters above. For modulations slower than the system bandwidth, the signal output stays in phase with the modulation input. On the other hand, with faster modulations, the signal output lags behind the pump input as indicated by the tilting phase of the colored waveform. On the dashed line, the phase shift is exactly $\pi/4$ where the modulation frequency is equal to the system bandwidth. The numerical solutions also verify the predicted attenuation of the output signal for modulations above the 3 dB filter cutoff. This is indicated by the reduced contrast of the plotted waveform with increasing modulation frequency.

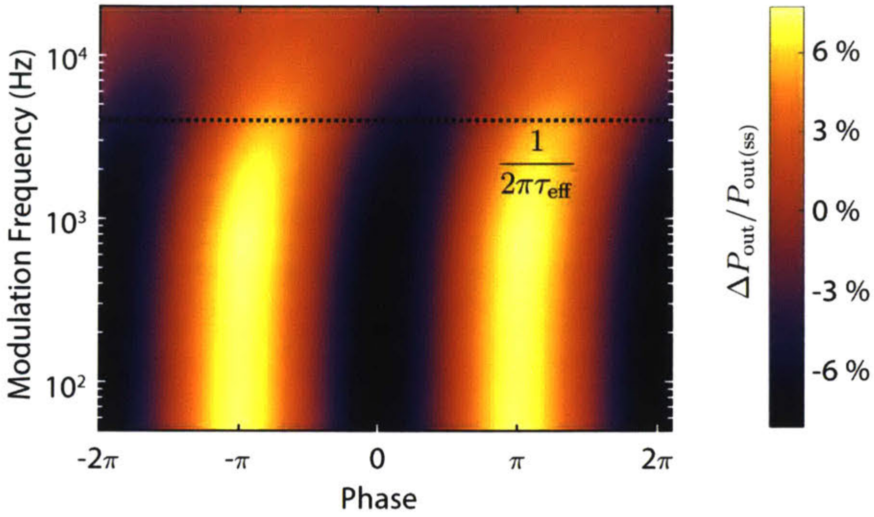

Figure 3-11: Signal output waveform as a function of pump modulation frequency from 50 Hz to 20 kHz.

Finally in Figure 3-12, we analyze the pump power dependence of the signal output waveform. As before, for each pump power simulated, ΔP_{out} is normalized to its own steady state value of $P_{\text{out(ss)}}$. Equivalent pump rates are plotted in the secondary vertical axis in corresponding spectroscopic units from equation (3.4). According to the numerical solutions, for pump powers less than 14 dBm ($\phi_p \sigma_{pa} \tau < 1$), the ground state stays mostly filled, and no significant change is expected in the signal output as absorption is only weakly modulated. For pump powers over 24 dBm ($\phi_p \sigma_{pa} \tau > 10$), gain is saturated due to the mostly-filled excited state; and the output signal power again does not exhibit significant change with respect to its steady state value. In contrast, when $1 < \phi_p \sigma_{pa} \tau < 10$, changes in pump power result in large variations in the signal phase shift. This variation is induced by τ_{eff}'s dependence on the pump rate ϕ_p, and is indicated by the "tilts" in the plotted signal waveforms. A higher pump rate results in a shorter effective lifetime; and the system exhibits a smaller phase shift due to reduced $2\pi f \tau_{\text{eff}}$ product. Here, the dashed line indicates the expected phase shift from the transfer function in equation (3.21), and is equal to the angle of the complex quantity $1/(1 + s\tau_{\text{eff}})$. The phase difference between the signal waveforms under low and high pump rates is approximately $\pi/2$, corresponding to the phase shift experienced in a single-stage low pass filter. Moreover, the excellent agreement of this dashed line with the tilted signal waveforms once again proves the validity of the approximations in the above derivation.

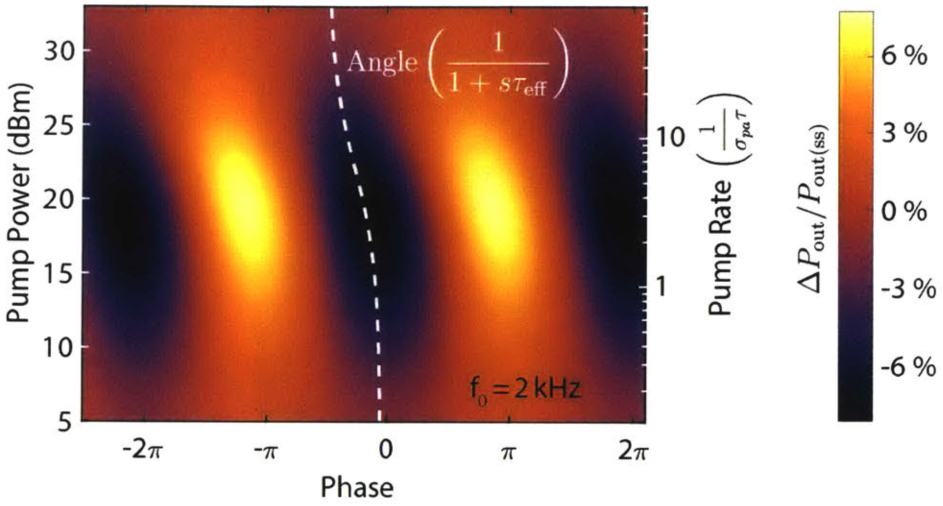

Figure 3-12: Signal output waveform as a function of pump power from 5 dBm to 33 dBm.

3.4.3 Experimental Characterization of Rare-Earth Doped Gain Media

We can utilize the change in the phase shift of the output signal to study system dynamics for various gain media. Specifically, due to the pump rate dependence of the effective lifetime, power dependent system response can be analyzed in order to accurately characterize spectroscopic parameters such as absorption and emission cross-sections, and the spontaneous emission lifetime. The experimental setup is shown in Figure 3-13, where a rare-earth doped fiber or waveguide is pumped with a modulated pump laser. The signal is coupled to the gain medium with the use of a fiber wavelength division multiplexer. Modulated signal output is measured with a photodetector, and its amplitude and phase are compared to the modulation input using a lock-in amplifier. For an accurate analysis by the lock-in amplifier, it is important to strongly attenuate any residual pump light at the detector. Even though typical 1.5 – 1.9 μm InGaAs detectors usually have reduced responsivity at the shorter pump wavelengths for many rare-earth ions (976 nm for Er^{3+}, 785 nm for Tm^{3+}), we added a Si window for a stronger pump attenuation. The use of counter-propagating pump and signal inputs can also provide additional extinction of the pump at the detector if necessary.

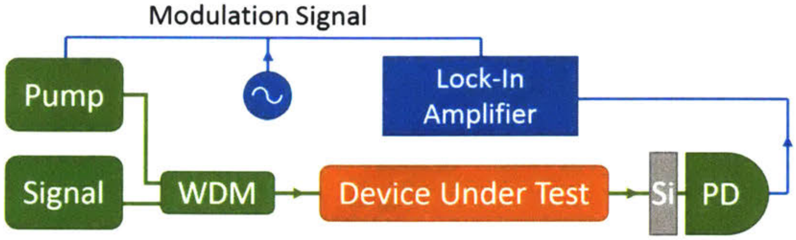

Figure 3-13: Experimental setup for frequency-domain spectroscopy of rare-earth doped fibers and waveguides

The key to accurate spectral characterization is identification of the effective lifetime τ_{eff} as a function of pump power as per equation (3.6). We first verify this method by measuring the lifetime of two gain media that are well documented in literature: Er^{3+}-doped silica fiber, and Tm^{3+}-doped silica fiber. With the use of the lock-in amplifier, we measure the magnitude and phase of the transfer function between the change in the signal output and the pump modulation as a function of pump power.

3.4.3.1 Er^{3+}-doped silica fiber

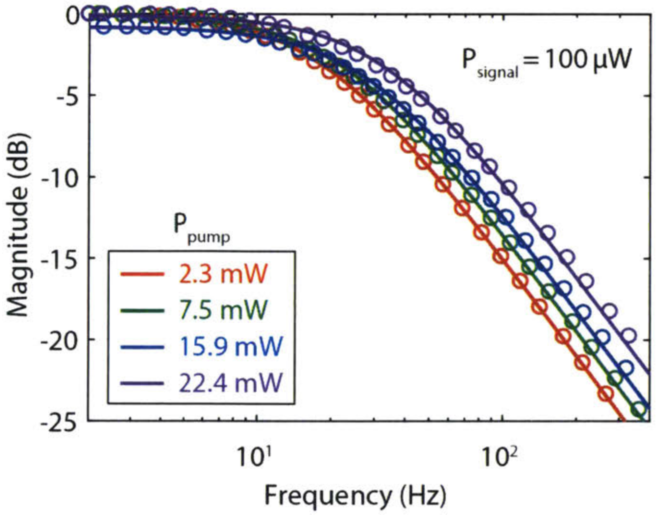

Figure 3-14: Magnitude of transfer function $H(s)$ for Er^{3+}-doped silica fiber

For the Er^{3+}-doped fiber, the magnitude and phase responses are plotted in Figure 3-14 and Figure 3-15 with the circles. For this measurement, the 1550 nm signal power in the fiber was approximately 100 μW, much smaller than the 976 nm pump power (> 1.5 mW).

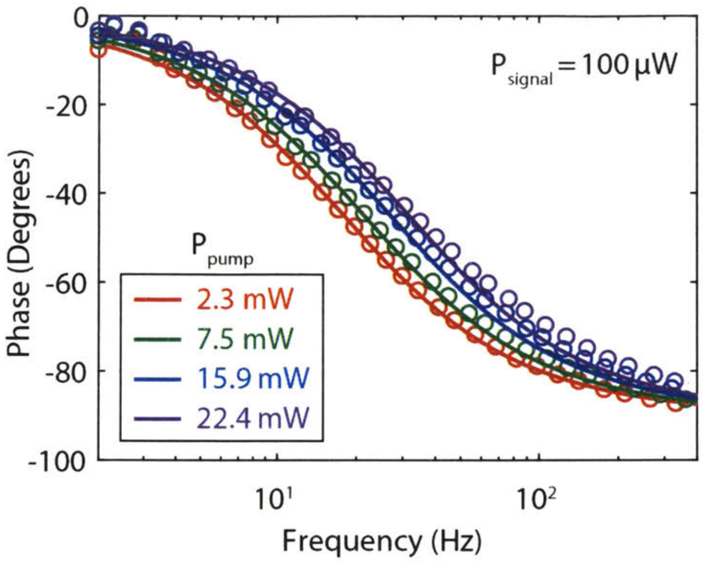

Figure 3-15: Phase of transfer function $H(s)$ for Er^{3+}-doped silica fiber

A least-squares fit was applied for each pump power to obtain the solid lines corresponding to the analytical transfer functions expected according to the model above. Both the magnitude and phase responses show excellent agreement with the single-pole filter description. Moreover, with increasing pump rate, filter cutoff $(1/2\pi\tau_{\text{eff}})$ shifted to higher frequencies due to the reduced effective lifetime. With two-pole filter fits to account for the possibility of a shorter lifetime of a higher energy state, a second pole was found at a much higher frequency, but no significant changes were observed in the magnitude and phase data around the first pole.

Using these transfer function fits, we then plot the location of the first pole as a function of pump power in Figure 3-16. The data are accurately represented by the linear fit (solid line), in agreement with the linear pump power dependence in our definition of the effective lifetime. The vertical intercept here corresponds to an unpumped gain medium, and is therefore equal to the inverse of the spontaneous emission lifetime $1/\tau$ as before. For the Er^{3+}-doped fiber, τ was measured to be 9.72 ± 0.11 ms from the linear fit, matching literature data for many types of Er^{3+}-doped silica fiber [57]. This measurement verifies our effective lifetime model and its pump power dependence, and demonstrates how it can be used to measure the spontaneous emission lifetime for new gain media. We can also determine the pump absorption cross-section from the slope in Figure 3-16 using equation (3.6). After converting from the plotted pump power (P_p) to the pump rate using $\phi_p = P_p/Ah\nu_p$, the slope yields $\sigma_{pa} = (2.24 \pm 0.04) \times 10^{-25}$ m^2 at the pump wavelength of 976 nm, where we calculated the circular mode area (A) using a 9 μm mode diameter. This measurement again matches with previously reported data from various Er^{3+}-doped silica fibers [58].

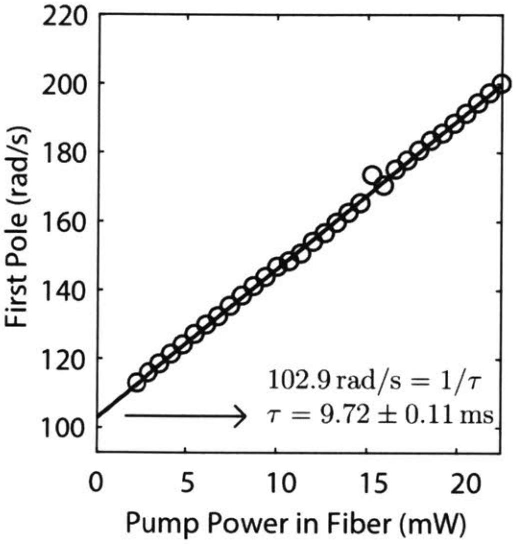

Figure 3-16: First pole location of the low-pass filter fits to the measured transfer functions $H(s)$ in Er^{3+}-doped silica fiber as a function of pump power

3.4.3.2 Tm^{3+}-doped silica fiber

Next, we study the Tm^{3+}-doped silica fiber in the same manner in Figure 3-17, Figure 3-18, and Figure 3-19. Corresponding to Tm^{3+} emission and absorption spectra, we used 1900 nm and 785 nm signal and pump laser diodes, with powers of 90 μW and > 1 mW respectively. As before, at each pump power, we fit transfer functions using the measured magnitude and phase responses, and represent the inverse of the effective lifetimes with a linear fit. It is known that the spontaneous emission lifetime in typical Tm^{3+}-doped silica fibers (~ 500 μs) is significantly shorter than that in Er^{3+}-doped silica (~ 10 ms). Therefore, shorter lifetimes corresponding to higher energy levels can more significantly alter the phase response around $1/2\pi\tau_{\mathrm{eff}}$ for Tm^{3+}. This explains why the phase response slightly differs from the transfer function fits at frequencies above 1 kHz in Figure 3-18. Consequently, two-pole filter fits were used to capture any shorter lifetimes that may be influencing system response at these higher frequencies. The second, high-frequency pole most likely reflects the fast relaxations from higher energy states. But this pole wasn't used to quantify any of these faster system dynamics in this analysis. Additionally, due to the shorter lifetime, we used higher pump powers than in case of Er^{3+} in order to resolve the differences in the four magnitude and phase responses plotted in Figure 3-17 and Figure 3-18 at different pump powers. Nevertheless, the linear fit to the first pole locations in Figure 3-19 indicates a spontaneous emission lifetime of 611 ± 42 μs, agreeing with previous results [44, 59]. Similarly, the pump absorption cross-section at 785 nm is calculated from the slope of the linear fit, and yields $\sigma_{pa} = (5.60 \pm 0.76) \times 10^{-25}$ m², in agreement with previous measurements in Tm^{3+}-doped silica fiber [59].

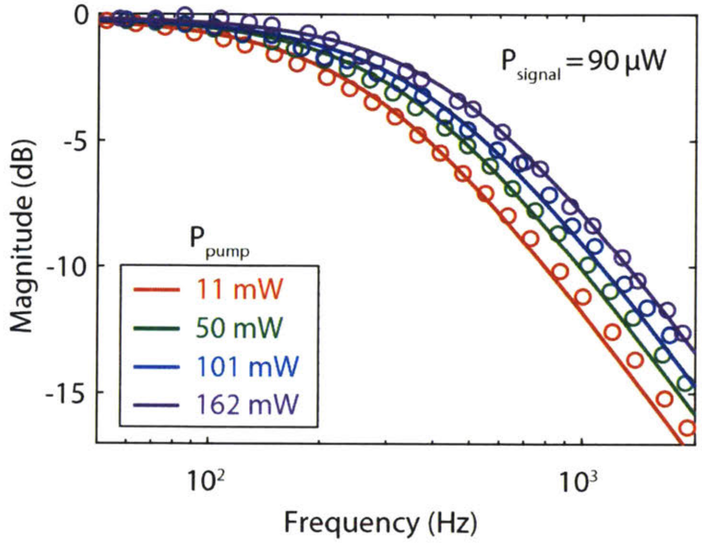

Figure 3-17: Magnitude of transfer function $H(s)$ for Tm^{3+}-doped silica fiber

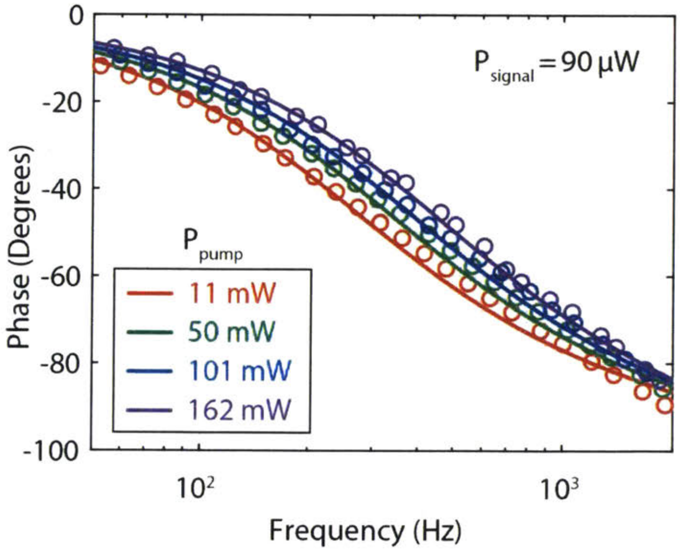

Figure 3-18: Phase of transfer function $H(s)$ for Tm^{3+}-doped silica fiber

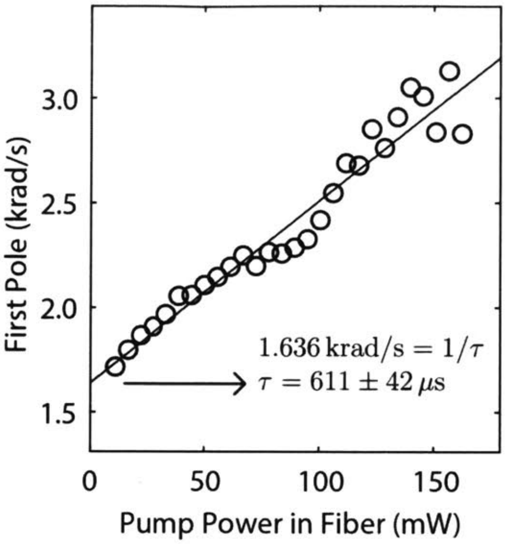

Figure 3-19: First pole location of the low-pass filter fits to the measured transfer functions $H(s)$ in Tm^{3+}-doped silica fiber as a function of pump power

3.4.3.3 Al_2O_3:Tm^{3+} waveguide

After verifying the frequency-domain methods derived here, we characterize our newly developed Al_2O_3:Tm^{3+} gain medium. We use the inverted ridge waveguide design in Figure 3-20 consisting of a $h_{SiN} = 200$ nm thick multi-segment SiN structure and a $h_{Al2O3} = 1.1$ µm thick back-end deposited gain medium. The SiN layer was fabricated in a 300 mm CMOS foundry via plasma enhanced chemical vapor deposition and patterned using deep reactive ion etching into $w_{SiN} = 300$ nm wide segments separated by gaps of $g_{SiN} = 350$ nm. The Tm^{3+} dopant concentration was 1.6 x 10^{20} cm^{-3}, as measured by Rutherford back-scattering.

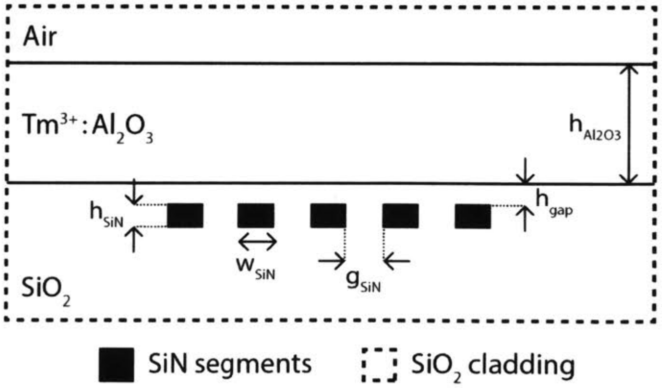

Figure 3-20: Inverted ridge waveguide design with multi-segment SiN structure and blanket-deposited Al_2O_3:Tm^{3+} layer

This specific waveguide design confines majority of pump and signal fundamental transverse electric (TE) modes in the blanket-deposited gain medium as indicated by the mode intensity profiles in Figure 3-21 and Figure 3-22. Here, the pump mode at 785 nm can be estimated as an ellipse of 1 μm × 4.5 μm in size, with a corresponding mode area of $A = 14.1\ \mu\text{m}^2$.

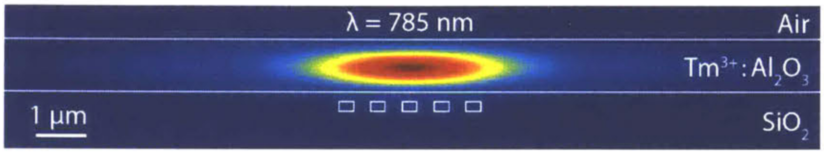

Figure 3-21: Intensity profile of the fundamental TE pump mode at 785 nm for the inverted ridge waveguide design

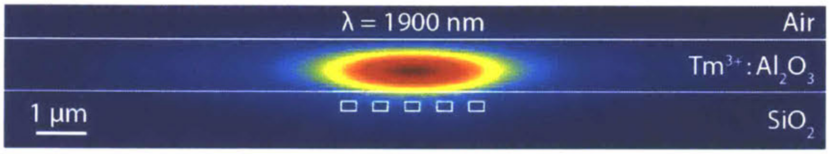

Figure 3-22: Intensity profile of the fundamental TE signal mode at 1900 nm for the inverted ridge waveguide design

Corresponding magnitude and phase responses for the Al_2O_3:Tm^{3+} waveguide are given in Figure 3-23 and Figure 3-24 respectively. Here, similar to the Tm^{3+}-doped silica fiber, we used two pole filter fits and plotted the corresponding first pole locations in Figure 3-25. The linear fit yields the spontaneous emission lifetime of 568 ± 48 μs, and an absorption cross-section of $\sigma_{pa} = (5.59 \pm 0.43) \times 10^{-25}\ \text{m}^2$. These results are similar to those measured in Tm^{3+}-doped silica fiber. More importantly, this absorption cross-section at 785 nm measured using the frequency domain analysis agrees with the prism coupling measurement shown earlier in Figure 3-6. Note that the magnitude and phase responses in Figure 3-23 and Figure 3-24 were measured with pump powers only up to 20 mW, whereas the same measurement for Tm^{3+}-doped silica fiber required 150 mW. This is due to the pump mode area being smaller by a factor of 4.5 in the waveguide and resulting higher pump rate ϕ_p.

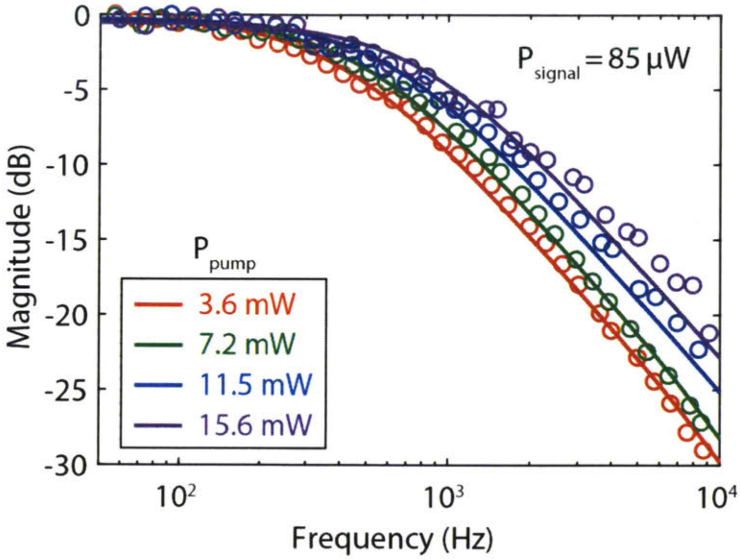

Figure 3-23: Magnitude of transfer function $H(s)$ for Al_2O_3:Tm^{3+} waveguide

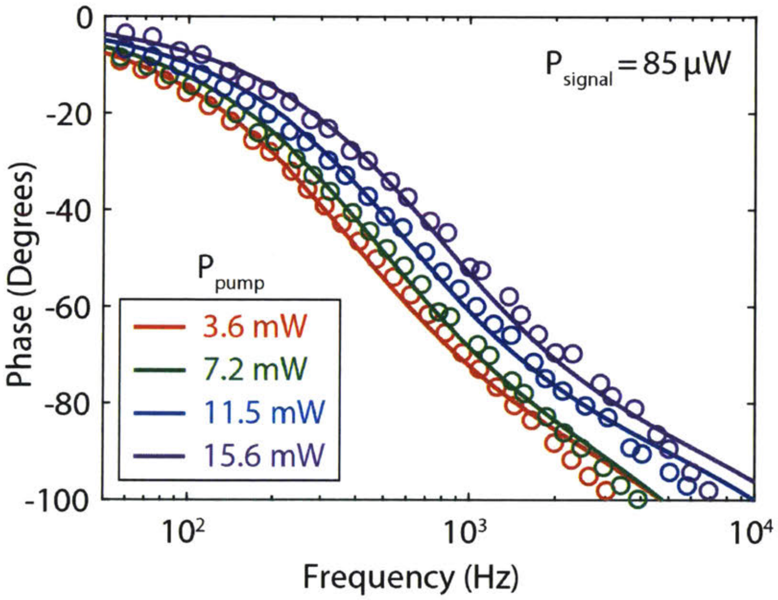

Figure 3-24: Phase of transfer function $H(s)$ for Al_2O_3:Tm^{3+} waveguide

3.5 Conclusion

We developed and standardized the fabrication methodology for Al_2O_3:Tm^{3+} using a reactive sputtering process, similar to the process used for Al_2O_3:Er^{3+} before. We identified an empirical relationship between the RF power delivered to the Tm target during deposition and the Tm^{3+} dopant concentration in the resulting film. We then measured the absorption cross-sections around the pump wavelengths of 785 nm and 1630 nm, using the prism coupling technique and tunable pump lasers.

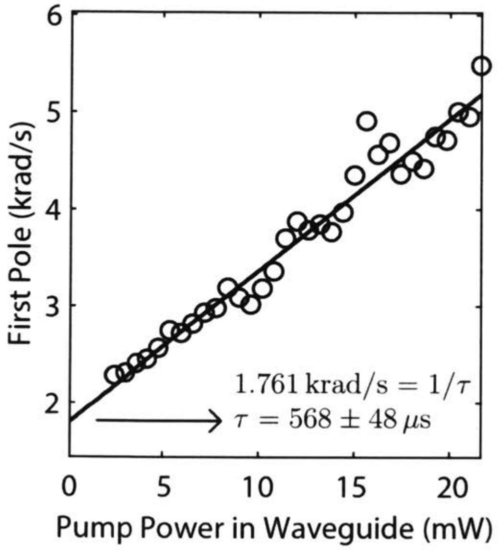

Figure 3-25: First pole location of the low-pass filter fits to the measured transfer functions $H(s)$ in Al_2O_3:Tm^{3+} waveguide as a function of pump power

For characterizing the lifetime in the newly developed medium, we have identified and detailed a family of frequency domain methods to characterize the system response in optically-pumped rare-earth doped gain media. The methods outlined are based on describing the effective system lifetime as a linear function of the pump rate, and characterizing how this lifetime dictates system bandwidth. We used a two-level model to describe the energy levels in the gain medium, and derived a low-pass filter response between the modulated pump and the resulting population levels that determine the signal gain and absorption. We verified our methods by confirming the well-known spontaneous emission lifetimes and pump absorption cross-sections in Er^{3+} and Tm^{3+}-doped silica fibers. Then we characterized our newly developed Al_2O_3:Tm^{3+} waveguides and measured the spontaneous emission lifetime and 785 nm absorption cross-section as $\tau = 568 \pm 48$ μs and $\sigma_{pa} = (5.59 \pm 0.43) \times 10^{-25}$ m^2 respectively.

The methods described here can be expanded by modeling the gain media as 3-level or 4-level systems. Obtaining an analytical description with more transitions can yield more accurate system representations and allow spectroscopic measurements of more complex kinetics such as upper state transition or relaxation cross-sections and lifetimes. The pump power dependence of system bandwidth can also be utilized in other media such as semiconductors for excited-state lifetime measurements.

4 LASER STABILIZATION VIA ATHERMAL RESONATOR REFERENCE

In this chapter, I use the techniques developed for the physical vapor deposition of aluminum oxide to design and fabricate devices with titanium dioxide (TiO_2). I make use of the negative thermo-optic coefficient of TiO_2 to design a resonator with specific resonances that aren't affected by thermal fluctuations. I then use the developed resonators to build a laser stabilization system using the Pound-Drever-Hall technique. Finally, I characterize the stabilized laser using an external mode-locked laser reference and analyze the improvements in the linewidth of the locked laser.

4.1 Thermal Stability in Integrated Photonics

The thermal response of an integrated photonic device is determined by the temperature dependence of the materials it is made of. Physically, there are two different phenomena that influence the behavior of light for integrated devices:

1. thermal expansion

2. thermo-optic effect

Thermal expansion refers to the phenomenon of a material changing in length, area, or volume as a response to a change in its temperature. The expansion in length is described by a linear expansion coefficient α_L where the relative change in length is given by the product of α_L and the change in temperature

$$\frac{\Delta L}{L_0} = \alpha_L \, \Delta T \tag{4.1}$$

For planar waveguide geometries where widths and heights are on the order of a few hundred nm, expansion in width and height are extremely small. The effects of these tiny changes in width and height on the effective indices of guided modes are even smaller. Therefore, we will only consider the thermal expansion in length for the waveguides studied here.

The thermo-optic coefficient describes the change in the refractive index of a material due to a change in its temperature. Similar to the coefficient of thermal expansion it is represented by a linear rate of change around the refractive index at a known temperature. The linear dependence can be expressed by

$$n(T) = n_0 + \frac{dn}{dT}(T - T_0) \tag{4.2}$$

where the refractive index at temperature T_0 is n_0. It is important to note that the thermo-optic shift is independent of thermal expansion. The index change is not related to the physical expansion or contraction of the material where the inter-atomic or inter-molecular distance changes. The index change is attributed to the electronic band structure of the material [60].

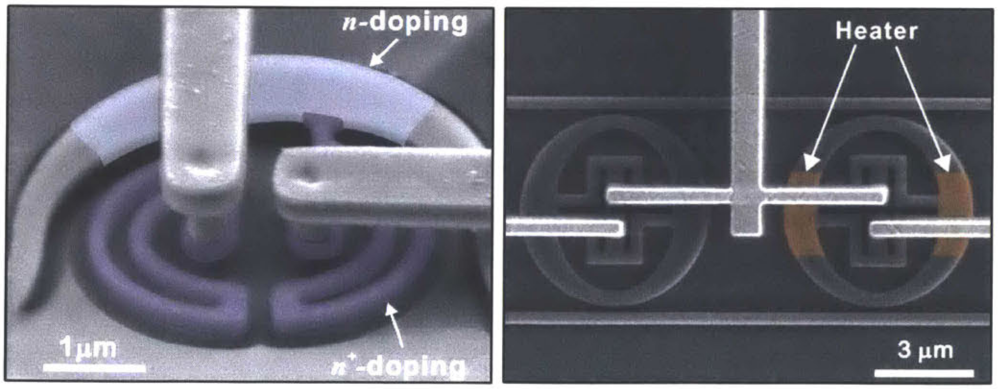

Tunable Phase Shifter

Tunable C-Band Filters

Figure 4-1: Examples of thermally tunable resonant devices: phase shifters [5] and filters [61]

The change of refractive index with temperature allows for tunable integrated devices such as various resonators, Bragg filters, or Mach –Zehnder interferometers (MZI). Scanning electron micrographs of some examples including phase shifters and filters are shown in Figure 4-1. In such a ring resonator, the resonance condition states that the optical path length must be an integer multiple of the wavelength in the resonator. This is summarized by

$$2\pi n_0(2\pi R_0) = 4\pi^2 R_0 n_0 = m\lambda \tag{4.3}$$

where m is the mode number, and R_0 is the radius of the ring resonator. When a temperature change ΔT is introduced the amount of spectral shift in the resonance for the same mode number m can be calculated from

$$\begin{aligned} 2\pi n(T)\big(2\pi R(T)\big) &= m\lambda \\ 4\pi^2 R_0\left(n_0 + \frac{dn}{dT}\Delta T\right)(1 + \alpha_L\,\Delta T) &= m(\lambda + \Delta\lambda) \\ = 4\pi^2 R_0\left(n_0 + \left(\frac{dn}{dT} + n_0\alpha_L\right)\Delta T + \frac{dn}{dT}\alpha_L(\Delta T)^2\right) & \end{aligned} \tag{4.4}$$

For small changes in temperature, the second order term with $(\Delta T)^2$ can be neglected, yielding

$$\begin{aligned} 4\pi^2 R_0\left(n_0 + \left(\frac{dn}{dT} + n_0\alpha_L\right)\Delta T\right) &\approx 4\pi^2 R_0 n_0 + m\,\Delta\lambda \\ \Longrightarrow \frac{\Delta\lambda}{\Delta T} \approx \frac{4\pi^2 R_0}{m}\left(\frac{dn}{dT} + n_0\alpha_L\right) &= \frac{\lambda}{n}\left(\frac{dn}{dT} + n_0\alpha_L\right) = \lambda\left(\frac{1}{n}\frac{dn}{dT} + \alpha_L\right) \end{aligned} \tag{4.5}$$

Therefore, when estimating the effects of thermal changes in spectral behavior, the correct parameters to compare are dn/dT and $n_0\alpha_L$. These parameters are summarized in Table 4-1 for commonly used materials in silicon photonics.

Clearly, thermal expansion for Si is an order of magnitude weaker than the thermo-optic shift. Additionally, the thermo-optic shift in Si is an order of magnitude stronger than the thermo-optic shift in other materials. Therefore, the strongest and the most efficient resonance shifts are obtained using thermal tuning in micro-resonators with a Si waveguide core. The smaller thermo-optic coefficients of SiN, Al_2O_3, or TiO_2 indicate that achieving the same spectral shift in a resonator with waveguide core made from these materials would require much larger amounts of power. However, it is important to mention that the as thermal expansion has to be multiplied by the refractive index, the $n_0 \alpha_L$ product can be as large as dn/dT for materials with high refractive indices and low thermo-optic coefficients such as TiO_2.

Material	n_0	dn/dT (K^{-1})	$n_0 \alpha_L$ (K^{-1})
Si	3.48	1.86×10^{-4} [62]	$\sim 9 \times 10^{-6}$ [63]
SiN	1.97	$2.5\text{–}4 \times 10^{-5}$ [64, 65]	$\sim 3 \times 10^{-6}$ [66]
SiO_2	1.45	0.95×10^{-5} [64]	$\sim 9 \times 10^{-6}$ [67]
Al_2O_3	1.65	4.9×10^{-5} [68]	$\sim 1.3 \times 10^{-5}$ [69]
TiO_2	2.23	-2.3×10^{-5} [68]	$\sim 2.2 \times 10^{-5}$ [70]

Table 4-1: Thermo-optic and thermal expansion coefficients of common materials in silicon photonics

Using equation (4.5), typical thermal shifts in Si and SiN resonators can be estimated as approximately 10 GHz/K and 1–2 GHz/K respectively. The exact shift depends on the confinement of the resonant mode within the waveguide core, as the core and cladding generally have significantly different thermo-optic coefficients. Although such shifts are extremely useful in designing thermally tunable or reconfigurable devices, they can also lead to stability issues. Thermal detuning of filters may cause communication systems to drop out parts of transmitted data, or drift out of spectral alignment. This is why despite the benefits of thermal tunability, non-zero thermo-optic coefficients can lead to significant thermal stability issues in integrated photonic systems.

One of the most common ways to mitigate thermally-induced resonance shifts is to use thermo-electric coolers (TEC) to stabilize the temperature of optical devices. An example of such a device is shown in Figure 4-2. The electrically controlled cooler consists of alternating types of semiconductor material sandwiched between electrically insulating and thermally conductive ceramic sheets. Utilizing the Peltier effect, coolers like the one shown here work by carrying heat from one ceramic plate to the other by means of a DC current. When the junction is conducting with the application of a sufficient voltage, the junction current moves heat between the two ceramic plates. In most cases, one plate is placed in contact with a heat sink; and the temperature of the other plate is controlled with a PID loop that modulates the junction voltage for a desired temperature reading.

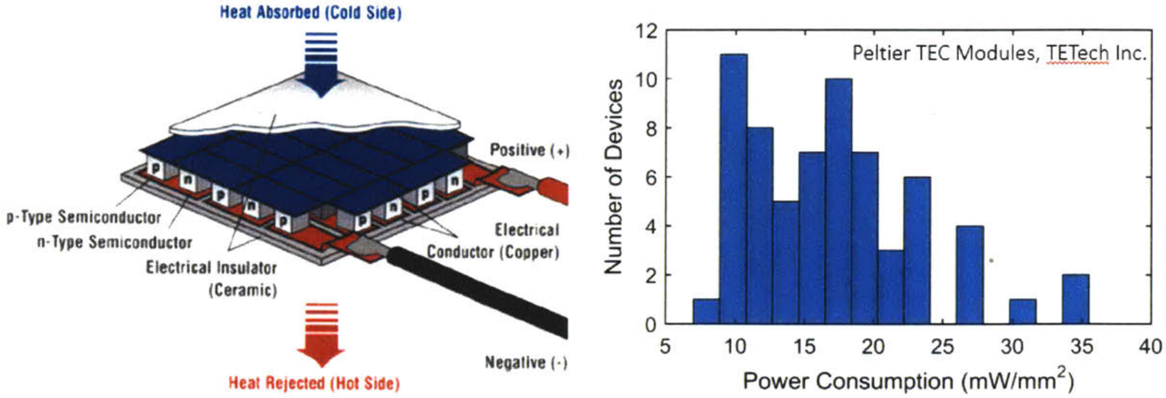

Figure 4-2: Schematic drawing of a thermo-electric cooler (TEC), and a histogram of average power consumption of common commercial models

Although Peltier TECs are useful for component-level testing, their use in large photonic systems is limited due to their large power consumption. For a typical TEC with an area of 1 inch^2 (~650 mm^2), the average power consumption can reach as high as 10 W, mainly due to the constant current flow required to sustain the desired temperature difference between the two ceramic plates. As integrated devices and systems are designed with low power budgets in mind, such power requirements preclude widespread use of TECs in integrated systems.

Another way to address thermal stability in integrated photonics is to make use of materials with positive and negative thermo-optic coefficients in tandem to compensate for the thermal resonance shift in equation (4.5). Among the materials with negative thermo-optic coefficients are TiO_2 as well as various polymers [71, 72], where some examples are shown in Figure 4-3. The discussion here will be limited to TiO_2 as most polymers cannot be easily integrated in a CMOS-based platform.

In the following sections, we investigate the noise components in a conventional SiN resonator, and quantify the expected thermal noise. Then we design and characterize an athermal resonator whose resonances exhibit no thermal shift within a specific range of temperatures. Finally, we use the Pound-Drever-Hall technique to lock a semiconductor laser to these resonators, and measure the spectral coherence of the resulting signals with an external mode-locked laser reference.

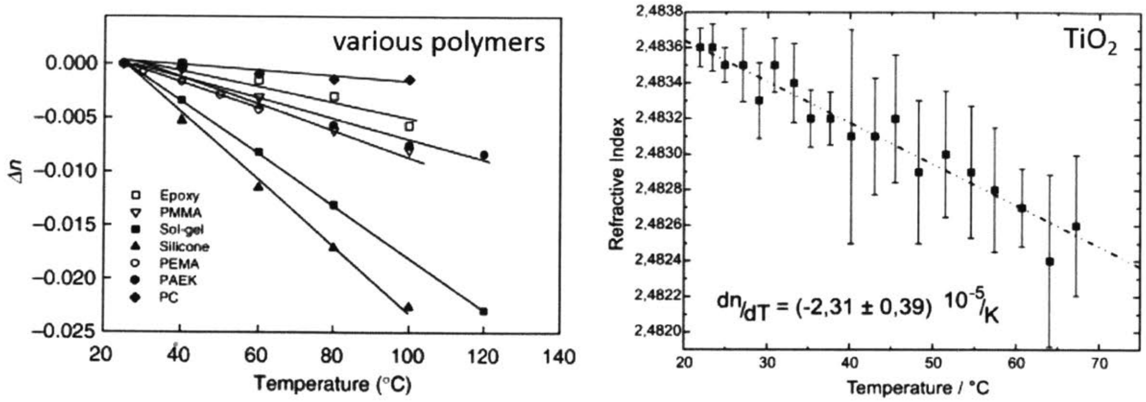

Figure 4-3: Materials with negative thermo-optic coefficients including polymers [72] such as epoxy, PMMA, silicone, and the most common inorganic example TiO_2 [68]

4.2 Phase Noise in Resonators

In order to understand how to design a resonator with less thermal noise than a conventional resonator, we first analyze the phase noise in a laser line in relation to the laser cavity, or a separate reference cavity that the laser stays locked to. In this manner, one effectively transfers the spectral stability of the reference cavity to the laser line. Whether a separate reference cavity is employed or not, phase noise refers to random fluctuations in the phase of the electric field in the laser line, and can be simply expressed by the waveform $\cos(\phi + \Delta\phi)$.

One of the most well-known sources of phase noise is spontaneous emission itself. In this case, the noise in the instantaneous frequency of the laser is white, and the resulting laser lineshape is Lorentzian. This is studied in detail by Schawlow and Townes in their 1958 paper [73] where they derived the resulting laser linewidth. This result was later modified by Melvin Lax who showed in 1967 that the laser linewidth is actually smaller by a factor of two [74]. This modified result Schawlow-Townes linewidth is given by

$$\Delta\nu_{\mathrm{ST}} = \frac{\pi(h\nu_{CW})}{P_{\mathrm{out}}Q^2}\nu_{CW}^2 \tag{4.6}$$

where ν_{CW} is the continuous-wave lasing frequency, P_{out} is the steady-state output power from the cavity, Q is the quality factor of the cavity, and h is Planck's constant. Here, $\Delta\nu_{\mathrm{ST}}$ is expressed as the full-width at half-max of the optical output spectrum.

In addition to the spontaneous emission phase noise that gives rise to the Schawlow-Townes linewidth, there are many other sources of noise including mechanical vibrations in the environment, changes in the pump power, and thermal fluctuations. Here, we will limit our discussion to the thermal fluctuations and how using materials with opposite signs of thermo-optic coefficients can help reduce thermal noise. We first start by expressing the phase noise power spectral density due to thermal fluctuations by

$$S_\varphi(f) = \left[\frac{4k_BT^2}{G}\left(\frac{1}{n}\frac{dn}{dT} + \alpha_L\right)^2\right]\left(\frac{\nu_{CW}}{f}\right)^2 \tag{4.7}$$

where k_B is Boltzmann's constant, T is temperature, G is thermal conductance to the substrate or another heatsink, n is the effective index of the resonator mode, and f is the offset frequency from the lasing frequency ν_{CW} [75]. We can model the thermal fluctuations as a "random walk" process where the temperature at time t is given by

$$T_t = T_0 + (\Delta T)_1 + (\Delta T)_2 + \cdots + (\Delta T)_t \tag{4.8}$$

Due to independence of individual walks, the variance in this random walk process can be calculated as

$$\mathrm{Var}[T_t] = \mathrm{Var}[(\Delta T)_1] + \mathrm{Var}[(\Delta T)_2] + \cdots + \mathrm{Var}[(\Delta T)_t] = \sigma^2 t \tag{4.9}$$

where we defined the variance for the temperature fluctuation at each time step as σ^2. In such a random walk process with linearly growing variance, the thermal linewidth can be calculated from the power spectral density of phase noise in equation (4.7) by

$$\Delta\nu_T = S_{\varphi T}(f)\omega^2 = \left[\frac{16\pi^2k_BT^2}{G}\left(\frac{1}{n}\frac{dn}{dT} + \alpha_L\right)^2\right]\nu_{CW}^2 \tag{4.10}$$

where the offset frequency is expressed as $\omega = 2\pi f$.

Putting together the phase noise contributions from the spontaneous emission and thermal sources, the total phase noise and resulting linewidth can be written as

$$S_\varphi(f) = \left[\frac{h\nu_{CW}}{4\pi P_{\mathrm{out}}Q^2} + \frac{4k_BT^2}{G}\left(\frac{1}{n}\frac{dn}{dT} + \alpha_L\right)^2\right]\left(\frac{\nu_{CW}}{f}\right)^2 \tag{4.11}$$

and

$$\varDelta\nu = \varDelta\nu_{ST} + \varDelta\nu_{\text{thermal}} = \left[\frac{\pi h\nu_{CW}}{P_{\text{out}}Q^2} + \frac{16\pi^2 k_B T^2}{G}\left(\frac{1}{n}\frac{dn}{dT} + \alpha_L\right)^2\right]\nu_{CW}^2 \tag{4.12}$$

In the following parts of this section, we use equation (4.12) to evaluate the Schawlow-Townes and thermal linewidths in a typical SiN resonator and compare contributions of each to the resulting laser linewidth.

4.3 A Conventional SiN Resonator

In order to evaluate the potential benefits of a thermally-stabilized resonator, we first investigate a SiN ring resonator with SiO$_2$ cladding and a SiN bus waveguide as shown in Figure 4-4. The measured spectral response of this resonator is also shown in Figure 4-4 where the transmission has been normalized to 0 dB.

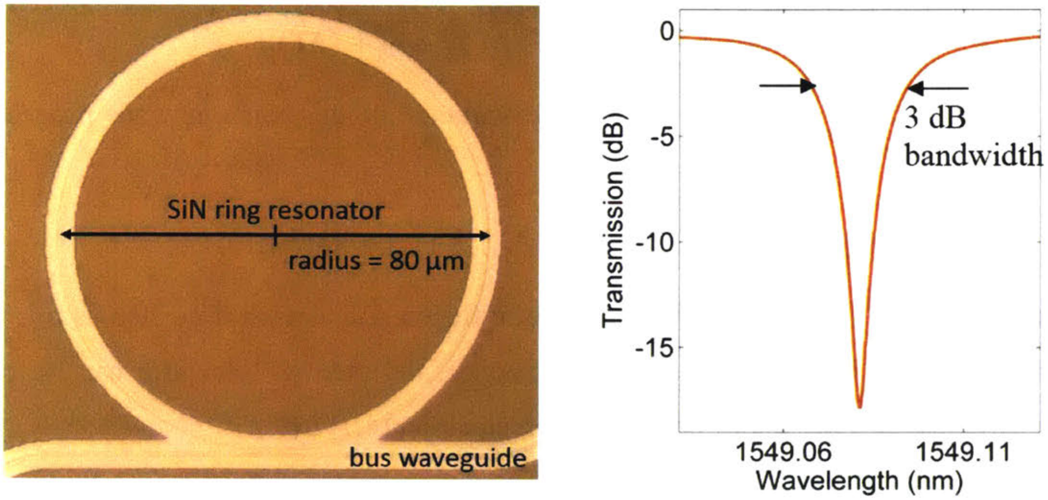

Figure 4-4: Photograph of a SiN resonator with SiN bus waveguide taken through a microscope objective, and the measured transmission response for one resonance around 1550 nm

With a radius of 80 μm, and a waveguide cross-section of 1 μm x 200 nm, this SiN resonator has a measured 3 dB bandwidth of 2.3 nm, resulting in a loaded quality factor of approximately $Q_l = 67{,}000$. The measured extinction ratio is $r_e = 17.9$ dB. The effective index in the fundamental TE guided mode in the resonator cross section is calculated from mode solutions as shown below in Figure 4-5, and is equal to 1.5183 at 1550 nm.

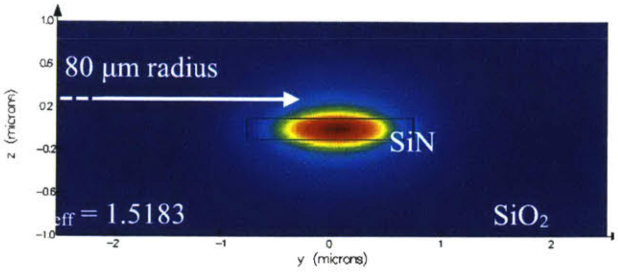

Figure 4-5: Fundamental TE mode profile in the SiN resonator

Another important parameter needed to characterize the thermal noise of the SiN resonator is its thermal conductance G to the substrate. The thermal conductance is a measure of how fast a material can conduct thermal energy to a heatsink. It can be defined similar to the electrical conductance, and is given by $G = k\,A/L$ where k is the material's thermal conductivity, A is the cross-sectional area that the heat is conducted through, and L is the separation between the material and the heatsink. Although one can employ a commercial solver like COMSOL to exactly evaluate the thermal conductance, we can approximate it simply by looking at the geometry of the resonator. Since the resonator is buried in SiO_2, the thermal conductivity that is needed is that of SiO_2. For the area, we can assume that the heat conductance effectively happens over a circular ring with the same center as the resonator, but with a radial width that is equal to a few times the waveguide width, which will be denoted with pw for the width of w. Finally, the length is the separation of the SiN resonator from the Si substrate, and is approximately the height of the buried oxide. Putting together these geometrical parameters and material properties, we get

$$G = k\frac{A}{L} \approx k\frac{\pi(R_o^2 - R_i^2)}{L} \approx k\frac{\pi((R+pw)^2 - (R-pw)^2)}{L} = \frac{2\pi kRpw}{L} \tag{4.13}$$

Using a thermal conductivity of $k = 1.4$ W/mK, a resonator radius of $R = 80$ μm, a waveguide width of $w = 1.5$ μm, and a buried oxide thickness of $L = 2$ μm, we get an approximate thermal conductance on the order of of $G = 0.002$ W/K where we assumed p to be around 4. In this case, we are assuming that the ring resonator conducts heat to the substrate through a hollow circular cylinder whose thickness is 4 times the waveguide width. Although one can use more advanced simulation techniques to calculate G exactly, the assumptions here are only to determine the order of magnitude for the thermal conductance, for comparison of the two linewidths. This estimated thermal conductance and the other parameters of the SiN resonator are summarized in Table 4-2 below.

Property	Value	Property	Value
Radius	80 μm	n_{eff}	1.5183
Coupling Gap	1 um	dn/dT	$3x10^{-5}$
Q_l	67,000	dL/(LdT)	$1.5x10^{-6}$
r_e	17.9 dB	G	0.002 W/K

Table 4-2: Parameters for a typical SiN resonator in on a CMOS-fabricated silicon photonic chip

Using the parameters in Table 4-2, and a typical steady state continuous-wave output power of $P_{\text{out}} = 5$ mW, we can calculate the linewidth due to phase noise from spontaneous emission and thermal fluctuations according to (4.12). Evaluating the Shawlow-Townes linewidth, we get $\Delta v_{ST} \approx 300\text{Hz}$, which is much narrower than the linewidths of typical diode or fiber lasers used in typical applications. On the other hand, linewidth due to thermal noise is calculated as $\Delta v_{\text{thermal}} \approx 1.6\text{MHz}$. It is also important to mention that the SiN resonator studied here is almost a best case scenario. Most Si resonators have much smaller thermal conductances to the substrate due to their smaller size (higher mode confinement). Moreover, since Si has an order of magnitude larger thermo-optic coefficient than SiN, the thermal noise is much larger.

From this estimation, we conclude that the phase noise in a conventional SiN resonator is dominated by thermal fluctuations. As $\Delta v_{\text{thermal}} \gg \Delta v_{ST}$, the expected linewidth from a laser locked to such a cavity is much wider than the Schawlow-Townes linewidth. One could design a larger resonator width or a longer Fabry-Perot resonator with Bragg grating reflectors on either side in order to increase the thermal conductance G to the substrate. However, the four orders of magnitude difference between $\Delta v_{\text{thermal}}$ and Δv_{ST} indicates that the required resonator would need to be cm-scale in radius or length. Such large device footprints are not desirable in the design of integrated photonic circuits due to the extremely valuable die space. However, one can in fact aim to reduce the $(1/n)(dn/dT) + \alpha_L$ term in the thermal linewidth. This term is directly related to the thermally-induced resonance shift $\Delta\lambda/\Delta T$ in equation (4.5), and therefore can be altered by the use of materials with opposite signs of thermo-optic coefficients, as will be explained in the next section.

4.4 The TiO_2-SiN Athermal Resonator

As TiO_2 is one of the most widely known materials with a negative thermo-optic coefficient (other than polymers), its use in the design of the athermal resonator is natural. In fact, there have been numerous previous demonstrations of TiO_2-clad resonators that take advantage of TiO_2's negative thermo-optic coefficient. However, as the CMOS process-flow described in the previous chapter is completed in a standardized foundry, the TiO_2 layer must again be deposited as a back-end-of-line process. Just like the laser structures, it is again beneficial to design resonators where no etch or patterning steps would be required after a blanket deposition of a TiO_2 layer, as shown by the proposed resonator design in Figure 4-6.

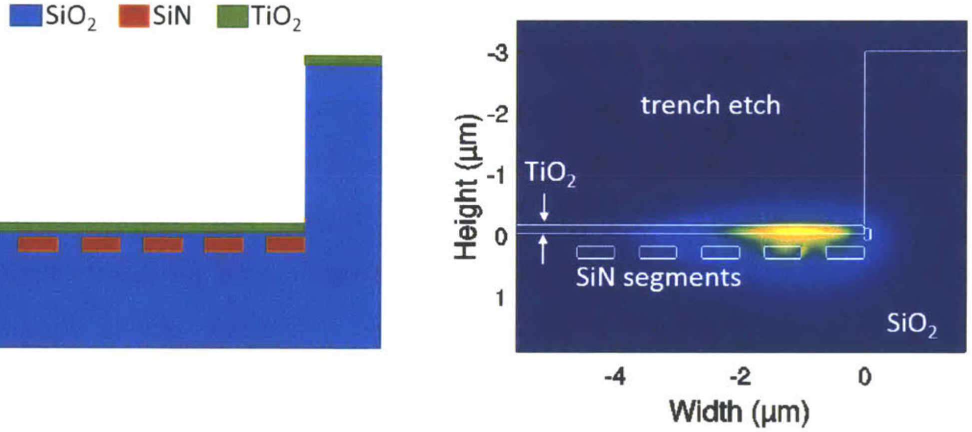

Figure 4-6: The design of the TiO_2-SiN athermal resonator with TiO_2 top layer and buried SiN segments. Electric field profile of the fundamental TE mode at 1550 nm

Here, the cross-section consists of five 600-nm-wide and 200-nm-thick segments of SiN separated by gaps of 400 nm. The sputtered layer of TiO_2 is separated from the buried SiN segments with a 200 nm thick layer of PECVD SiO_2. The trench etch on top of the SiN segments controls where the mode interacts with the TiO_2 layer, and also helps guide the whispering gallery mode with the sidewall. In this case, since TiO_2 has a significantly higher refractive index than both the SiN and SiO_2 (Table 4-1), the majority of the fundamental TE mode is confined in the TiO_2 layer. The sliver of the nitride remaining on the right of the five segments is due to the design rules on the second SiN layer being used as an etch stop, where this second nitride layer has to slightly protrude outside of the trench etch. That's the reason why a small segment of this second SiN layer remains to the right of the trench etch in Figure 4-6.

4.4.1 TiO_2 Sputtering Process

The TiO_2 layer was sputtered in the same deposition chamber as the erbium-doped lasers discussed previously. Samples were mounted upside down on the back of a 6" Si wafer, with the use of a high-temperature, silver-based, inorganic epoxy. The chamber was pumped down to a base pressure of below 10^{-6} Torr before each deposition. Ar and O_2 were introduced into the chamber using separate mass flow controllers. A titanium target with 99.999% purity was used. Plasma was ignited at a pressure of approximately 12 mT, with an initial RF power of 50 W on the Ti target. A deposition power of 400 W was used, from the 600 W power supply.

An important difference between the TiO_2 layer required for the athermal resonators and the Al_2O_3 layers required for lasers is the layer thickness. As the rare-earth doped Al_2O_3 is the gain medium for the laser, the mode has to have a large confinement in the Al_2O_3 in order to experience enough round-trip gain in the laser cavity. This requires use of micrometer-thick films, especially since Al_2O_3 has a relatively small refractive index compared to SiN, and just above that of SiO_2. On the other hand, the athermal resonator does not strictly require guiding in the TiO_2 medium. It only requires a sufficient amount of confinement to compensate for the positive thermo-optic coefficients of SiN and SiO_2. Moreover, TiO_2 has a significantly larger refractive index than both of SiN and SiO_2. Therefore, a thin layer is sufficient to provide the required confinement as shown in Figure 4-6.

Consequently, the deposition rate for the TiO_2 layer does not have to be as high as a few nm/min which is required for Al_2O_3. As a result, the TiO_2 layer was chosen to be deposited with the Ti target completely oxidized (poisoned), with an excessive amount of O_2 flow into the chamber. Compared to operating the Al target just below the O_2 flow that causes its bias to drop, an O_2 flow of 5 sccm was used for the Ti target, making the Ti bias stay as low as 150 V throughout the deposition. As a result, even though the deposition rate was much slower compared to Al_2O_3, the correct stoichiometry of TiO_2 was obtained without having to adjust O_2 flow during deposition. On average a deposition rate of 0.33 nm/min was obtained.

4.4.2 Spectral Response of the Athermal Resonator

In a multi-layered structure like the one shown in Figure 4-6, one can use the respective mode confinement in the materials to estimate the thermo-optic coefficient of the mode as

$$\frac{dn_{\text{eff}}}{dT} \approx \sum_{i=1}^{q} \Gamma_i \frac{dn_i}{dT} \tag{4.14}$$

Therefore, the larger the confinement of the mode in the TiO_2 layer, the more negative the thermo-optic coefficient will be. Since TiO_2 is deposited as a back-end process, we can exploit this fact to engineer the thermo-optic coefficient by controlling the thickness of the TiO_2 layer. In this case, using the confinement factors from the mode profile in Figure 4-6, and the approximation in equation (4.14), the required TiO_2 thickness was found to be approximately 130 nm.

After fabrication of the resonator, in order to see the amount of thermally-induced shift in the resonances, we place the fabricated resonator on a TEC stage and measure its spectral behavior with the use of a tunable continuous-wave laser operating in the C-band. By tracking a single resonance, the shifts due to thermo-optic coefficients and the thermal expansion coefficients are captured in the measurement. The tracked resonance is shown in Figure 4-7. From the 3 dB bandwidth, the loaded quality factor is calculated as $Q_l = 70{,}000$, which is almost the same as that of the SiN resonator (67,000) in Figure 4-4. The extinction ratio is 18.4 dB, which again is similar to the extinction obtained with the SiN resonator (17.9 dB). It is important to note that the TiO_2-SiN resonator was not designed or fabricated to be similar to the SiN resonator studied previously. However, in order to provide a meaningful comparison, an appropriate SiN resonator was chosen to match the quality factor and the extinction ratio from the TiO_2-SiN resonator.

From the frequency shift measurement in Figure 4-7, since the derivatives on either side of the maximum have the same order of magnitude (+50 MHz/K and -80 MHz/K), we can conclude that the linear thermal shift is practically eliminated. The frequency shift therefore now has a near-parabolic dependence with a negligible linear coefficient. This is a good approximation around the athermal operation temperature of 32 °C for this TiO_2 thickness. This suggests that by slightly adjusting the thickness of the deposited TiO_2 layer, one can shift the athermal operation point corresponding to the temperature at which the frequency shift has a near-zero derivative. However, as the linear thermo-optic coefficient has been almost completely mitigated, the amounts of change require to shift the athermal operation temperature are only a few nm. If the TiO_2 layer is much thicker than ~130 nm, then the mode gets completely confined in the TiO_2 core, and therefore exhibits a negative thermal dependence by the approximation in equation (4.14).

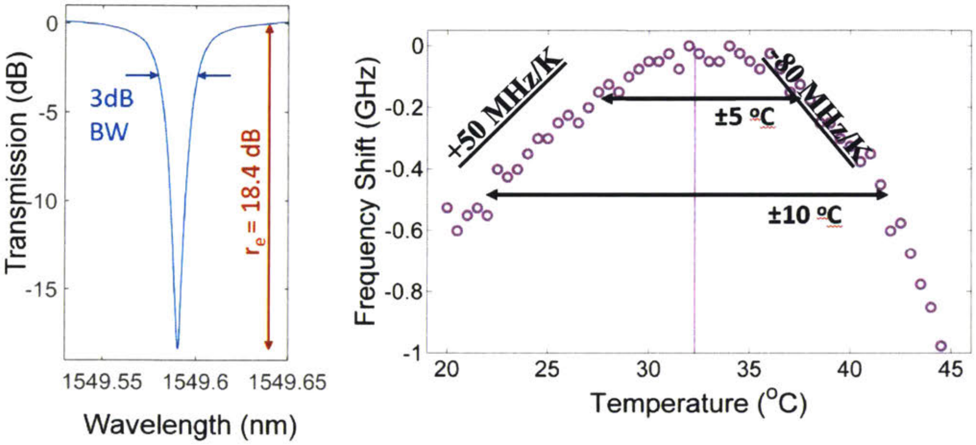

Figure 4-7: Tracked resonance of the athermal resonator, and the frequency shift of the resonance as a function of temperature

In order to quantify the effects of TiO_2 thickness on the athermal response, resonators have been fabricated with slightly different thicknesses of TiO_2. The thickness for each film was characterized by using an approximately 2 cm by 2 cm Si sample that was placed in the deposition chamber together with the chips with the resonators. The thickness of the top TiO_2 layer on the Si sample was then measured using a FILMETRICS system where the reflection from the sample was characterized as a function of wavelength. This technique is similar to ellipsometry, but it instead uses a normal incidence interferometer to measure the intensity of reflected light as a function of wavelength. Then, the layer thickness and refractive index of the top layer are numerically fitted to the measured response, yielding the TiO_2 thickness in the resonators that were deposited simultaneously. A photograph of this normal-incidence interferometer and an example measurement and fit are shown in Figure 4-8.

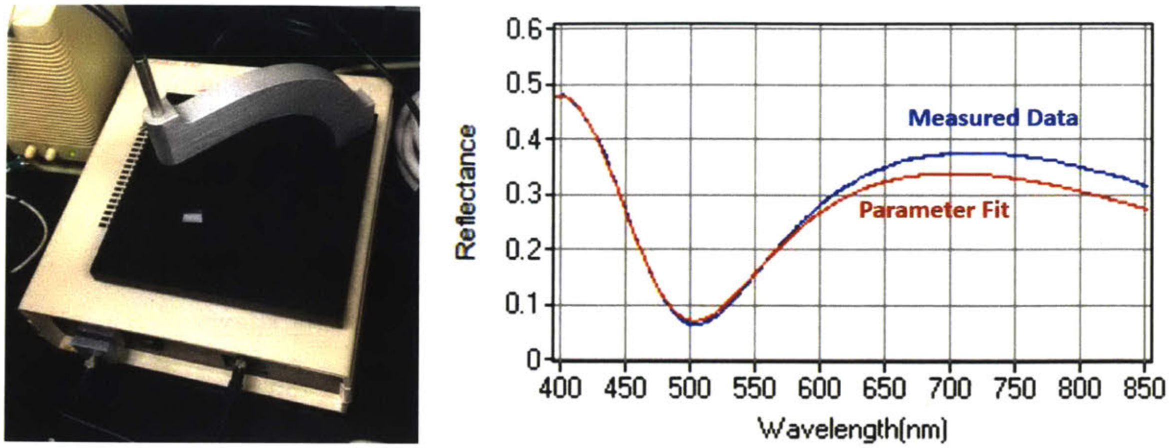

Figure 4-8: The normal-incidence interferometer for measuring the thickness of the sputtered TiO_2 layer with an example measurement and fit

The spectral response of the resonators were characterized for TiO_2 layer thicknesses of 125 nm, 130 nm, 134 nm, and 139 nm. As before, one resonance in the C-band was identified and tracked as a function of temperature. The resulting frequency shifts are plotted in Figure 4-9. For each tracked resonance, the frequency shift has been centered at zero at the vertex of the parabola where the resonator operates athermally. With increasing TiO_2 thickness, the athermal operation temperature shifts to the right towards higher temperatures. The explanation for this shift follows here: Consider the athermal operation point around 28 °C for the TiO_2 thickness of 125 nm. Since the mode has zero thermo-optic shift at this temperature, a slightly thicker layer of TiO_2 would introduce an overall negative thermo-optic coefficient for the guided mode. A negative thermo-optic coefficient means a negative shift in the resonance wavelength with increased temperature, and a corresponding positive shift in the resonance frequency. A positive derivative of frequency shift corresponds to having the rising edge of the parabola at the previous athermal operation temperature of 28 °C (green). That indicates the vertex of the parabola must shift to higher temperatures, leaving the rising edge around the previous vertex. This corresponds to a frequency shift curve that is shifted to the right, as shown by any of the other examples with 130 nm (blue), 134 nm (purple), and 139 nm (red).

Being able to fabricate resonators with "adjustable" athermal operation temperatures is useful in applications where the operation temperature may be different than room temperature due to environmental conditions, or the amount of optical power inside the resonator. This TiO_2 thickness is easily controlled by adjusting the deposition time on the resonators, and can be used as an effective means of controlling temperature dependence of spectral response. In the next section, we utilize these athermal resonators and the implications of the thermally-dominated phase noise in SiN resonators to stabilize and analyze an external laser.

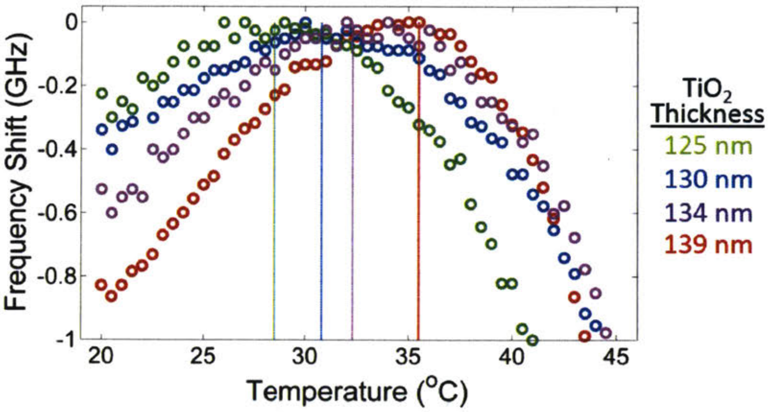

Figure 4-9: Frequency shift of the tracked resonance as a function of temperature for four different TiO_2 thicknesses indicating the influence of layer thickness on athermal operating temperature

4.5 Laser Stabilization using the Athermal Resonator

Since we know that the phase noise in a typical SiN resonator is dominated by the thermal component, we can use the athermal resonator as a reference cavity to thermally stabilize a laser. This is achieved by using the Pound-Drever-Hall technique [76] where a laser is locked to a reference cavity by means of identifying and minimizing an error signal corresponding to the mismatch of the laser line and the resonator reference. Apart from the original reference given above, many other papers can be found discussing the operation principles and details of the locking technique with applications in not only laser stabilization [77], but also in interferometry [78], spectroscopy [79, 80], and sensing [81, 82].

In general, the Pound-Drever-Hall technique relies on phase modulating an optical signal and identifying the spectral positions of the generated sidebands with respect to a reference resonance. Near resonance, as the phase response of the resonator has opposite signs on either side of the resonance, one can use the sidebands in order to identify how close to and on which side of the reference the laser line is spectrally located. The error signal is generated by detecting the reflected or transmitted light from the resonator with the use of a photodetector. This error is then mixed down to baseband using the local oscillator driving the phase modulator. Any harmonics at multiples of the local oscillator frequency are electrically filtered. Finally, using a controller and the modified baseband error signal, a modulation feedback is produced to spectrally shift the source laser to the reference resonance. When the laser lines up with this resonance, as the sidebands are equally separated from the reference, the generated error signal is zero. More details and mathematical analyses can be found in the references above [77-82].

4.5.1 Pound-Drever-Hall Locking Loop

A schematic of the constructed Pound-Drever-Hall locking setup is shown in Figure 4-10 where green indicates optical instruments and fibers, and blue indicates electrical instruments and RF cable (BNC/SMA). In the first part of the setup indicated by the red dashed box, in addition to the athermal resonator developed here, we used an Anritsu C-band continuous-wave tunable laser, a fiber-coupled phase modulator, and standard SMF-28 fiber patchcords. The light from the CW laser was first amplified with the use of an EDFA to mitigate the coupling losses from fiber-to-fiber connections as well as the on- and off-chip coupling losses. The phase modulator was driven by a 10 GHz local oscillator. Since the phase modulator required a TE input, we used a polarization controller between the CW laser and the modulator. If the output from the laser is TE polarized, one can also use polarization maintaining fiber between the laser and the phase modulator. The modulated signal is then coupled on-chip with the use of another fiber and another polarization controller. The reason for the second polarization controller is that all the waveguides on-chip are designed to guide TE modes. If available, one could also use polarization maintaining fiber between the modulator and the on-chip resonator. Modulated TE light is coupled on and off the Si chip with the use of inverted facet tapers. The transmitted signal at the through port of the athermal resonator is collected by another fiber at the output of the chip and detected by a fiber coupled 22 GHz photodetector. The transmitted signal of a ring resonator has a spectral response similar to the reflected signal from a Fabry-Perot resonator that many Pound-Drever-Hall references use. After detecting, the error signal is still at the modulation frequency, and has to be extracted from the AC component of the detected signal. The photodetector output is therefore separated into its AC and DC components with the use of a bias-tee. The AC signal carrying the high frequency error signal is then mixed with the local oscillator driving the phase modulator. The result is the error signal at the output of the mixer, but also includes harmonics of the local oscillator. These are low pass filtered to create the modified error signal that is then passed to a servo controller. The servo controller has gain and corner frequency adjustments that are used to generate the optimal feedback signal to frequency-modulate the CW laser. An oscilloscope was also added to monitor the generated error signal, the ±5 V modulation signal, and the DC power read from the photodetector.

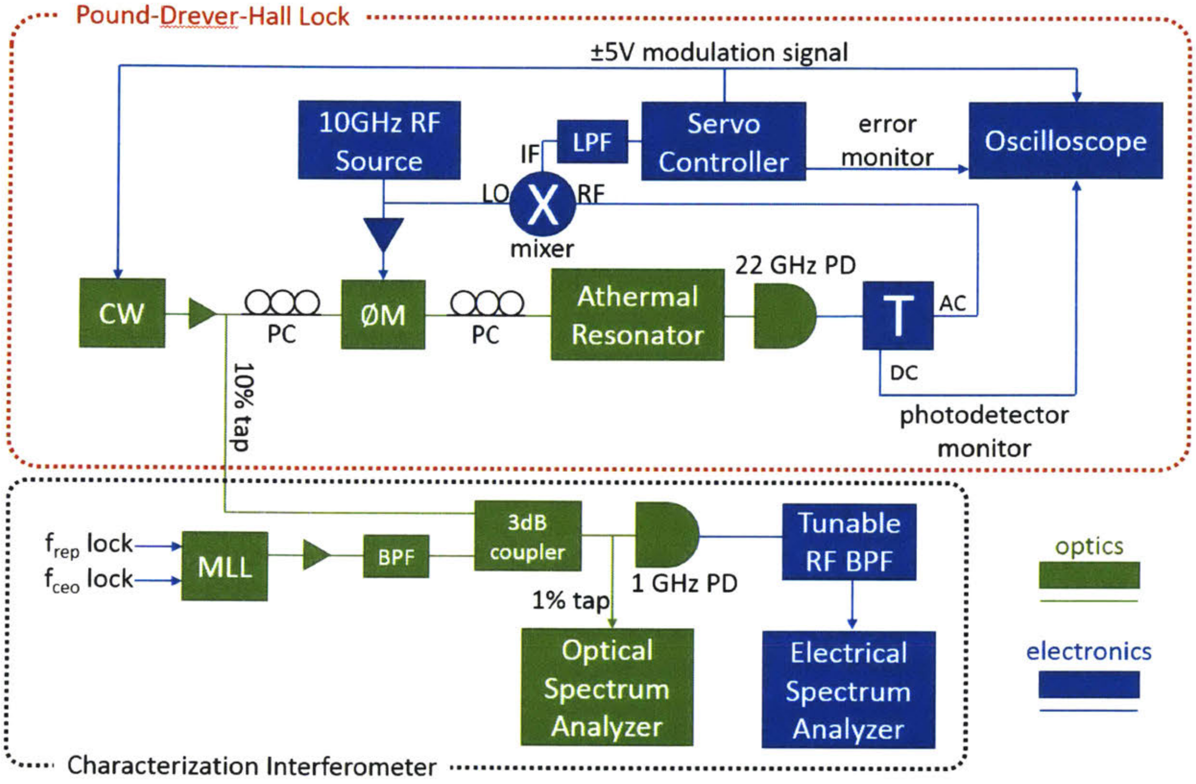

Figure 4-10: Schematic of the Pound-Drever-Hall locking mechanism of an external laser to the reference athermal resonator and the interferometer used to characterize the linewidth of the resulting locked laser line

The second part of the setup in Figure 4-10 within the black dashed box is the interferometer built to measure the spectral characteristics of the locked laser line. In this part of the setup, a stabilized Menlo Systems mode-locked laser is used as a reference frequency comb. This laser's repetition rate and carrier envelope offset are locked to external reference oscillators by means of a 1f-2f lock. The stabilized reference comb is amplified using an EDFA, and is then band-pass filtered in the optical domain with a tunable, fiber-coupled filter to spectrally match with the laser line. Using a 3 dB coupler, the 1f-2f locked comb and the resonator-stabilized laser line are then combined on the same fiber, and then detected using a lower speed photodetector. This second photodetector only has to be able to detect within the repetition rate of the comb, and can therefore be lower speed. In this case, the repetition rate was locked to 250 MHz. Finally, the detected beat note is filtered to suppress any other beat notes by the interference of the laser line with the other comb lines, and analyzed with an Agilent electrical spectrum analyzer. There is also a 1 % tap before the second photodetector where the combined signal is input into an optical spectrum analyzer. This allows for the tunable filter to be tuned while observing the comb output to make sure that it spectrally matches with the laser signal from the Pound-Drever-Hall loop.

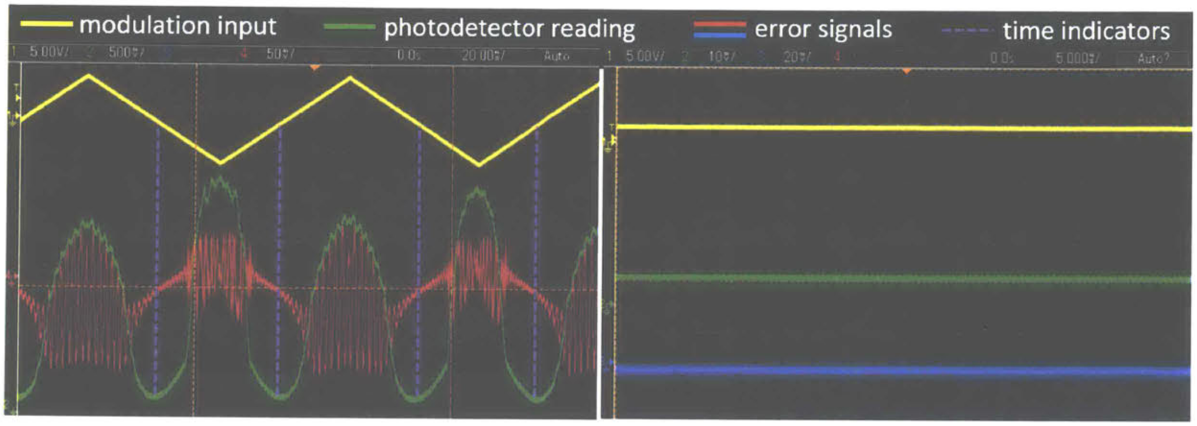

Before Lock **After Lock**

Figure 4-11: Oscilloscope traces of the modulation input, the photodetector reading, and the error signals before and after the Pound-Drever-Hall lock is established

In order to start frequency locking using the Pound-Drever-Hall loop, the laser is first coarsely tuned close to one of the resonances of the reference athermal resonator. Then, using a triangle waveform, the laser frequency is modulated back and forth to capture the resonance. This is shown in the oscilloscope trace in Figure 4-11 recorded before the lock was engaged. In each ramp-up/ramp-down cycle of the driving signal, there is a point at which the photodetector reading (green-left) goes to its minimum, and the error signal (red/pink) crosses zero. These are marked with the time indicators (purple) and indicate when the laser exactly lines up with the reference resonance. At this wavelength, since most of the light is coupled to the resonator, the intensity at the through port goes to a minimum as indicated by the photodetector reading.

The lock is established by turning off the triangular modulation signal and turning on the servo controller to provide the necessary feedback signal to the tunable laser. Once the servo controller comes online, the error signal (blue) remains near zero, and the photodetector reading (green-right) stays relatively constant. This lock can sustain itself for more than two hours if the

RF cables and fibers are not moved. The longevity of the stabilized signal depends on environmental factors such as vibration of the optical table or the cables/fibers. The movement of the fiber cantilevers for on-chip coupling also affects lock performance as movement of the cantilevers changes the amount of optical power at the athermal resonator. It may be possible to further isolate the system from vibration and wind by building a foam or plexiglass housing in order to extend the lock's lifetime.

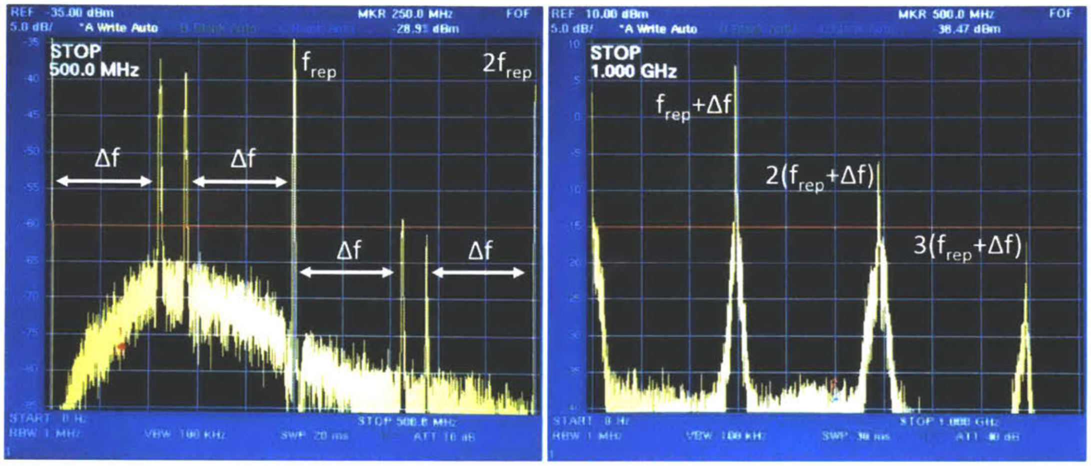

Figure 4-12: Electrical spectrum of the beat note between CW laser and stabilized comb before and after the tunable RF filter

4.5.2 Analysis and Characterization of Laser Linewidth

In an interferometric analysis between a CW laser and a comb, there are many beat notes generated. The strongest and the most narrowband beat notes generated are between the individual comb lines themselves at integer multiples of the repetition rate: 250 MHz (f_{rep}), 500 MHz ($2f_{rep}$), etc. These are observed in the example electrical spectrum reading shown on the left in Figure 4-12. The beat notes between a comb line and the CW signal are observed at Δf, $f_{rep} \pm \Delta f$, $2f_{rep} \pm \Delta f$, $3f_{rep} \pm \Delta f$, etc. The periodic nature of the beat notes comes from the fact that the laser line interferes not only with the comb line closest to it, but with all comb lines. For spectrum analysis, one of the comb lines is then filtered using a tunable analog RF filter. The output of the filter is shown on the right in Figure 4-12, where harmonics of the filtered line appear as artifacts. Then, the first beat note at $f_{rep} + \Delta f$ is analyzed further with a high-resolution spectrum analyzer.

To establish a baseline for the performance of the athermal resonator, the Anritsu CW laser is first tested in its free-running condition, without being locked to a reference cavity. The beat note is analyzed as described above, and the measured spectrum is plotted in red in Figure 4-13. The spectrum is fit with a Lorentzian lineshape, yielding a linewidth of 4.79 MHz, which is expected from a typical benchtop laser. The spectrum is measured again after the laser is locked to a conventional SiN cavity whose response was shown in Figure 4-4. The measured linewidth in this case is 1.91 MHz, which is similar to the 1.6 MHz expected thermal noise dominated linewidth calculated for this resonator in Section 4.3. Finally, the linewidth measurement is performed with the laser locked to the the TiO_2-SiN athermal resonator. The measured linewidth decreases further by a factor of 6 to 0.34 MHz, significantly below the thermal limit of 1.6 MHz of the SiN resonator. This proves that the athermal design can effectively suppress the phase noise due to thermal fluctuations.

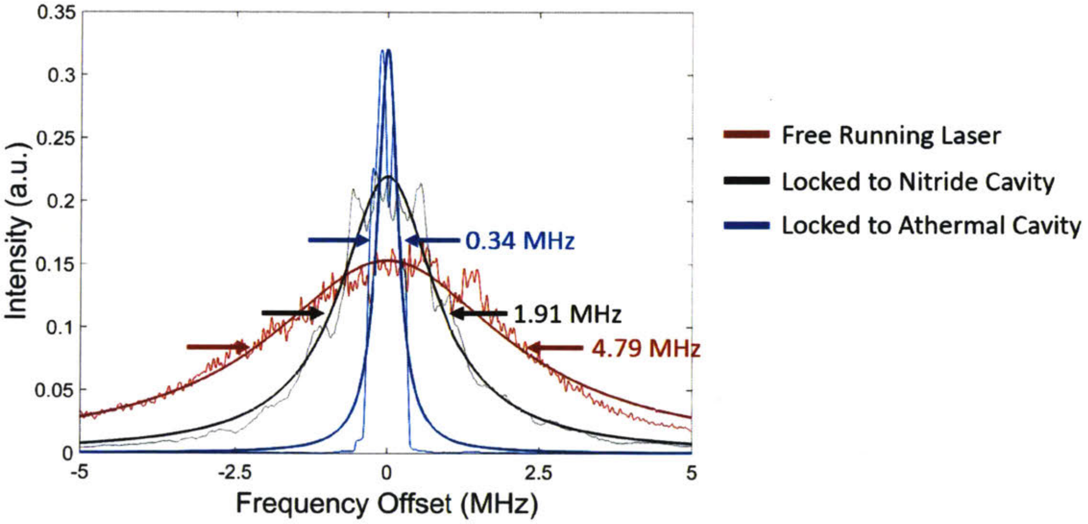

Figure 4-13: Spectrum and linewidth of the beat note between a stabilized comb and a CW laser while free-running (red), locked to a SiN cavity (black), and locked to a TiO_2-SiN athermal cavity (blue)

One can also plot the data in Figure 4-13 in terms of phase noise power spectral density. This is a measure of how much power a signal has at a frequency offset of f from the carrier ν_{CW}, and here is given in units of "dB with respect to carrier" (dBc). The result is shown in Figure 4-14. As also indicated by the linewidth measurement, the laser carries much less power at frequencies far away from the carrier when it is locked to the athermal cavity. Compared to the free-running laser, the regular SiN cavity can suppress power at a 1 MHz offset by approximately 7 dB, whereas the suppression increases to more than 25 dB with the athermal cavity. Improved suppression of phase noise proves how effective the athermal resonator is in compensating for thermal fluctuations and resulting spectral drifts.

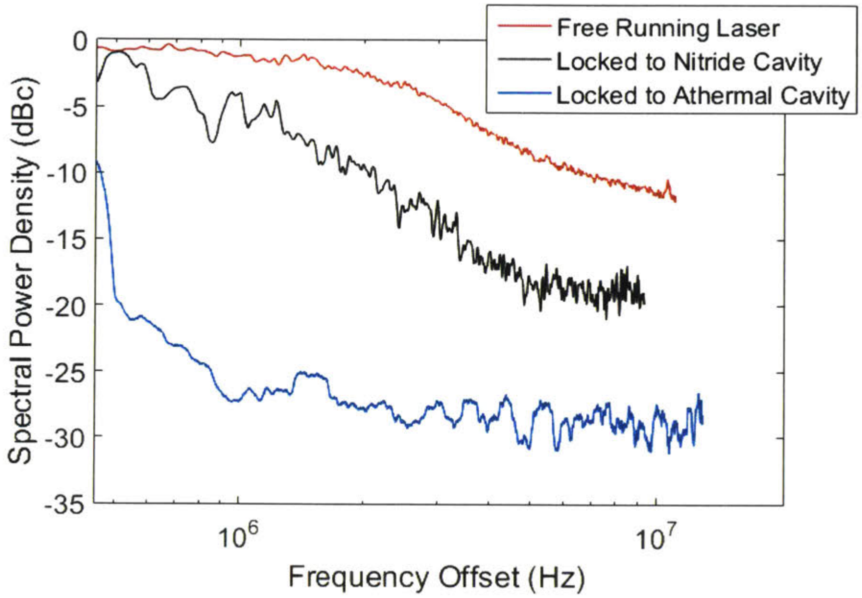

Figure 4-14: Single side-band phase noise power spectral density of the free-running and locked laser signals

4.6 Conclusion

We showed that thermal fluctuations make up one of the most important sources of phase noise in resonators. To investigate the contribution of thermal noise, we compared the Schawlow-Townes linewidth and the thermal linewidth for a laser line locked to a typical buried SiN resonator with 80 μm radius. As $\Delta\nu_{ST} \approx 300\text{Hz} \ll \Delta\nu_{\text{thermal}} \approx 1.6\text{MHz}$ we concluded that the noise in the SiN resonator is thermally dominated in its phase noise. Since most Si resonators are smaller due to high confinement, and as Si's thermo-optic coefficient is much larger, Si resonators are even more highly dominated by thermal noise. In order to address these noise limitations, we designed and fabricated an athermal resonator with a TiO_2 top layer that was deposited as a back-end of line process. The resonator was characterized by tracing one of its resonances in the C-band while changing its temperature by means of a TEC. With the appropriate thickness of the TiO_2 layer, the linear thermo-optic shift has been completely eliminated. Moreover, we showed that the temperature range around which the resonator operates completely athermally can be shifted by changing the thickness of the top TiO_2 layer.

This provides flexibility in that the resonator response can be modified with the use of an etch-free & lithography-free back-end step.

Using the athermal TiO_2-SiN resonator, we constructed a Pound-Drever-Hall frequency locking experiment where we locked a tunable benchtop laser to the fabricated athermal resonator. The performance of the athermal resonator was then characterized by means of interfering the locked CW signal with a reference comb whose repetition rate and carrier envelope offset were locked using a 1f-2f interferometer. Compared to the free-running linewidth of 4.79 MHz, the regular SiN resonator was able to lock the laser to a linewidth of 1.91 MHz, whereas the athermal resonator achieved 0.34 MHz. With the use of the athermal reference, the linewidth of the laser was narrowed below the expected thermal linewidth of 1.6 MHz from a regular SiN resonator. The single sideband phase noise was suppressed by more than 25 dB with respect to the free-running laser, and more than 18 dB with respect to the SiN cavity. These results show how powerful athermal resonators can be in suppressing thermal noise. One can use similar techniques to build integrated systems that can utilize the Pound-Drever-Hall technique to lock on-chip lasers to on-chip athermal resonators. Resulting narrow linewidth lasers can be used in integrated coherent communication or detection applications that suffer from thermal fluctuations.

5 COUPLED-MODE APPLICATIONS IN SPECTRAL SELECTIVITY

In this chapter, we review the basics of coupled mode theory and utilize it for designing devices that achieve broadband integrated spectral selectivity. Comparisons to typical directional couplers as well as more advanced structures are provided.

5.1 Understanding Coupled-Mode Theory

For the purposes of the devices studied in this chapter, coupled mode theory refers to coupling of guided modes in space in periodic steady state. This is illustrated in Figure 5-1, as reproduced from Haus's iconic textbook [83]. In this scenario, we will refer to the guided modes of the whole structure as ψ_+ and ψ_-, whereas the guided modes of the individual waveguides will be referred to as ψ_A and ψ_B (for Waveguides A and B respectively). Crucially, for the structure given in Figure 5-1, ψ_A and ψ_B are not eigenmodes, and do not obey the wave equation in this geometry. On the other hand, as ψ_+ and ψ_- are in fact orthogonal eigenmodes of the structure, they obey the equations

$$\frac{d}{dz}\psi_+ = -j\beta_+\psi_+ \tag{5.1}$$

and

$$\frac{d}{dz}\psi_- = -j\beta_-\psi_- \tag{5.2}$$

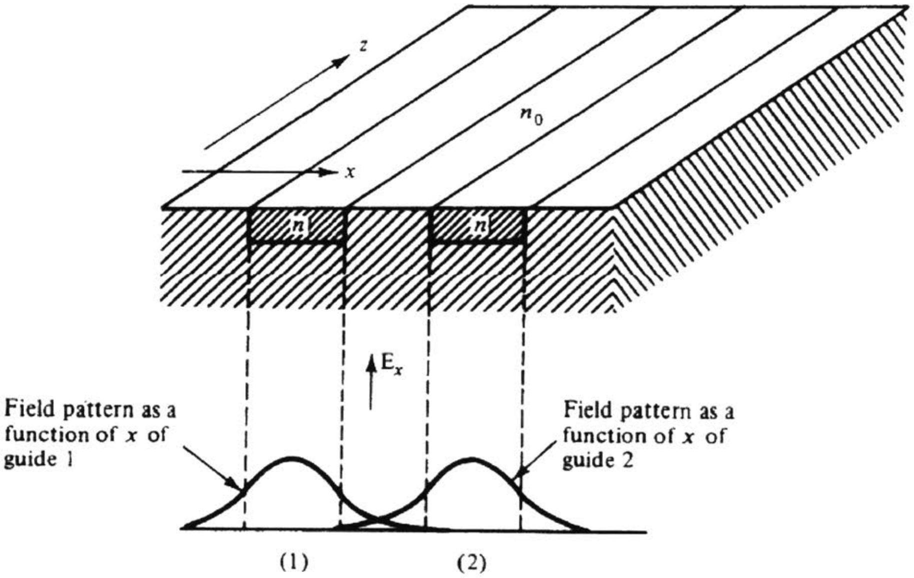

Figure 5-1: Cross-sectional view of the index profile of two waveguides and their coupled guided modes, reproduced from [83]

In equations (5.1) and (5.2), β_+ and β_- are the propagation constants of ψ_+ and ψ_- respectively. Here, just like the eigenmodes of any waveguide, ψ_+ and ψ_- are not coupled. We can represent these eigenmodes of the combined structure (also called supermodes, or even/odd modes) with exponentials forms as solutions to (5.1) and (5.2):

$$\psi_+ = q_+e^{-j\beta_+z} \qquad \text{and} \qquad \psi_- = q_-e^{-j\beta_-z} \tag{5.3}$$

where we assigned the amplitudes q_+ and q_-.

In contrast, since ψ_A and ψ_B are in fact coupled, they are not orthogonal; and they obey a different set of equations:

$$\frac{d}{dz}\psi_A = -j\beta_A\psi_A + \kappa_{AB}\psi_B \tag{5.4}$$

and

$$\frac{d}{dz}\psi_B = -j\beta_B\psi_B + \kappa_{BA}\psi_A \tag{5.5}$$

Here, we similarly defined the propagation constants β_A and β_B for modes ψ_A and ψ_B, and the coupling coefficients κ_{AB} and κ_{BA} between the two waveguides.

If the coupling between the two waveguides is weak, we can represent the supermodes ψ_+ and ψ_- as linear combinations of the individual modes ψ_A and ψ_B [84]:

$$\begin{bmatrix}\psi_+\\ \psi_-\end{bmatrix} = \begin{bmatrix}a_+ & b_+\\ a_- & b_-\end{bmatrix}\begin{bmatrix}\psi_A\\ \psi_B\end{bmatrix} \tag{5.6}$$

Taking the derivative in equation (5.6), and using the results from equations (5.1), (5.2), (5.4), and (5.5), we get

$$\frac{d}{dz}\begin{bmatrix}\psi_+\\ \psi_-\end{bmatrix} = \begin{bmatrix}a_+ & b_+\\ a_- & b_-\end{bmatrix}\frac{d}{dz}\begin{bmatrix}\psi_A\\ \psi_B\end{bmatrix} = \begin{bmatrix}a_+ & b_+\\ a_- & b_-\end{bmatrix}\begin{bmatrix}-j\beta_A & \kappa_{AB}\\ \kappa_{BA} & -j\beta_B\end{bmatrix}\begin{bmatrix}\psi_A\\ \psi_B\end{bmatrix} \tag{5.7}$$

Multiplying out the matrices yields

$$-j\begin{bmatrix}\beta_+\psi_+\\ \beta_-\psi_-\end{bmatrix} = \begin{bmatrix}-j\beta_A a_+ + \kappa_{BA}b_+ & -j\beta_B b_+ + \kappa_{AB}a_+\\ -j\beta_A a_- + \kappa_{BA}b_- & -j\beta_B b_- + \kappa_{AB}a_-\end{bmatrix}\begin{bmatrix}\psi_A\\ \psi_B\end{bmatrix} \tag{5.8}$$

In this system, it is convenient to represent the modes using the basis vectors ψ_A and ψ_B. Then, we have

$$\psi_A = \begin{bmatrix}1\\ 0\end{bmatrix}, \qquad \psi_B = \begin{bmatrix}0\\ 1\end{bmatrix}, \qquad \psi_+ = \begin{bmatrix}a_+\\ b_+\end{bmatrix}, \qquad \psi_- = \begin{bmatrix}a_-\\ b_-\end{bmatrix} \tag{5.9}$$

Using the newly defined basis, each row from the matrix equation (5.8) then reads

$$-j\beta_+\psi_+ = \begin{bmatrix}-j\beta_A a_+ + \kappa_{BA}b_+\\ -j\beta_B b_+ + \kappa_{AB}a_+\end{bmatrix} = \begin{bmatrix}-j\beta_A & \kappa_{BA}\\ \kappa_{AB} & -j\beta_B\end{bmatrix}\begin{bmatrix}a_+\\ b_+\end{bmatrix} = \begin{bmatrix}-j\beta_A & \kappa_{BA}\\ \kappa_{AB} & -j\beta_B\end{bmatrix}\psi_+ \tag{5.10}$$

and

$$-j\beta_+\psi_- = \begin{bmatrix}-j\beta_A a_- + \kappa_{BA}b_-\\ -j\beta_B b_- + \kappa_{AB}a_-\end{bmatrix} = \begin{bmatrix}-j\beta_A & \kappa_{BA}\\ \kappa_{AB} & -j\beta_B\end{bmatrix}\begin{bmatrix}a_-\\ b_-\end{bmatrix} = \begin{bmatrix}-j\beta_A & \kappa_{BA}\\ \kappa_{AB} & -j\beta_B\end{bmatrix}\psi_- \tag{5.11}$$

We can summarize equations (5.10) and (5.11) in a single eigenvalue equation as follows:

$$\begin{bmatrix}-j\beta_A & \kappa_{BA}\\ \kappa_{AB} & -j\beta_B\end{bmatrix}\psi_\pm = -j\beta_\pm\psi_\pm \tag{5.12}$$

5.1.1 Propagation Constants of Supermodes

By power conservation, for waveguides carrying power in the same direction,

$$\kappa_{AB}\kappa_{BA} = -|\kappa_{AB}|^2 \Longrightarrow \kappa_{AB} = -\kappa_{BA}^* \tag{5.13}$$

Conversely, for waveguides carrying power in opposite directions, we have

$$\kappa_{AB}\kappa_{BA} = |\kappa_{AB}|^2 \Longrightarrow \kappa_{AB} = \kappa_{BA}^* \tag{5.14}$$

Here, we will consider the case of a co-directional (or simply directional) coupler where the propagation direction in the two coupled waveguides are the same. Then, equation (5.12) can be rewritten as

$$\begin{bmatrix} -j\beta_A & j\kappa^* \\ j\kappa & -j\beta_B \end{bmatrix} \psi_\pm = -j\beta_\pm \psi_\pm \tag{5.15}$$

where we let $j\kappa \equiv \kappa_{AB} = -\kappa_{BA}^*$. We then divide both sides by j and rearrange to obtain

$$\begin{bmatrix} \beta_\pm - \beta_A & \kappa^* \\ \kappa & \beta_\pm - \beta_B \end{bmatrix} \psi_\pm = 0 \tag{5.16}$$

We then define the following variables

$$\overline{\beta} = \frac{\beta_A + \beta_B}{2}, \qquad \delta = \frac{\beta_A - \beta_B}{2}, \qquad S^2 = \delta^2 + |\kappa|^2 \tag{5.17}$$

and rewrite equation (5.16) as

$$\begin{gathered} \begin{bmatrix} \overline{\beta} + \delta & -\kappa^* \\ -\kappa & \overline{\beta} - \delta \end{bmatrix} \psi_\pm = \beta_\pm \psi_\pm \\ \begin{bmatrix} \beta_\pm - (\overline{\beta} + \delta) & \kappa^* \\ \kappa & \beta_\pm - (\overline{\beta} - \delta) \end{bmatrix} \psi_\pm = 0 \end{gathered} \tag{5.18}$$

Setting the determinant to zero, we get

$$\begin{gathered} [\beta_\pm - (\overline{\beta} + \delta)][\beta_\pm - (\overline{\beta} - \delta)] - |\kappa|^2 = 0 \\ \Longrightarrow \beta_\pm^2 - 2\beta_\pm\overline{\beta} + \overline{\beta}^2 - \delta^2 - |\kappa|^2 = 0 \Longrightarrow (\beta_\pm - \overline{\beta})^2 = \delta^2 + |\kappa|^2 \end{gathered} \tag{5.19}$$

Then, the eigenvalues are given by

$$\beta_\pm = \overline{\beta} \pm \sqrt{\delta^2 + |\kappa|^2} = \overline{\beta} \pm S \tag{5.20}$$

Although equation (5.20) is by far the most common expression used for the eigenmodes in a coupled waveguide structure, most applications today allow one to solve for the supermode propagation constants using a 1D or 2D mode solver. The coupling coefficient on the other hand requires an overlap integral of the individual modes. That's why it is useful to use the definition of the supermode propagation constants and solve for the coupling coefficient $|\kappa|$ as

$$4|\kappa|^2 = 4S^2 - 4\delta^2 = (\beta_+ - \beta_-)^2 - 4\delta^2 \tag{5.21}$$

For most typical applications such as basic directional couplers, in the case that the two individual waveguides are the same, $\delta = 0$, and $2|\kappa| = 2S = \beta_+ - \beta_-$.

5.1.2 Supermodes as Eigenvectors

So far, the discussion has been limited to $\beta_\pm$, as the propagation constants of the two supermodes are extremely useful in designing devices and calculating interaction lengths. However, the propagation constants alone cannot determine the ratio of optical power in each individual waveguide. That requires solving for the eigenvectors from equation (5.18).

For the first eigenvalue $\beta_+ = \overline{\beta} + S$, we have

$$\begin{bmatrix} (\overline{\beta} + S) - (\overline{\beta} + \delta) & \kappa^* \\ \kappa & (\overline{\beta} + S) - (\overline{\beta} - \delta) \end{bmatrix} \psi_+ = 0 \tag{5.22}$$

Solving directly for the eigenvector ψ_+ yields

$$\psi_+ = x_+ \begin{bmatrix} -(S + \delta)/\kappa \\ 1 \end{bmatrix} \tag{5.23}$$

Similarly, we can solve for ψ_- using $\beta_- = \overline{\beta} - S$:

$$\begin{bmatrix} (\overline{\beta} - S) - (\overline{\beta} + \delta) & \kappa^* \\ \kappa & (\overline{\beta} - S) - (\overline{\beta} - \delta) \end{bmatrix} \psi_- = 0 \tag{5.24}$$

yielding

$$\psi_- = x_- \begin{bmatrix} (S - \delta)/\kappa \\ 1 \end{bmatrix} \tag{5.25}$$

In equations (5.23) and (5.25), we introduced x_+ and x_- as normalization constants. Since ψ_A and ψ_B are already normalized in their own basis in equation (5.9), we then force normalization of the supermodes in the following form:

$$|a_+|^2 + |b_+|^2 = 1 \qquad \text{and} \qquad |a_-|^2 + |b_-|^2 = 1 \tag{5.26}$$

This yields

$$x_+^2\left(\left(\frac{S+\delta}{\kappa}\right)^2 + 1\right) = 1 \Rightarrow x_+ = \frac{\kappa}{\sqrt{2S(S+\delta)}} \tag{5.27}$$

Similarly, for x_-, we have

$$x_-^2\left(\left(\frac{S-\delta}{\kappa}\right)^2 + 1\right) = 1 \Rightarrow x_- = \frac{\kappa}{\sqrt{2S(S-\delta)}} \tag{5.28}$$

Plugging x_+ and x_- from equations (5.27) and (5.28) into the eigenvectors ψ_+ and ψ_- in (5.23) and (5.25), we get

$$\psi_+ = \begin{bmatrix} \dfrac{-\kappa}{\sqrt{2S(S+\delta)}}\dfrac{(S+\delta)}{\kappa} \\ \dfrac{\kappa}{\sqrt{2S(S+\delta)}} \end{bmatrix} = \frac{1}{\sqrt{2}}\begin{bmatrix} -\sqrt{(S+\delta)/S} \\ \sqrt{(S-\delta)/S} \end{bmatrix} = \frac{1}{\sqrt{2}}\begin{bmatrix} -\sqrt{1+\delta/S} \\ \sqrt{1-\delta/S} \end{bmatrix} \tag{5.29}$$

and

$$\psi_- = \begin{bmatrix} \dfrac{\kappa}{\sqrt{2S(S-\delta)}}\dfrac{(S-\delta)}{\kappa} \\ \dfrac{\kappa}{\sqrt{2S(S-\delta)}} \end{bmatrix} = \frac{1}{\sqrt{2}}\begin{bmatrix} \sqrt{(S-\delta)/S} \\ \sqrt{(S+\delta)/S} \end{bmatrix} = \frac{1}{\sqrt{2}}\begin{bmatrix} \sqrt{1-\delta/S} \\ \sqrt{1+\delta/S} \end{bmatrix} \tag{5.30}$$

Equations (5.29) and (5.30) are the normalized representations of the even and odd supermodes in the basis of the individual waveguide modes. This representation is useful in determining how much of the light in a supermode actually is in one of the individual eigenmodes. Answering this question is also important in calculating how much of the optical power in a supermode remains in either one of the coupled waveguides.

5.1.3 Power Distribution in Coupled Waveguides

In order to solve for how much power remains in one waveguide, we need to evaluate the inner products of the supermodes with the individual modes. For instance, to calculate how much of the power in the even supermode remains in Waveguide A (WG_A), we evaluate the inner product of the even supermode with the guided mode in WGA (ψ_A):

$$\begin{aligned} T_{+A} &= \left|\frac{\psi_A \cdot \psi_+}{\psi_+ \cdot \psi_+}\right|^2 = \frac{1}{2}\left(1 + \frac{\delta}{S}\right) = \frac{1}{2}\left(1 + \frac{\delta}{\sqrt{\delta^2 + |\kappa|^2}}\right) = \frac{1}{2}\left(1 + \frac{\gamma}{\sqrt{1 + \gamma^2}}\right) \\ &= \frac{1}{2}(1 + \sin(\arctan\gamma)) \end{aligned} \tag{5.31}$$

where T_{+A} is transmission for WGA for the even supermode, $\psi_A \cdot \psi_+$ and $\psi_+ \cdot \psi_+$ are inner products, and we defined the dimensionless quantity $\gamma = \delta/|\kappa|$. Similarly, for the Waveguide B whose individual guided mode is ψ_B, we get

$$\begin{aligned} T_{+B} &= \left|\frac{\psi_B \cdot \psi_+}{\psi_+ \cdot \psi_+}\right|^2 = \frac{1}{2}\left(1 - \frac{\delta}{S}\right) = \frac{1}{2}\left(1 - \frac{\delta}{\sqrt{\delta^2 + |\kappa|^2}}\right) = \frac{1}{2}\left(1 - \frac{\gamma}{\sqrt{1 + \gamma^2}}\right) \\ &= \frac{1}{2}(1 - \sin(\arctan\gamma)) \end{aligned} \tag{5.32}$$

For the odd supermode ψ_-, the transmission are given by

$$T_{-A} = \left|\frac{\psi_A \cdot \psi_-}{\psi_- \cdot \psi_-}\right|^2 = T_{+B} \qquad \text{and} \qquad T_{-B} = \left|\frac{\psi_B \cdot \psi_-}{\psi_- \cdot \psi_-}\right|^2 = T_{+A} \tag{5.33}$$

It is easily confirmed that

$$T_{+A} + T_{+B} = T_{-A} + T_{-B} = 1 \tag{5.34}$$

satisfying conservation of power in the two coupled waveguides.

We can now plot equations (5.20) and (5.31) and interpret various implications that changing propagation constants may have on the power distribution behavior. In Figure 5-2, we plot the propagation constants of the even and odd supermodes in a coupled waveguide geometry. Here, for simplicity, we assumed a constant coupling coefficient κ although a varying κ can also be easily used. The plot can be interpreted in multiple ways:

1. The horizontal axis is frequency: In typical symmetric dielectric waveguides, the propagation constant reduces with increasing wavelength or decreasing frequency. However, the speed at which the propagation constant changes depends on the group velocity and dispersion of the specific waveguides. If at some wavelength, γ is small (the difference between the propagation constants is small and there is a sufficient amount of coupling between the two waveguides), then the guided modes will hybridize as shown in Figure 5-2, reproduced from [83]. The profiles of β_+ and β_- will start to differ from the propagation constants of the individual guided modes β_A and β_B (dashed lines). β_+ will always be larger than the larger one of β_A and β_B. One can think of the coupling between the two waveguides as a mechanism to push apart the propagation constants. With larger coupling coefficients, the difference between β_+ and β_- will grow, as can be seen from equation (5.20). Consequently, a larger coupling coefficient will also increase the difference from the supermode propagation constants to both β_A and β_B.

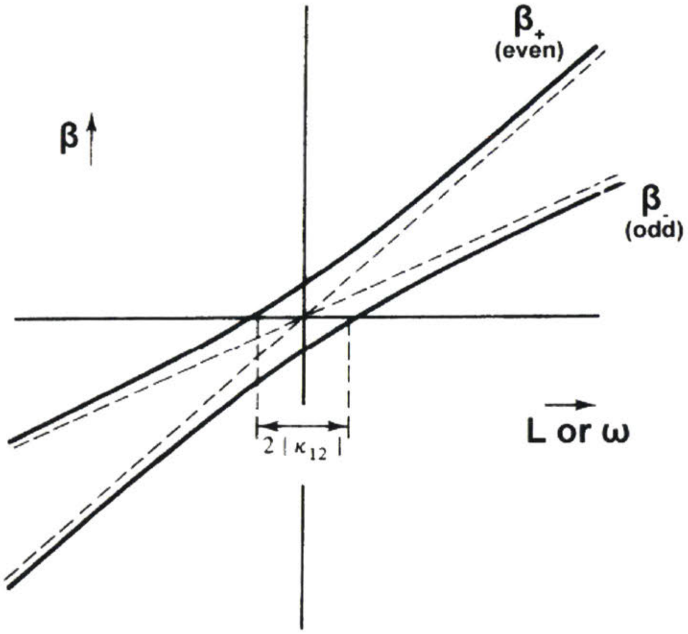

Figure 5-2: Propagation constants of coupled modes, reproduced from [83]

2. The horizontal axis is propagation along the device: It is also possible to interpret Figure 5-2 as the changing propagation constants along the propagation direction in a device due to changing geometry. Such changes in propagation constants can be easily achieved by changing widths in integrated waveguides. An example is shown in Figure 5-3 where one

waveguide has constant width, and the other has varying width along the propagation direction. In this case, the two coupled modes would hybridize at $z = z_0$ where they have equal width, and therefore equal propagation constants.

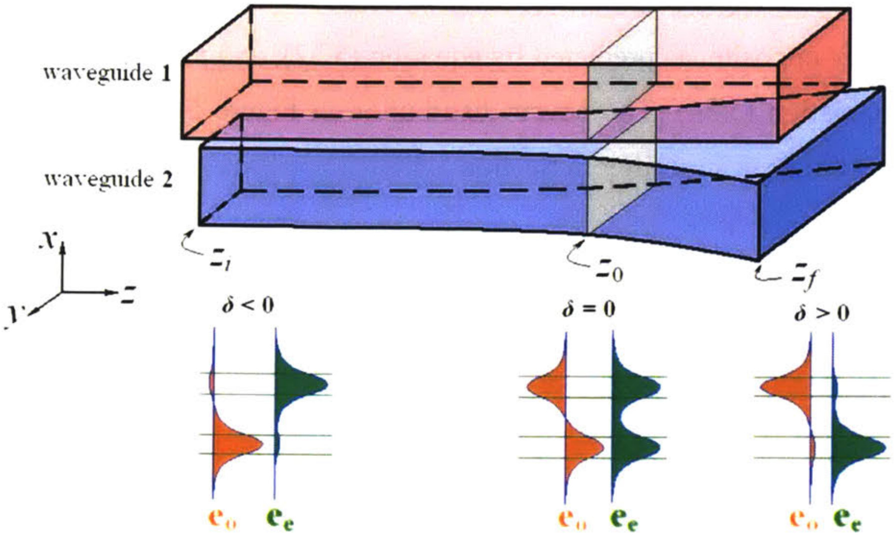

Figure 5-3: Two example waveguides one of which has changing width along the propagation direction, reproduced from [85]

In both of these scenarios, the wavelength or point at which $\beta_A = \beta_B$ is where the power in both the even supermode and the odd supermode is evenly distributed between the two waveguides. This is illustrated by the even and odd field profiles (e_e and e_o) shown at the bottom of Figure 5-3.

Another important distinction between the even and odd modes lies in the number of zero crossings the field has. Just like the modes in a typical single-piece waveguide, the field for the even mode (fundamental mode of the combined structure) does not have a zero crossing. The odd mode (the first harmonic, or the second order mode for the combined structure) has one zero crossing. If the individual waveguides supported more than one mode, all Cartesian product combinations of these modes would show up as supermodes. For instance, if one of the waveguides supported 2 guided modes instead of 1, there would be a total of 4 supermodes including even and odd combinations of each pair. Similarly, the number of zero crossings would indicate the order of propagation constants. However, from a design perspective, one should aim to reduce the number of guided modes to the minimum required. In other words, the designed structure should only support modes that are necessary for device operation.

In Figure 5-4, we plot equations (5.31) and (5.32) to investigate the power remaining in one of the waveguides as a function of γ for the even supermode. Since $|\kappa|$ is always positive, the signs of γ and δ are the same. As predicted for the even mode, the waveguide with the larger propagation constant carrier more power. The transmission for the same waveguide in case of the odd mode is exactly opposite, as predicted by equation (5.32), and as also was shown by power conservation in equation (5.34). The power distribution in Figure 5-4 will be studied in more detail in the context of a spectral filter in Section 5.3.1.

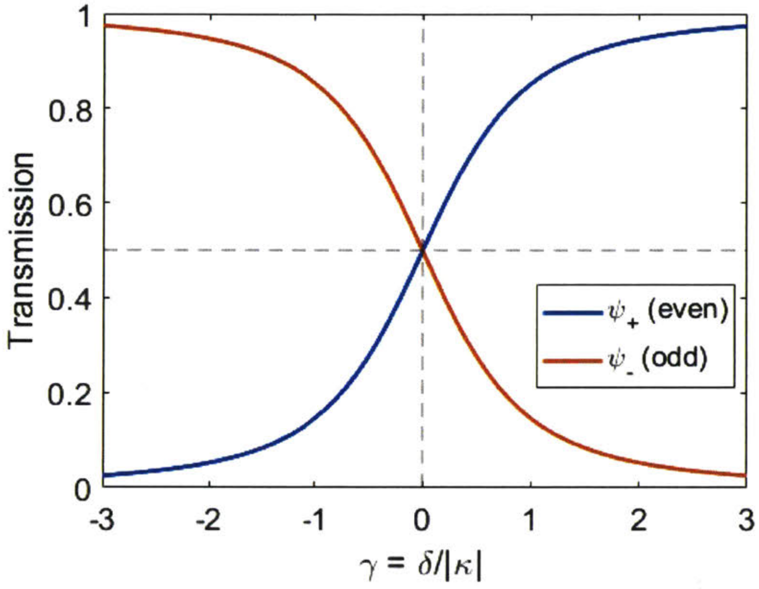

Figure 5-4: Transmission for one of a pair of coupled waveguides as a function of γ for the even and odd supermodes

5.2 Spectral Dependence of a Directional Coupler

Propagation of modes in a directional coupler such as one shown in Figure 5-1 is governed by equations (5.4) and (5.5). The solutions to these equations are given by

$$\begin{bmatrix} a_A \\ a_B \end{bmatrix} = \begin{bmatrix} \cos(Sz) + j\frac{\delta}{S}\sin(Sz) & -\frac{j\kappa}{S}\sin(Sz) \\ -\frac{j\kappa}{S}\sin(Sz) & \cos(Sz) + j\frac{\delta}{S}\sin(Sz) \end{bmatrix} \begin{bmatrix} a_A(0) \\ a_B(0) \end{bmatrix} e^{-j\bar{\beta}z} \tag{5.35}$$

where a_A and a_B represent propagation direction dependent field amplitudes whose initial values are given by $a_A(0)$ and $a_B(0)$ in WG$_A$ and WG$_B$ respectively [83]. If all the power is input to WG$_A$, then we can reduce equation (5.35) by setting $a_A(0) = 1$ and $a_B(0) = 0$. This yields

$$
\begin{aligned}
a_A &= \left(\cos(Sz) + j\frac{\delta}{S}\sin(Sz)\right) a_A(0)e^{-j\bar{\beta}z} \\
a_B &= -\frac{j\kappa}{S}\sin(Sz)\, a_A(0)e^{-j\bar{\beta}z}
\end{aligned}
\tag{5.36}
$$

This indicates that the maximum power coupled from one waveguide to the other is $(\kappa/S)^2$. Furthermore, when the two waveguides WG$_A$ and WG$_B$ are identical, the propagation constants are the same, and we have $\delta = 0$ and $S = \kappa$. Consequently,

$$
\begin{aligned}
a_A &= \cos(Sz)\, a_A(0)e^{-j\bar{\beta}z} \\
a_B &= -j\sin(Sz)\, a_A(0)e^{-j\bar{\beta}z}
\end{aligned}
\tag{5.37}
$$

The oscillation of power between two identical waveguides comes from this sinusoidal form of a_A and a_B. The power in WG$_A$ is then proportional to $|a_A|^2 \propto \cos^2(Sz)$; and similarly, the power in WG$_B$ is then proportional to $|a_B|^2 \propto \sin^2(Sz)$.

What is less commonly studied is the spectral dependence of this behavior. Let's assume that one designs a symmetric directional coupler of length L that achieves 100% coupling to an adjacent waveguide at wavelength λ_0. Then, we know that

$$
\sin^2(SL) = 1 \Longrightarrow SL = \frac{\pi}{2} \Longrightarrow L = \frac{\pi}{\beta_+ - \beta_-} = \frac{\lambda_0}{2(n_+ - n_-)}
\tag{5.38}
$$

However, the ratio of coupled power changes at wavelengths other than λ_0. At shorter wavelengths, since the modes are not as strongly coupled, longer interaction lengths are needed for full coupling. Conversely, for longer wavelengths, L is already longer than the required interaction length due to increased coupling strength. We can investigate this behavior by solving for the individual and supermode effective indices as a function of wavelength for a symmetric directional coupler with 320 nm wide waveguides separated by a gap of 300 nm. Using the indices, the coupling coefficient is calculated at each wavelength from equation (5.21). Then, the power transferred to the adjacent waveguide is plotted in Figure 5-5 according to equation (5.37).

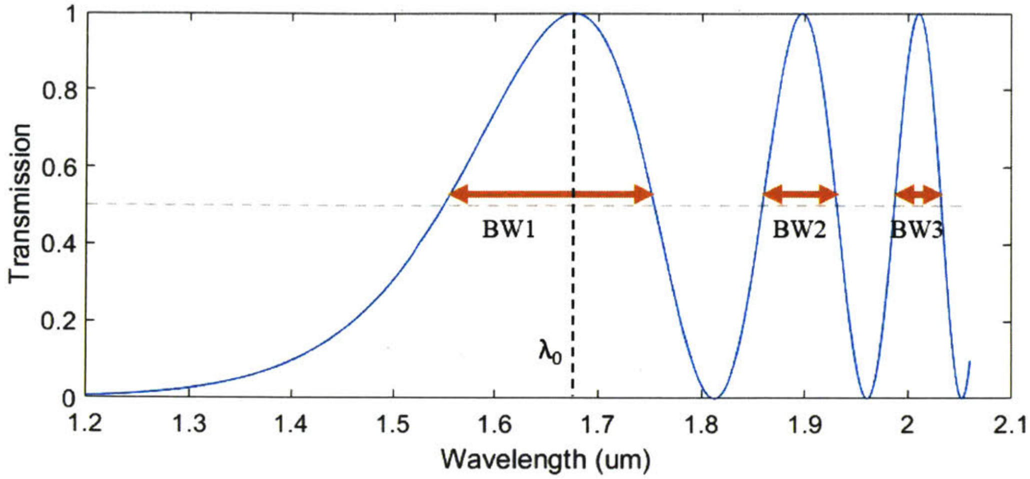

Figure 5-5: Spectral dependence of an example symmetric directional coupler

The transmitted power as a function of wavelength takes the form of a chirped wave, with a $\sin^2(a\lambda^b L)$ dependence. This is an empirically obtained dependence from the effective index difference of the even and odd modes (see Appendix 2). As predicted, for wavelengths significantly shorter than λ_0, there is minimal power transfer. The first wavelength at which 100 % transfer occurs is in fact λ_0. This is also the spectral solution that achieves the 100 % power transfer with the widest bandwidth (BW1). Subsequent wavelengths of 100 % power transfer have consecutively narrower bandwidths due to light going back and forth between the two waveguides multiple times (BW3 < BW2 < BW1). Therefore, for robust operation one should always aim to design such a device to operate around the first 100 % power transfer wavelength. Since fabrication-induced width and height variations introduce effective index changes, $\beta_+ - \beta_-$ usually experiences slight changes, and the center wavelength λ_0 is shifted. Having a large BW1 also ensures proper device operation even when λ_0 is slightly shifted from the design target. That way, the device can be used as a spectral filter or a wavelength splitter/combiner for signals at $\lambda_1 \approx \lambda_0$ and $\lambda_2 \ll \lambda_0$. For this operation regime, the extinction ratio depends on how close λ_2 is to λ_0. At $\lambda_0 - \lambda_2 = (BW1)/2$, we get 3 dB extinction by definition. From the plot in Figure 5-5, the estimated extinction goes up to approximately 8 dB for $\lambda_0 - \lambda_2 = (BW1)$, and to 13 dB for $\lambda_0 - \lambda_2 = 3(BW1)/2$.

5.3 Filters Based on Spectrally Selective Waveguides

Optical filters are one of the most important and widely used building blocks in photonic systems. Many applications including communications [86, 87], spectroscopy [88-91], imaging and microscopy [92, 93], optical signal processing [94, 95], and radio frequency and optical synthesis and stabilization [96-98] take advantage of various types of integrated or free-space optical filters to selectively separate or combine incident light at different wavelengths. Among the most common types of optical filters used in free-space systems are dichroic lenses or reflectors where incident light is selectively reflected or transmitted due to interference within the alternating layers of optical coatings. Although dichroic filters can achieve relatively wideband operation up to hundreds of nm, they are limited in scalability and are not suitable for optical systems requiring tens or hundreds of optical filters at precise wavelengths. Moreover, many commercial free-space dichroic filters also have slow roll-offs where the transmission drops from a maximum of 95-99 % to below 5 % in approximately 100 nm [99], corresponding to 0.2-0.3 dB/nm roll-off.

For in-band filtering where the operation is restricted to a certain spectral region like the O-band (1260 - 1360 nm) or the C-band (1530 - 1565 nm), many examples of collections of tunable microring resonators [100, 101], arrayed waveguide gratings (AWG) [102, 103], and photonic crystal filters [104, 105] have been demonstrated. However, the limited operation bandwidth presents challenges in dense wavelength division multiplexing applications where many channels have to be squeezed into a narrow spectrum. Due to their interferometric operation principles, resonators and AWGs do not exhibit single cutoff behavior, and are limited by their free spectral ranges. Resulting narrow bandwidths cause increased crosstalk in adjacent channels [106]. Moreover, achieving flat-top pass-band responses in resonant, interference-based, or other narrowband filters results in higher insertion losses [107, 108].

While sharp spectral transitions are commonly found in interferometric devices like ring resonators, AWGs, or Fabry-Perot cavities, broadband responses are typically only achieved by adiabatic structures. As a result of their broadband response, adiabatically-coupled structures generally do not exhibit transmissions with sharp spectral changes. An ideal integrated filter must achieve a broad and low-loss pass-band, similar to adiabatic structures, but must also have a sharp filter roll-off at the desired cutoff wavelength. In the past, wavelength dependence of evanescent field overlap has been used as another means to spectrally separate and combine light in adiabatic couplers [109, 110]. However, in such a coupling scheme, the coupling coefficient κ is primarily influenced by waveguide dispersion, and therefore has a weak wavelength dependence. As a result, slow pass-band to reject-band transitions are obtained (estimated 0.02 dB/nm in [109], and 0.03 dB/nm in [110]). Moreover, in the reported devices, a longer coupler yields a shorter cutoff wavelength, due to the increased κL product. Therefore the cutoff wavelength depends on the coupler length, and can only be determined after accurate propagation simulations.

In this section, I present the theory, design approach, and experimental results for broadband, low-loss, integrated dichroic filters that can achieve single-cutoff operation while maintaining a sharp filter roll-off. First I investigate possible waveguide cross-sections for spatial separation of guided modes, and model the transition roll-off using a coupled mode description. I show that a sharp filter roll-off is expected when the individual propagation constants of two adjacent waveguides are matched at a single wavelength and are highly mismatched otherwise. This allows the cutoff wavelength to remain as a separate design parameter independent of the propagation length along the coupler. I then design the transitions to the desired cross-sections, fabricate the devices in a standard CMOS foundry, and experimentally verify the short-pass and the long-pass filter characteristics. The results suggest that single-cutoff broadband filters created with the methods described here can be adapted in other integrated photonic platforms to create other types of highly customizable optical functions such as band-pass or all-pass filters as well as ultra-broadband multiplexers, pump couplers, and arbitrary optical waveform generators.

5.3.1 Waveguide Geometries for Dichroic Response

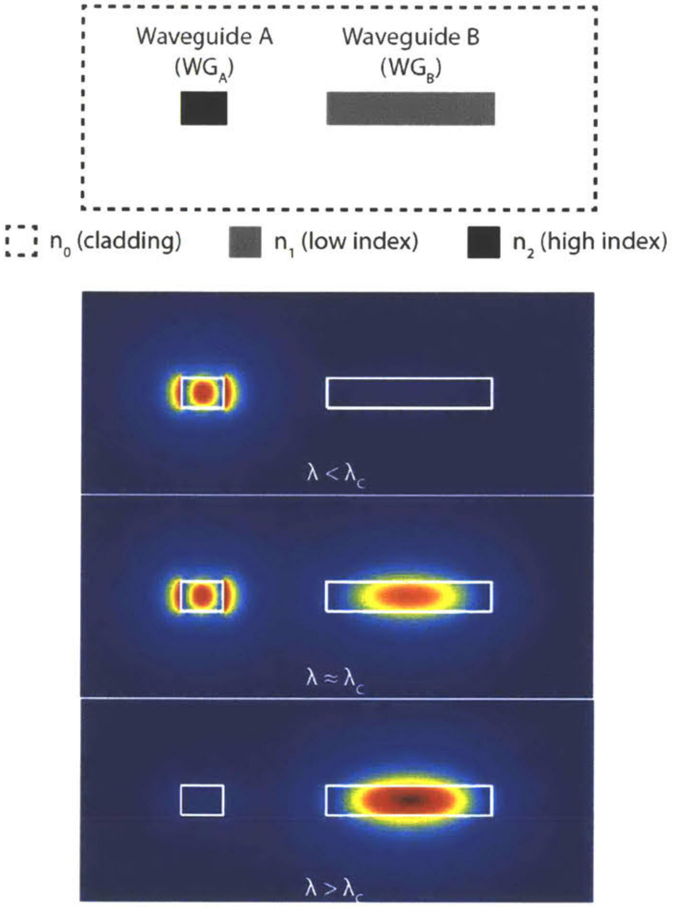

Figure 5-6: Spectrally selective waveguide cross-section made from 2 different core materials. Fundamental TE modes below, at, and over the cutoff wavelength.

In order to design geometries that can achieve the desired dichroic splitting, we first need to interpret the power distribution in a coupled waveguide geometry plotted previously in Figure 5-4. Equation (5.31) describes the distribution of power between any two coupled waveguides in general. Here, δ and κ are determined by waveguide geometry, which can be engineered to yield the desired transfer function according to the above derived transmission response. Specifically, for spectral filtering and combining applications, we can exploit the wavelength dependence of γ. For instance, at the wavelength where $\gamma = 0$, power is evenly distributed between WG$_{\mathrm{A}}$ and WG$_{\mathrm{B}}$. This marks the 3 dB cutoff of the filter, and occurs only when WG$_{\mathrm{A}}$ and WG$_{\mathrm{B}}$ are phase matched ($\delta = 0$). The sign of γ at all other wavelengths is determined by the magnitudes of β_A and β_B. For $\beta_A > \beta_B$, $\delta > 0$, $\gamma > 0$, and $|T_A| > 1/2$. As the difference $\beta_A - \beta_B$ grows, δ becomes increasingly positive, $|T_A|$ approaches 1, and majority of the optical power in ψ_+ is confined within $\mathrm{WG_A}$. Similarly, for increasingly negative values of δ, $|T_A|$ approaches 0, and the optical power in ψ_+ is primarily confined in $\mathrm{WG_B}$. In summary, a wavelength-dependent sign change in δ manifests itself in ψ_+'s spatial profile change from $\mathrm{WG_A}$ to $\mathrm{WG_B}$. As a result, the two coupled waveguides act as transmissive spectral filters whose outputs are determined by their dispersion characteristics.

The key to achieving a dichroic filter response with separate short-pass and long-pass ports is to use two waveguides that are only phase matched at the filter cutoff wavelength (λ_C). The mismatch of propagation constants at wavelengths other than λ_C is essential for a good extinction ratio between the two output ports, and can be accomplished by waveguides with different group indices. An example of such a waveguide cross-section is given in Figure 5-6. Here, $\mathrm{WG_A}$ is made from a higher index material than $\mathrm{WG_B}$, and is therefore to be narrower to satisfy the phase matching condition at the desired λ_C.

Figure 5-7 depicts an alternative waveguide cross-section, where $\mathrm{WG_B}$ consists of closely-spaced multiple waveguide segments made from the same material as $\mathrm{WG_A}$. Here, $\mathrm{WG_B}$ effectively possesses spectral characteristics equivalent to a waveguide with smaller group index, or one made from a smaller refractive index material. This is a commonly used idea in photonic crystal structures where effective index is modulated by the gap sizes between higher-index waveguide segments. The practical advantage of the multi-segmented $\mathrm{WG_B}$ is due to its simpler fabrication procedure, as it doesn't require any additional materials or lithography stages after $\mathrm{WG_A}$ has been fabricated. In both cases, the group index difference is instrumental for realizing the phase mismatch at wavelengths outside of the cutoff, and therefore is key for a spectrally selective cross-section.

Both examples consist of two waveguides, whose guided modes are coupled via their evanescent fields. Both cross-sections are accompanied by plots of major electric field components of their transverse-electric (TE) quasi-even supermodes at $\lambda < \lambda_C$, $\lambda \approx \lambda_C$, and $\lambda > \lambda_C$ shown in Figure 5-6 and Figure 5-7. Here, we simulated the mode profiles and the propagation constants by using a finite difference eigenmode solver. Effective indices and guided modes in all waveguide cross-sections were simulated using Lumerical's MODE software with a maximum discretization of 10 nm. Inside and around the waveguide cores, a 5 nm discretization was used. At λ_C, as γ changes sign, the field distribution evolves from one waveguide to another as predicted by the theoretical analysis. Since equation (5.31) describes power distribution in a coupled waveguide geometry in general, any two waveguides satisfying $\delta = 0$ at one wavelength can be used to spectrally filter an optical input.

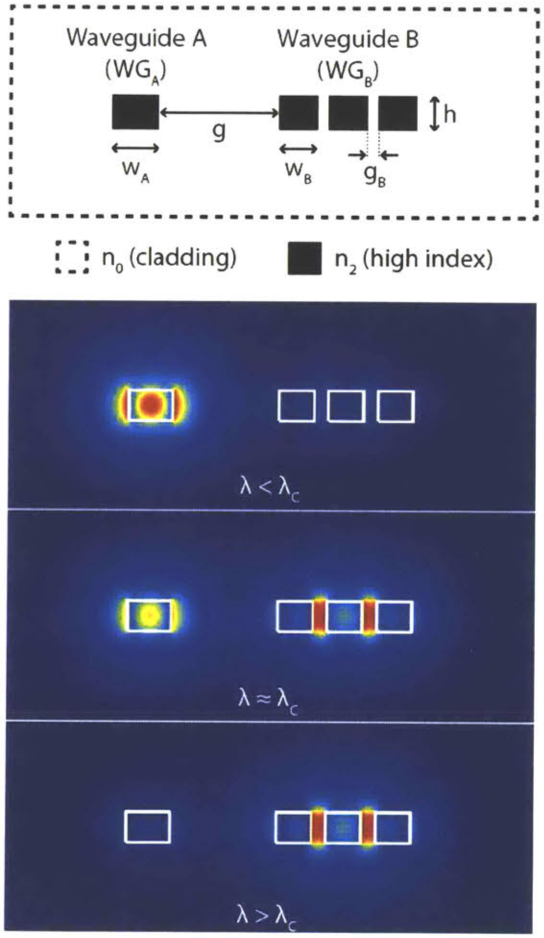

Figure 5-7: Spectrally selective waveguide cross-section made from a single core material, in one lithography step. Fundamental TE modes below, at, and over the cutoff wavelength

Although both cross-sections have been designed with a silicon-on-insulator (SOI) platform in mind, the design in Figure 5-7 is more advantageous from a fabrication perspective due to its single-material and single-step lithography process. For the rest of the analysis, we therefore focus only on the cross-section in Figure 5-7. In Figure 5-8, we plot the corresponding effective indices of the individual fundamental TE modes of WG_A and WG_B for the geometry in Figure 5-7. Here, by varying the width of WG_A (w_A), we designed a number of waveguide cross-sections for filter cutoffs in the 1550 nm communication band, as indicated by the shifting intersection wavelength between the plotted effective indices. For this particular design, the evolution of the field distribution from WG_A to WG_B is also observed in the supermode effective indices plotted in Figure 5-9. Just as in the mode profiles, the quasi-even supermode ψ_+ evolves from ψ_A to ψ_B with increasing wavelength, and follows the highest effective index available in the cross-section.

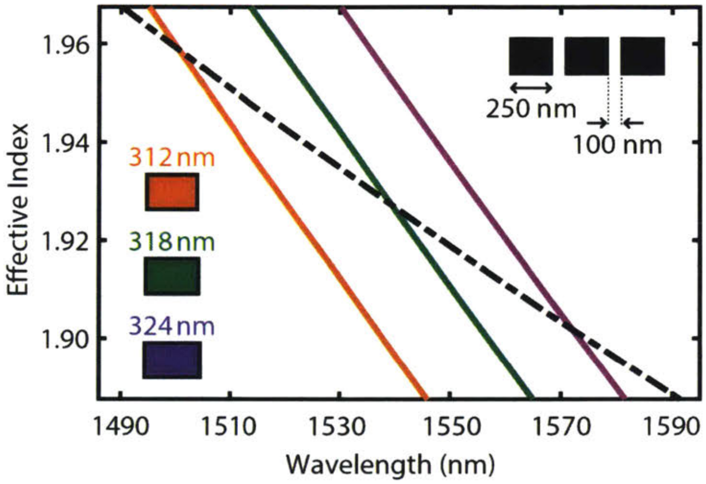

Figure 5-8: Effective indices of the individual waveguides in the spectrally selective waveguide cross-section. Width of WG_A is varied.

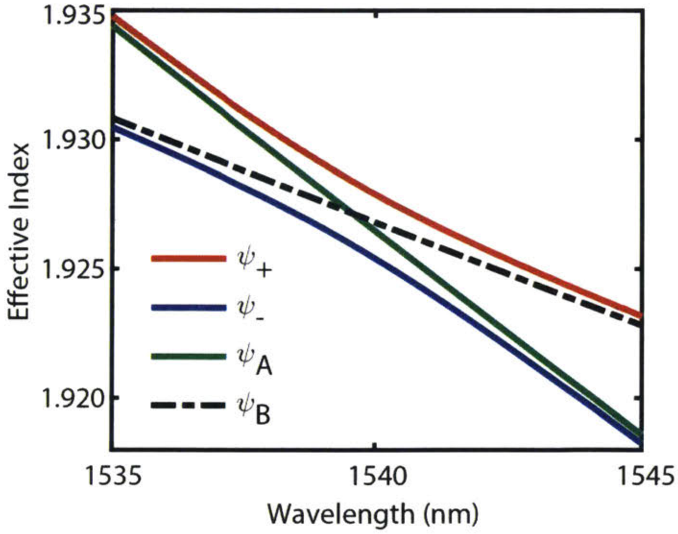

Figure 5-9: Effective indices for the quasi-even and quasi-odd supermodes in the spectrally selective waveguide cross-section

In principle, one can design WG_B with any number of segments to yield a similar effective index profile as shown in Figure 5-8. However, the optimum solution consists of a bulk-like (or ideally flat) effective index profile that can maximize the magnitude of δ when $\lambda \neq \lambda_C$. An increasing number of segments can be used to mimic a bulk-like material, as the combination of closely spaced, small high-index segments acts a single waveguide with a lower effective index. In reality, design choices are generally limited by the minimum widths and gaps that can be reliably fabricated. Here, we used a three-segment design to achieve a large difference between β_A and β_B while ensuring reliable fabrication of the thin waveguide segments.

5.3.2 Power Roll-Off Around the Cutoff Wavelength

How fast the power in the quasi-even mode evolves from WG_A to WG_B depends on γ's rate of change with respect to wavelength. As $\gamma = \delta/|\kappa|$, γ's wavelength dependence is determined by the change in the effective indices and the coupling coefficient as a function of wavelength. In Figure 5-10, we plot $\delta(\lambda)$, and $|\kappa(\lambda)|$ for the waveguide cross-section in Figure 5-7, with a gap of g = 750 nm between $\mathrm{WG_A}$ and $\mathrm{WG_B}$. $\delta(\lambda)$, by definition, is half of the propagation constant difference between β_A and β_B.

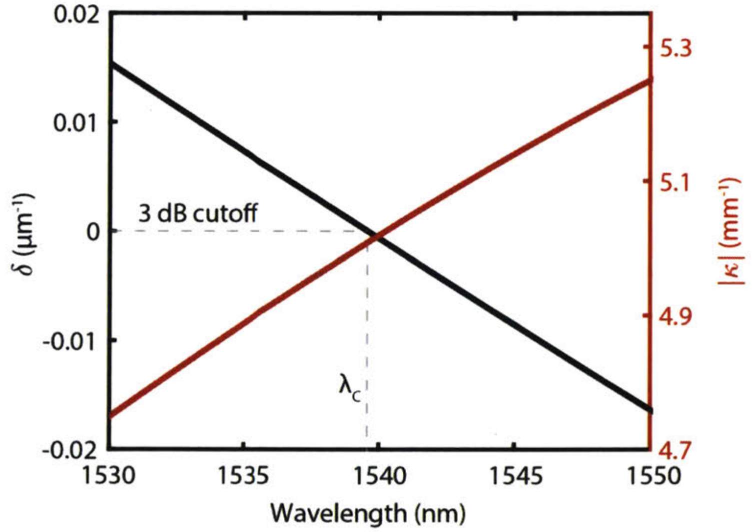

Figure 5-10: Propagation constant difference (δ) and the coupling coefficient (κ) as a function of wavelength around λ_C

Around λ_C, the sign of $\delta(\lambda)$ is wavelength-dependent, and therefore, δ undergoes significant change with changing wavelength. For this specific design, $\delta(\lambda < \lambda_C) > 0$, $\delta(\lambda = \lambda_C) = 0$, and $\delta(\lambda > \lambda_C) < 0$. On the other hand, the coupling coefficient $|\kappa(\lambda)|$ is only a slowly varying function of λ, as it mainly depends on the overlap of the evanescent fields of individual modes

ψ_A and ψ_B. The wavelength dependent change in the overlap is primarily influenced by waveguide dispersion, as the larger spatial profiles of ψ_A and ψ_B at longer wavelengths result in greater coupling coefficients. The weak wavelength dependence of $|\kappa(\lambda)|$ shown here also explains the slow roll-off speeds of filters relying purely on waveguide dispersion. This can also be confirmed by solving for the coupling coefficient from the eigenvalues as in equation (5.21). Since $|\kappa(\lambda)|$ is monotonically increasing and slowly varying, $\gamma(\lambda)$ and $\delta(\lambda)$ exhibit similar spectral dependence. By the description in (5.31), the sign change in $\gamma(\lambda)$ results in a maximum-to-minimum transition in $|T_A|$, where $\gamma(\lambda = \lambda_C) = 0$ marks the 3 dB filter cutoff.

In Figure 5-11, we plot the expected transmission response $|T_A|$ for the cross-section in Figure 5-7. The power roll-off is characterized numerically by evaluating the ratios of Poynting vector flux through regions surrounding WG_A and WG_B to the total flux through the whole cross-section. This provides a measure of the ratio of optical power in one waveguide to the total guided power at discrete wavelengths. The simulated result (circles) is plotted together with the analytical result (dashed line) from the coupled mode solution in equation (5.31). With increasing wavelength, majority of the optical power shifts from WG_A to WG_B, tracing the change observed in the mode profile of ψ_+ from Figure 5-7. The analytical and simulated results show excellent agreement.

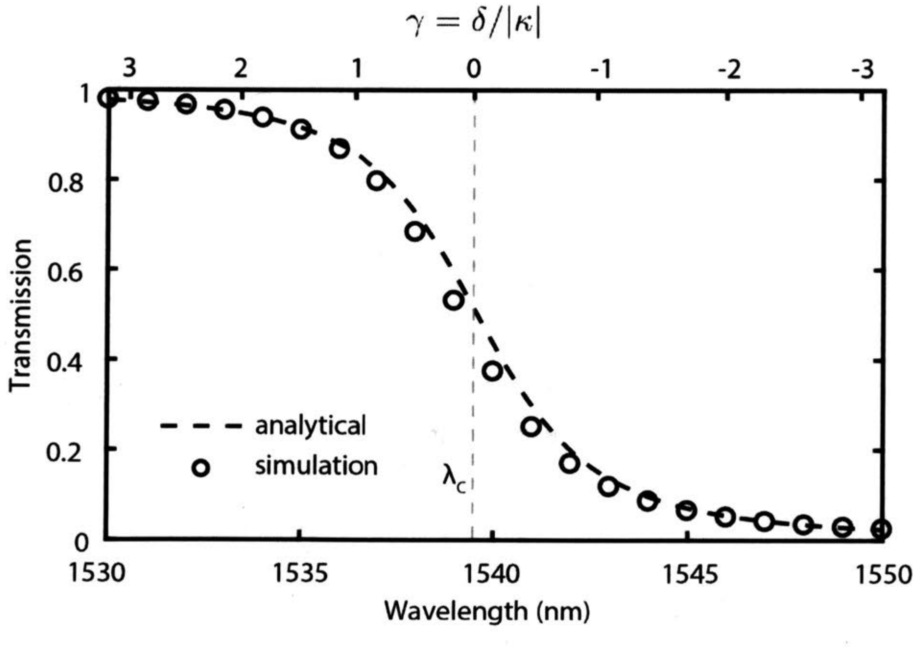

Figure 5-11: Transmission for WG_A with the quasi-even mode input as a function of wavelength. γ is plotted in the secondary horizontal axis and decreases with increasing wavelength

The speed at which $|T_A|$ approaches 1 or 0 on either side of the cutoff depends on how fast the magnitude of γ can grow with changing wavelength. As $|\kappa(\lambda)|$ is only slowly varying, $\gamma(\lambda)$'s magnitude is mainly influenced by $\delta(\lambda)$. By definition, the larger the difference in effective indices of ψ_A and ψ_B, the larger the magnitude of $\delta(\lambda)$. Therefore, in order to approach 1 or 0 transmission on the left or right of the cutoff, one must design WG$_A$ and WG$_B$ to achieve maximum effective index difference when $\lambda \neq \lambda_C$. Since the propagation constants β_A and β_B must match at $\lambda = \lambda_C$, the effective index difference for $\lambda \neq \lambda_C$ is only possible with waveguides with different group indices. With a larger group index difference, although a faster transition from 1 to 0 is expected, phase matching at the desired λ_C becomes increasingly challenging. One can also increase the magnitude of γ by separating WG$_A$ and WG$_B$ with a larger gap, which in turn reduces κ for all wavelengths. However, in order to efficiently guide light in structures with multiple segments, slowly varying transitions to the desired cross-sections are required. As longer transitions are needed to implement larger gaps, the separation of WG$_A$ and WG$_B$ presents a design trade-off between device length and performance.

5.3.3 Adiabatic Coupler Design

Once the appropriate waveguide geometry is determined for the desired spectral response, efficient transitions from a single core rectangular waveguide to the determined cross-section must be designed. For low insertion-loss and wideband device response, a single-mode TE input at any given wavelength must stay in the quasi-even mode throughout these transitions. According to coupled local-mode theory, power lost to unwanted modes can be minimized by decreasing the rate of change of the dielectric constant along the propagation length [111], or equivalently by using longer transitions [112]. To this end, we designed the slowly varying waveguide transitions illustrated in Figure 5-12 for evolution of the quasi-even mode electric field as light propagates through the device. In this schematic illustration of short-pass and long-pass ports of the integrated dichroic filter, there are four transition sections to reach the desired waveguide cross-section. The Si substrate as well as the buried and top oxides are not shown. The spectrally selective cross-section is reached just before section ④, where wavelengths are separated to short-pass and long-pass ports.

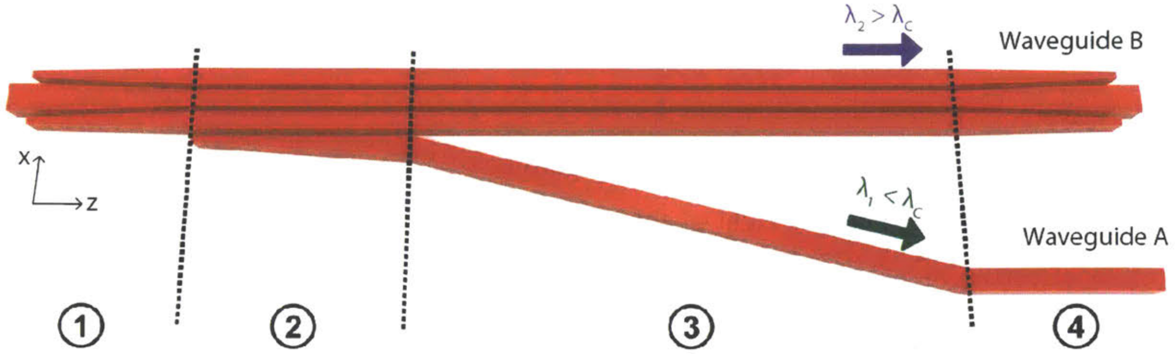

Figure 5-12: Design of the mode-evolution transition structures from a single-core waveguide to the desired wavelength selective cross-section

Throughout the transitions indicated from ① through ④, a single waveguide input is converted to a 3-segment waveguide, a new adjacent waveguide segment (WG_A) is developed next to the 3 segments, the newly developed segment is slowly separated, and the 3-segments are converted back into a single rectangular waveguide respectively. In all transitions, a 100 nm minimum waveguide spacing and width were used, as dictated by the limitations in our SOI fabrication process. We simulated the transmission of the quasi-even mode through each section using the eigenmode expansion method (EME) as plotted in Figure 5-13, Figure 5-14, and Figure 5-15.

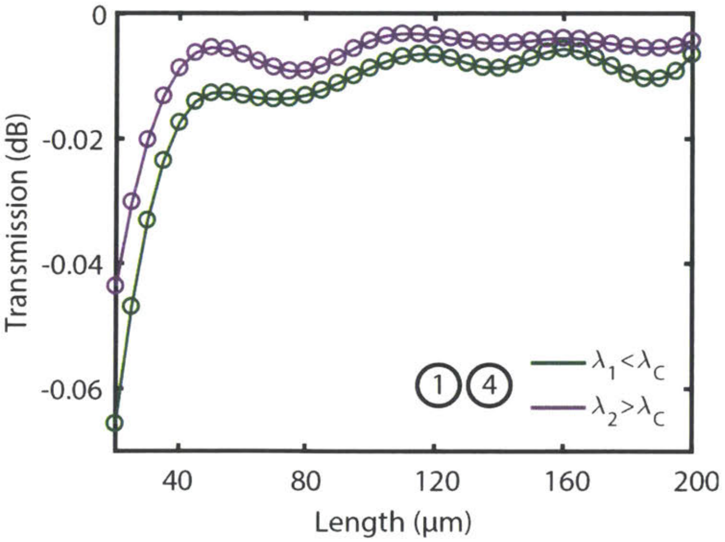

Figure 5-13: Eigenmode expansion simulation for sections ① and ④

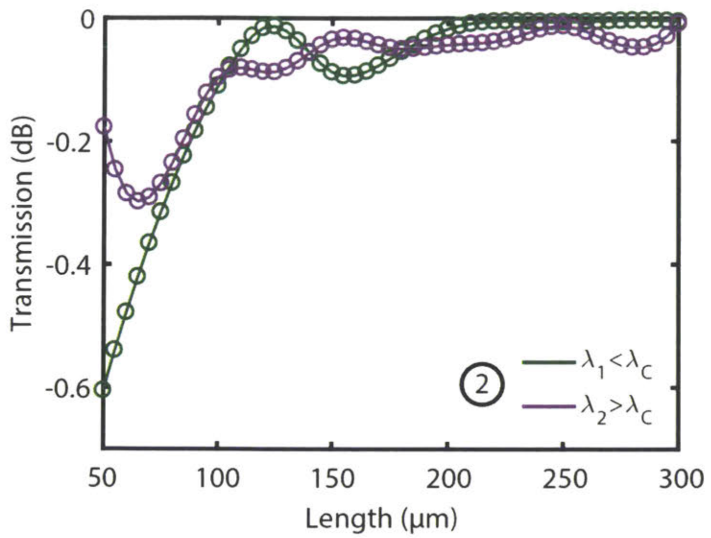

Figure 5-14: Eigenmode expansion simulation for section ②

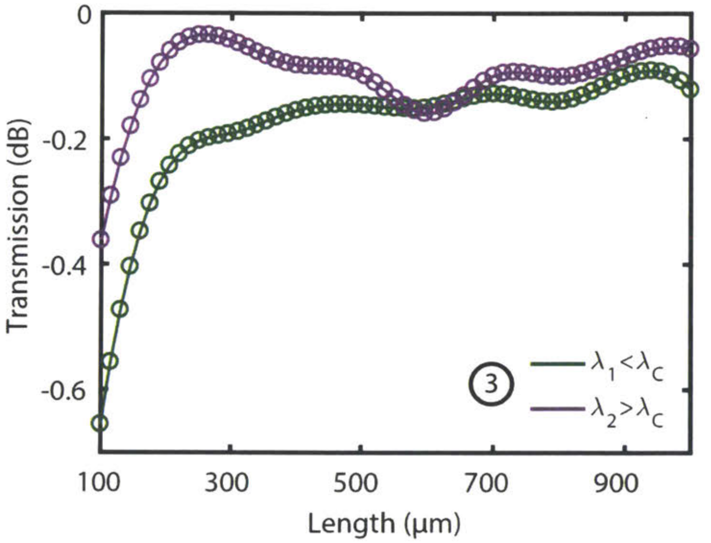

Figure 5-15: Eigenmode expansion simulation for section ③

Transmission efficiencies plotted here were extracted from the power transferred between the quasi-even input and quasi-even output modes as simulated by the EME method. In the direction of propagation, a total of 30 modes were solved every 5 µm in regions ① and ②, and every 15 µm in region ③. From the EME results, we determined the required transition lengths to achieve maximum transmission in each section. We chose $L_1 = L_4 = 200$ µm, $L_2 = 260$ µm, and $L_3 = 900$ µm to minimize insertion loss while avoiding excessively long transitions to reduce losses due to propagation. At the end of section ③, WG_A and WG_B have been separated to a final gap of g = 2 μm, in order to minimize any further coupling between the two waveguides, and allow convenient connections to downstream devices for use in larger systems. Section ① and the top part of section ④ (for WG_B) are the same transitions in reverse, therefore have the same spectral response, and were chosen to have the same length due to reciprocity.

5.3.4 Device Fabrication

All filters were fabricated using 300 mm SOI substrates with 225 nm-thick Si layer, and a 2 μm-thick buried oxide in a CMOS foundry with 65 nm technology node. SOI was patterned using 193 nm immersion photolithography and reactive ion etching. Si layer was etched completely to form the strip waveguides. This was followed by an oxidization step to passivate the sidewalls, which reduced the Si thickness to 220 nm. A 4 μm-thick top cladding of SiO_2 was chemical vapor deposited. Dicing trenches were etched on the die borders, and the wafer was diced to individual dies. An SEM image from one of the fabricated devices is shown in Figure 5-16 where WG_A and the multi-segment WG_B are clearly resolved.

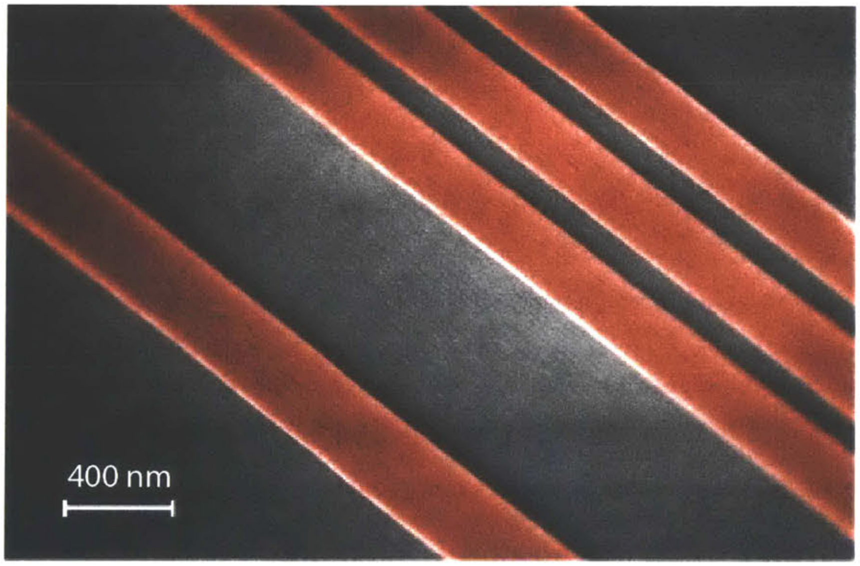

Figure 5-16: A colorized scanning electron micrograph of one of the fabricated dichroic filters.

5.3.5 Characterization and Analysis of Filter Response

For use in infrared applications, filters with cutoff wavelengths around 1550 nm and 2100 nm were fabricated. To test the fabricated filters, we used single-mode fibers, polarization controllers, and inverted facet tapers for on and off chip coupling of tunable continuous-wave laser sources. Specifically, filters were characterized using three continuous wave laser sources tunable from 1484 – 1625 nm, 1860 – 2010 nm, and 2040 – 2400 nm. Single-mode fibers SMF-28 and SM-2000 were used together with polarization controllers to couple TE light on- and off-chip through inverted facet tapers.

Figure 5-17 and Figure 5-18 show the measured spectral responses of the filters where the expected cutoff wavelengths were $\lambda_C = 1539.6$ nm and $\lambda_C = 2128.6$ nm respectively, from the mode solutions results. The measured responses from both the short-pass and the long-pass ports confirm the single cutoff characteristic of the filter. The cutoff wavelengths were measured to be 1533.3 nm and 2119.9 nm from Figure 5-17 and Figure 5-18 respectively. The mismatch between the measurement and the design targets can be attributed to thickness and width variations due to fabrication. The insertion losses through the filters in the pass-bands were measured to be approximately 1 dB for the short-pass ports, and less than 2 dB for the long-pass ports. Increased loss at the long-pass port can be explained by the increased interaction of the propagating mode with the sidewalls, due to the design of WG_B. This sidewall interaction also explains the slightly reduced extinction ratio in the long-pass output, due to scattering of light to adjacent WG_A. Extinction ratios of approximately 10 dB are measured for the short-pass and long-pass ports in Figure 5-17. For the longer wavelength filter in Figure 5-18, the measured extinction ratios were over 15 dB and 17 dB for the short-pass and long-pass ports respectively. Power roll-off for the filters were calculated to be as high as 2.82 dB/nm and 0.85 dB/nm by differentiating the transmission responses in Figure 5-17 and Figure 5-18 respectively. Due to the slowly varying transitions of waveguide cross-sections, the propagating mode in the dichroic filters demonstrated here does not rely on evanescent coupling to adjacent waveguides. As a result, the measured roll-offs here are 10-70 times sharper than free-space dichroic lenses [99] or integrated filters making use of evanescently coupled devices [109, 110].

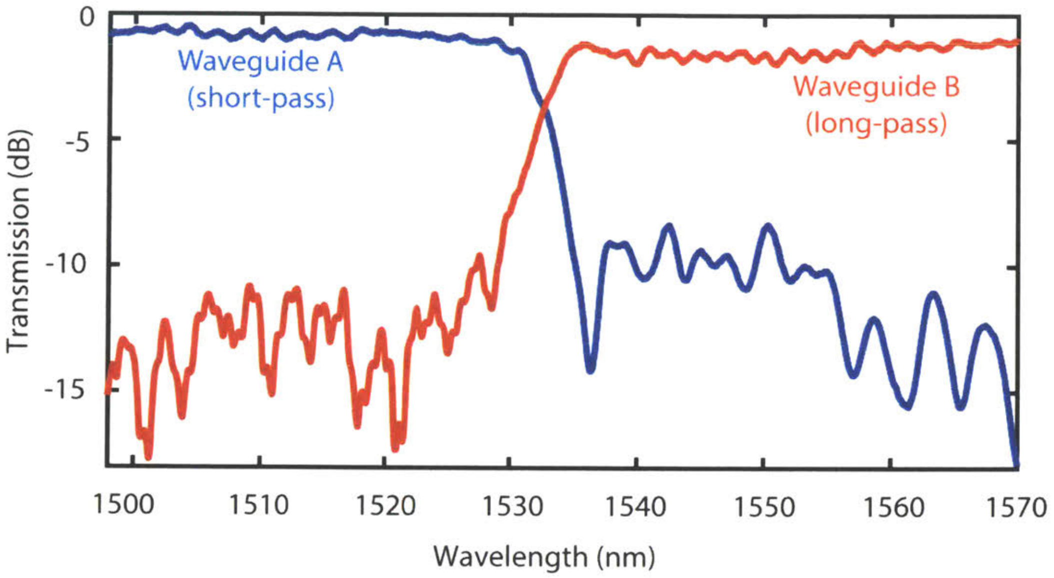

Figure 5-17: Transmission spectra for WGA (short-pass) and WGB (long-pass) with C-band cutoff

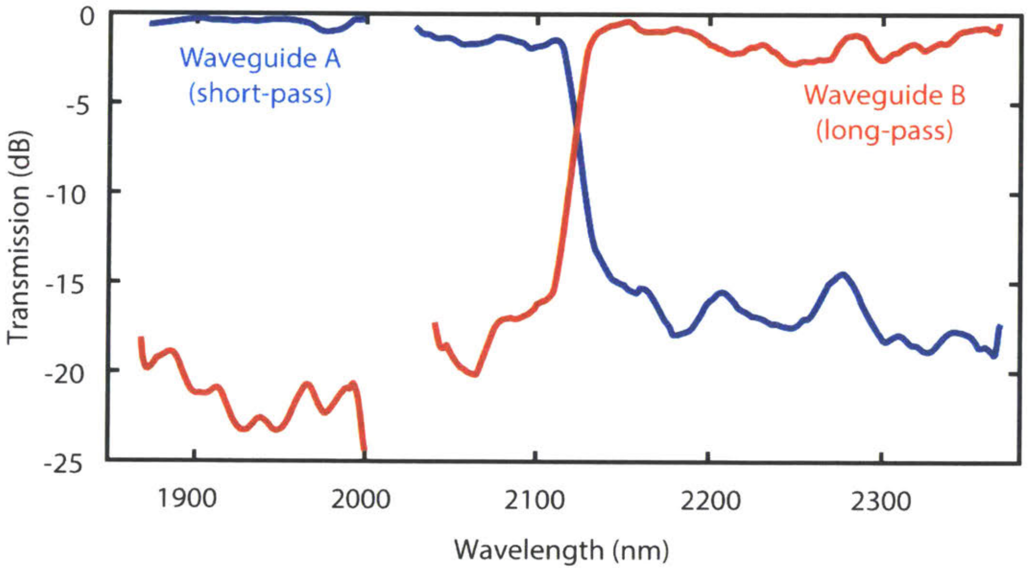

Figure 5-18: Transmission spectra for WGA (short-pass) and WGB (long-pass) with cutoff around 2.1 μm

The dichroic filter with the C-band cutoff wavelength was then imaged with an infrared camera at two wavelengths $\lambda_1 = 1530\text{ nm} < \lambda_C$ and $\lambda_2 = 1535\text{ nm} > \lambda_C$. 20 images were captured along the length of the device and stitched together creating one overall image for each wavelength. The two images were then colored accordingly and overlaid on top of one another to illustrate the device operation. The resulting image is shown in Figure 5-19 where the two wavelengths is clearly resolved and directed to the corresponding output ports of the dichroic filter.

Figure 5-19: Colored and overlaid infrared images of the dichroic filter operation. Blue: $\lambda_1 = 1530\text{ nm} < \lambda_C$, Red: $\lambda_2 = 1535\text{ nm} > \lambda_C$

Any change in the waveguide geometry due to fabrication presents itself as a shift to the effective indices plotted in Figure 5-8. With shifted propagation constants, as $\delta(\lambda)$ is modified, the cutoff wavelength at which $\gamma = 0$ is also shifted. This induced shift not only explains the difference between the expected and measured cutoffs, but also can be utilized to design and fabricate filters with different cutoffs. For instance, to shift the response to longer wavelengths, one can either increase w_A, or increase g_B, resulting in a either higher effective index for WG_A, or a lower effective index for WG_B. Under both conditions, the intersection for the effective indices of ψ_A and ψ_B, and therefore the cutoff wavelength, is shifted to longer wavelengths. The new expected cutoff wavelengths can be calculated by mode solutions with the new waveguide dimensions. For instance, using $w_A = 312$ nm while keeping all other dimensions the same as in Fig. 1e, the cutoff wavelength is simulated to be $\lambda_C = 1500.7$ nm, and measured from the transmission in Figure 5-20 as 1495.1 nm. Similarly for $w_A = 324$ nm, the simulated and measured cutoffs are 1572.2 nm and 1573.9 nm respectively.

For longer wavelength applications, we designed another set of three filters to have cutoffs in the 2.1–2.2 μm range. In addition to the nominal design choice of $w_A = 494$ nm, filters with with $w_A = 486$ nm and 502 nm were fabricated while the dimensions of $w_B = 350$ nm and $g_B = 100$ nm were maintained for WG_B. For this set of filters with longer cutoff wavelengths, the transmission measurements are plotted in Figure 5-21. Using the transmission data, the cutoff wavelengths are measured to be 2076.3 nm, 2119.9 nm, and 2162.4 nm in the order of increasing w_A. The expected cutoffs are 2078.5 nm, 2128.6 nm, and 2169.6 nm, as determined by eigenmode simulations. Similar to the devices with cutoffs in the 1550 nm window, the difference between the simulated and measured cutoffs can be attributed to fabrication induced changes in the Si layer height as well as the dimensions of individual waveguides.

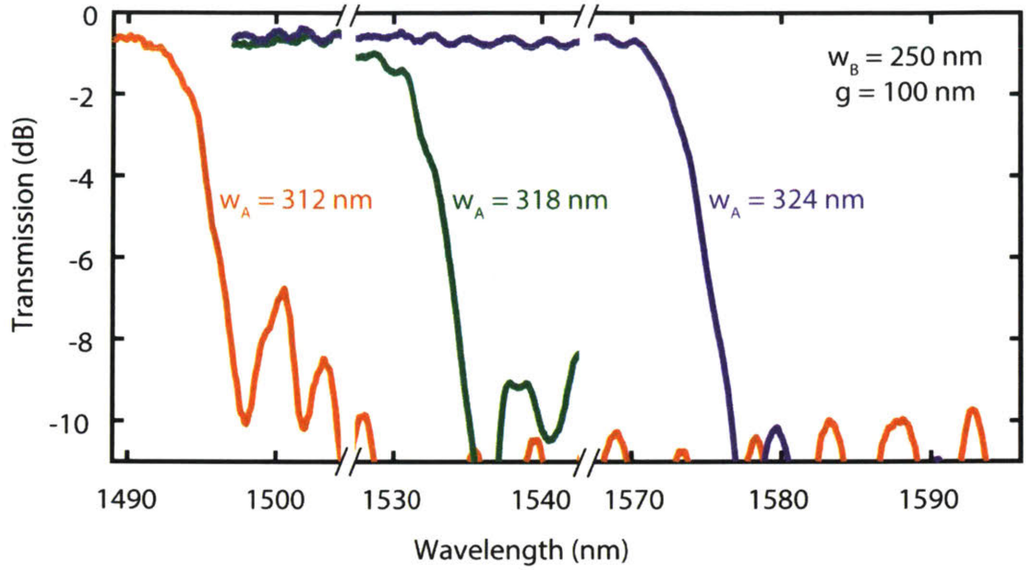

Figure 5-20: Shift of cutoff to longer wavelengths due to increasing w_A from 312 nm to 324 nm. The simulated and measured cutoffs are 1500.7 nm and 1495.1 nm for $w_A = 312$ nm, and 1572.2 nm and 1573.9 nm for $w_A = 324$ nm.

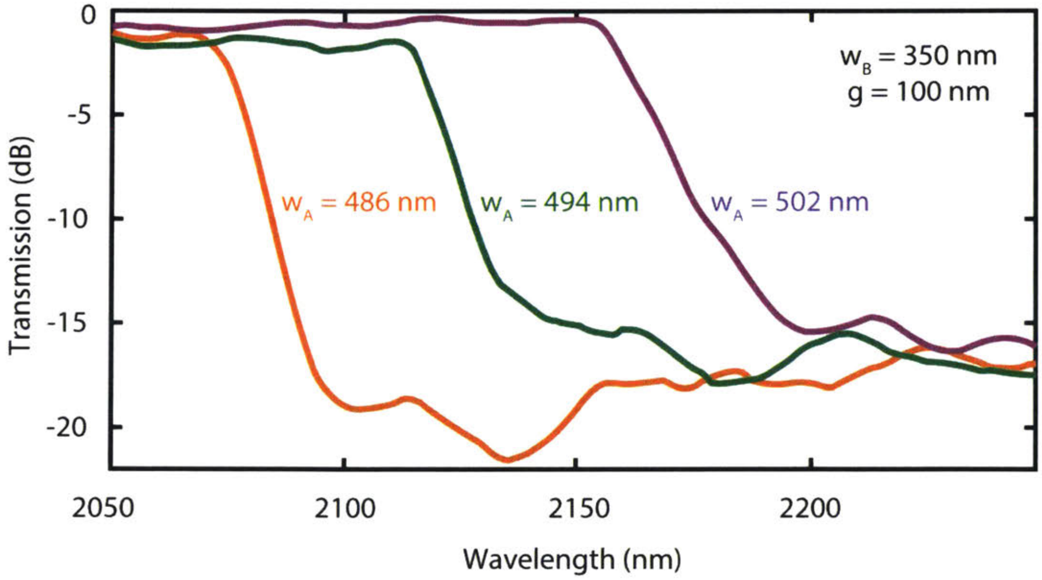

Figure 5-21: Similar shifts for the longer wavelength filters where simulated and measured cutoffs are 2078.5 nm and 2076.5 nm for $w_A = 486$ nm, and 2169.6 nm and 2162.4 nm for $w_A = 502$ nm.

5.3.6 Thermal Tunability of Filter Cutoff

Due to the high thermo-optic shift of $dn/dT = 1.86\text{x}10^{-4}$ K^{-1} in Si [62], the dichroic filter's cutoff wavelength can be tuned efficiently with a thermal shifter. Here, tunability is enabled by the unbalanced changes in the effective indices of individual waveguide modes ψ_A and ψ_B. According to eigenmode solutions at different temperatures, the temperature dependence of β_A is approximately twice as large as that of β_B. The difference in thermal shifts arises from the respective geometries of the two waveguides: WG_A is a strip waveguide confining a majority of the field within its core. In contrast, WG_B is a slot waveguide where there is a significant amount of field in the gaps between the waveguide cores. This explains the smaller thermal dependence of β_B, as SiO_2 typically exhibits a thermo-optic coefficient of approximately 10^{-5} K^{-1}, smaller than that of Si by more than an order of magnitude.

In order to quantify the thermally induced cutoff shift, we used a linear approximation to the thermal and wavelength dependence of the effective indices of ψ_A and ψ_B. Namely, the effective indices of ψ_A and ψ_B were approximated as linear functions of wavelength and temperature according to

$$n_{A,B}(\lambda, T) = n_0 + \left.\frac{\partial n_{A,B}}{\partial \lambda}\right|_{\lambda_C} (\lambda - \lambda_C) + \left.\frac{\partial n_{A,B}}{\partial T}\right|_{T_0} (T - T_0) \tag{5.39}$$

The approximation was calculated around the simulated cutoff wavelength of $\lambda_C = 1539.6$ nm, and the free-running operation temperature of $T_0 = 22.6$ °C as measured by the TEC. The dependence on wavelength was determined from the data in Figure 5-8; and the temperature dependence was extracted from eigenmode solutions by changing the refractive index of the core and cladding materials at a rate of $dn_{Si}/dT = 1.86\text{x}10^{-4}$ K^{-1} and $dn_{SiO2}/dT = 1\text{x}10^{-5}$ K^{-1}. For the linear fits, eigenmode simulations were performed with steps of $\Delta\lambda = 5$ nm, and $\Delta T = 5$ °C. The calculated derivatives of the effective indices with respect to wavelength and temperature as summarized in Table 5-1.

	n_A	n_B
$\partial/\partial\lambda$ (nm^{-1})	-1.575×10^{-3}	-0.798×10^{-3}
$\partial/\partial T$ (K^{-1})	1.685×10^{-4}	0.927×10^{-4}

Table 5-1: Linear approximations to the dependence of effective indices of ψ_A and ψ_B on wavelength and temperature, around the cutoff wavelength and nominal operating temperature.

Once we know the derivatives for each effective index with respect to wavelength and temperature, we can estimate the thermally induced wavelength shift in the following manner. We know that the effective indices n_A and n_B must be equal at the new temperature and the new shifted cutoff wavelength:

$$n_A(\lambda_{\text{new}}, T_{\text{new}}) = n_B(\lambda_{\text{new}}, T_{\text{new}}) \tag{5.40}$$

Plugging in from equation (5.39), we get

$$\frac{\partial n_A}{\partial \lambda}\Delta\lambda + \frac{\partial n_A}{\partial T}\Delta T = \frac{\partial n_B}{\partial \lambda}\Delta\lambda + \frac{\partial n_B}{\partial T}\Delta T \tag{5.41}$$

where we defined the change in wavelength as $\Delta\lambda = \lambda_{\text{new}} - \lambda_C$ and the change in temperature as $\Delta T = T_{\text{new}} - T_0$. Then it follows that

$$\frac{\Delta\lambda}{\Delta T} = -\frac{\frac{\partial}{\partial T}(n_A - n_B)}{\frac{\partial}{\partial \lambda}(n_A - n_B)} \tag{5.42}$$

Using the parameters from Table 5-1, we find that $\Delta\lambda/\Delta T$ is equal to 94.5 pm/K or 11.9 GHz/K. This is experimentally confirmed as shown in Figure 5-22 where we plotted the normalized filter transmission at the long-pass output as a function of substrate temperature from 12.5 °C to 55.0 °C using a closed-loop thermo-electric controller placed in contact with the chip. The cutoff at each temperature is plotted separately in Figure 5-23, from which the thermal shift was measured to be 14.4 GHz/K using a linear fit. Fabrication-induced waveguide geometry changes can explain the mismatch between the expected and measured thermal shifts, as the thermo-optic shifts in strongly-guided modes depend heavily on mode confinement. Overall, the measurement confirms that our dichroic filters can achieve thermal performances similar to the tunability commonly observed in Si Bragg reflectors and ring resonators where measured shifts are on the order of 10 GHz/K [113]. Moreover, for many of the filters measured, the cutoff can be tuned back to the design target, or to any desired wavelength with temperature changes on the order of few 10s of °C, which can be efficiently achieved by integrated heaters.

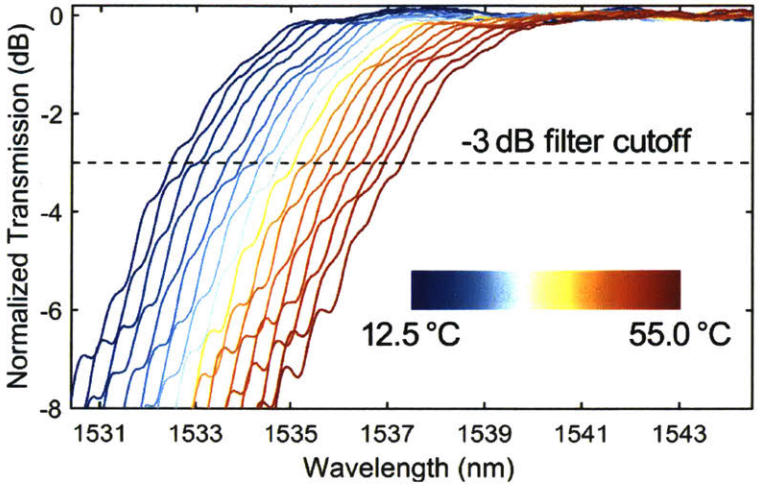

Figure 5-22: Transmission at the long-pass port of the dichroic filter as a function of temperature

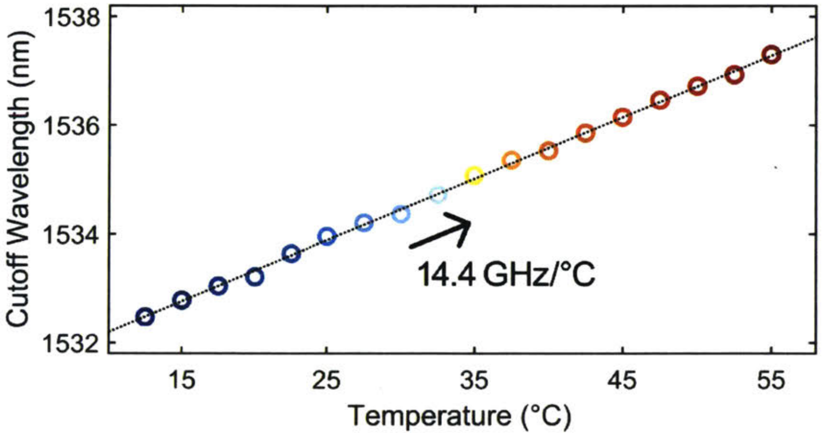

Figure 5-23: Thermal tunability of cutoff wavelength where the 3 dB point is plotted as a function of temperature

5.3.7 Discussion of Spectral Filtering Capabilities and Possible Enhancements

The approach presented here provides a clear methodology to design highly-selective, broadband, single-cutoff, transmissive, and low-loss optical filters based on the novel spectrally selective waveguide designs. Since the transmission response relies on the propagation constants in the two waveguides [equation (5.31)], it is possible to design and integrate similar filters at visible or mid-infrared wavelengths using other core materials such as Si_3N_4, Al_2O_3, or TiO_2.

Unlike devices that rely on propagation length to transfer power to an adjacent waveguide, the mode-evolution-based design here allows for the cutoff wavelength to be determined independent of coupler length. Optimizing the transition sections to suppress the fringing in the reject-bands and to improve the extinction ratio would be valuable topics for future studies. Improvements may be possible when using a cross-section similar to the one shown in Figure 5-6, or lower index-contrast waveguides, due to reduced interaction of the guided mode with the sidewalls. However, material choices are limited since phase matching at the cutoff wavelength poses strict restrictions on the material index.

The mismatch between the measured cutoff wavelength and the design target can be attributed to width and height changes that affect propagation constant due to fabrication, as commonly seen in the responses of many integrated devices such as Bragg reflectors, Mach-Zehnder interferometers, or ring resonators. More precise cutoff shifts may be possible with the use of wider waveguides at the expense of introducing higher order modes, as the change in effective index gradually decreases with increasing width. Thermal tuning of the cutoff wavelength is also demonstrated, as this is commonly required in reconfigurable optical systems. An accurately controlled wavelength shift is significant when designing band-pass filters, and therefore can be achieved by cascaded combinations of tunable short-pass and long-pass filters described here. Devices demonstrated here can be used in many optical systems including ultra-broadband multiplexing and demultiplexing systems in communications, efficient pump couplers to laser cavities, optical signal processing applications where arrays of arbitrarily wide band-pass filters are needed, and spectroscopy measurements that require spectral separation of excitation and output signals closely spaced in wavelength. Optical environmental sensors such as those used in index or concentration measurements or distance and velocity sensing like light imaging, detection and ranging (LIDAR) can also benefit from the filters described here, as these seonsors transduce wavelength selectivity to other measured quantities.

6 WAVELENGTH SPLITTERS BASED ON THE DIRECTIONAL COUPLER ARCHITECTURE

This chapter focuses on alternative wavelength selective couplers based on Mach-Zehnder interferometers. We first discuss various limitations and tolerances of a directional coupler, then introduce the transfer matrix approach, and design and analyze the expected response from the proposed broadband coupler.

6.1 Limitations of a Typical Directional Coupler

The typical spectral response of a single directional coupler was previously shown in Figure 5-5. This response can be utilized to design a device that would couple "long" wavelengths to the adjacent waveguide while retaining the "short" wavelengths at the input waveguide. The goal here is to use this directional coupler in order to separate 1f (2300 nm) and 2f (1150 nm) signals in an octave-wide input signal. Although various limitations exist for operation beyond the first 100 % coupling length, designing such a device is relatively simple and straightforward. An example is shown in Figure 6-1. In this directional coupler Si waveguides with 380 nm height and 650 nm width were separated by a gap of 400 nm in the coupling section. The S-bends on either side of the coupler were designed with a lateral shift of 5 μm and a horizontal propagation distance of 12 μm.

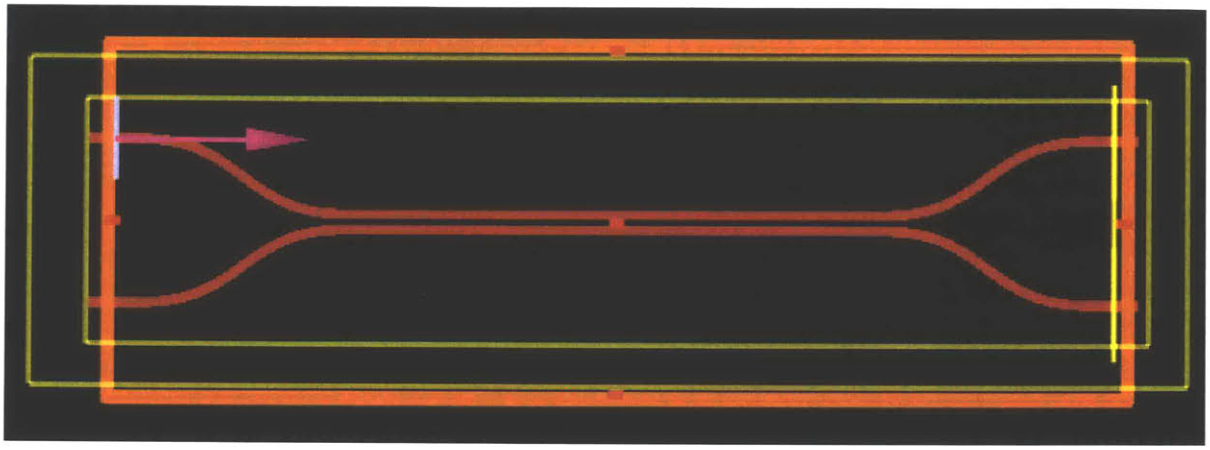

Figure 6-1: Design of 2x2 symmetric directional coupler with S-bends for input and output waveguides

The designed coupler was simulated using FDTD methods where a transform-limited pulse is applied as the input (the top left port), and the transmission on the top right and bottom right ports are recorded. The FDTD simulation results from the above directional coupler are plotted in Figure 6-2. The simulation was repeated 3 times with input signals at different center wavelengths: As designed, maximum transmission was achieved around 2300 nm, which was the design wavelength for the first 100 % coupling for a coupling length of 32.6 μm. The transmission around the 1550 nm C-band was approximately -20 dB. And finally, the transmission for much shorter wavelengths such as round 1150 nm was below -30 dB.

The proper length for the directional coupler here was 32.6 μm, which was slightly shorter than the length directly calculated from equation (5.38). This is due to the non-zero coupling acquired as the light propagates through the input and output S-bends. The exact amount of coupling achieved in the S-bend sections depends mainly on final gap of the waveguides. Assuming a 10 μm initial separation, and a horizontal propagation distance of 12 μm, the relative coupled power through the S-bends is given in Figure 6-3. Clearly, for larger gaps, the amount of power coupled decays exponentially. Consequently, in directional couplers with larger coupling gaps, including the coupling introduced by the S-bends isn't as crucial.

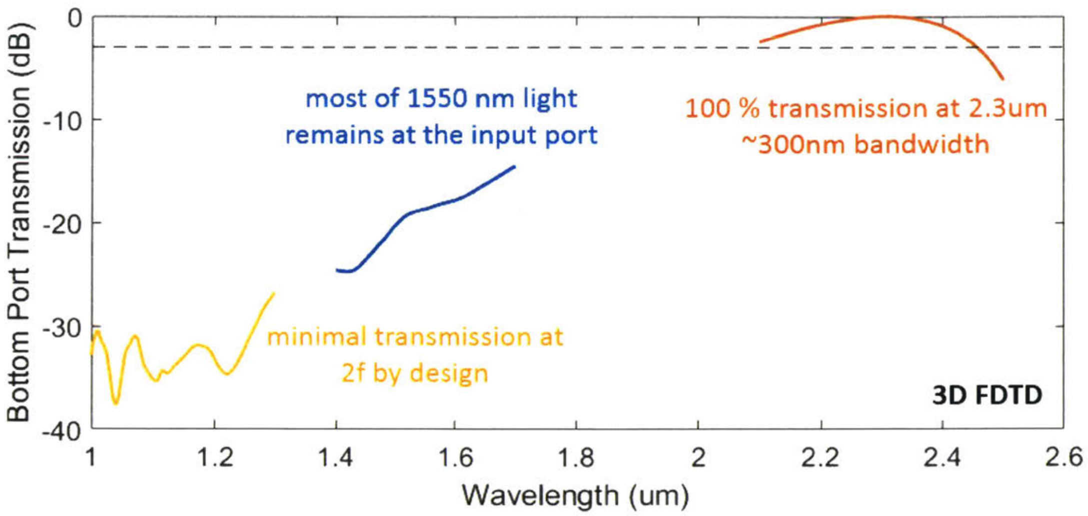

Figure 6-2: FDTD simulation result for transmission at the bottom right port of a directional coupler

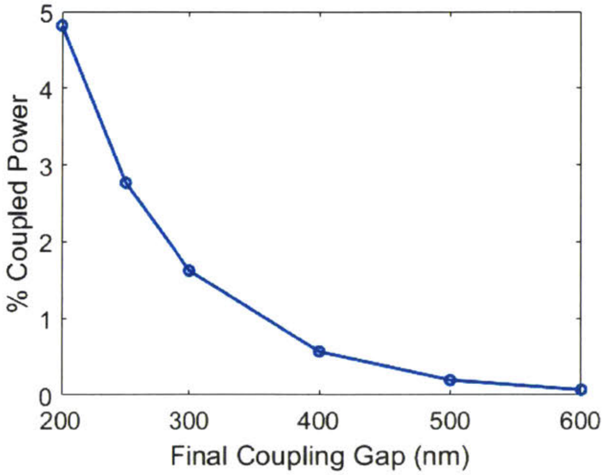

Figure 6-3: % power coupled through input and output S-bends as a function of coupling gap in a directional coupler

The 3 dB bandwidth of the proposed directional coupler from Figure 6-2 is about 350 nm. This wide bandwidth is partially due to having designed the first 100 % coupling wavelength around 2300 nm at which point the waveguide is less dispersive than around 1550 nm. A bandwidth is also crucial in terms of producing high-yield devices where each directional pair works as intended after fabrication. Most importantly, variations in waveguide widths, gaps, or layer heights due to finite fabrication tolerances impact the spectral response. All of these variations can be interpreted in terms of modified effective indices of the individual modes or the even/odd modes in the directional coupler. Each one these fabrication tolerance analyses is summarized, analyzed, and simulated in the following sections.

6.1.1 Waveguide Width Variations

With a changing waveguide width, we assume that both waveguides in the coupling section undergo the same changes. We also assume that the gap stays constant. Any difference from the design width of 650 nm will result in modified mode profiles and effective indices. For wider waveguides, the effective indices would increase, and the individual waveguide modes would become more confined. Consequently, achieving the same amount of coupling at the design wavelength would require a longer coupling section. For the same length of the device, longer wavelengths would satisfy the 100 % coupling condition. Therefore the 100 % coupling point would shift to longer wavelengths. An analysis of the changing coupled power is shown in Figure 6-4. Due to the wide bandwidth, the coupling changes by approximately ±4 %, which is tolerable in many applications, especially for a coupler designed with 100 % transmission.

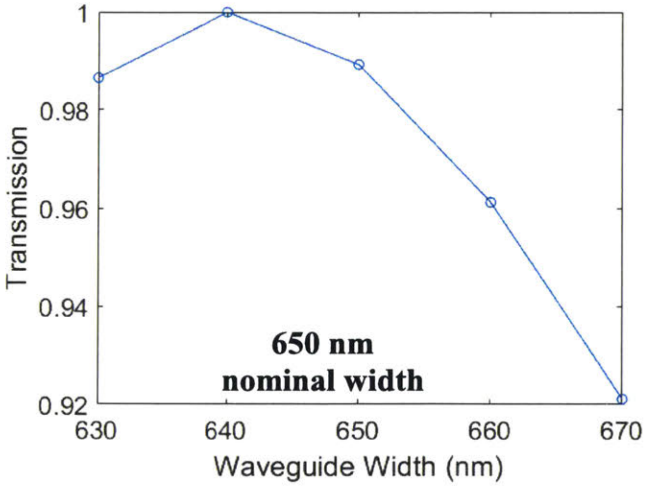

Figure 6-4: Transmission tolerance analysis in a 2x2 directional coupler with respect to waveguide widths

6.1.2 Waveguide Gap Variations

An increasing gap between the waveguides has the same effect as with increased waveguide widths: A larger gap results in decreased interaction and a smaller coupling coefficient, and a smaller percentage of coupled power. In order to retain the percentage of power coupled, one then needs a longer coupling section. With the same length, longer wavelengths achieve higher coupling as before. This analysis is shown in Figure 6-5, where due to the larger bandwidth, the transmission change again remains around ±3 %, for a ±20 nm change in the gap.

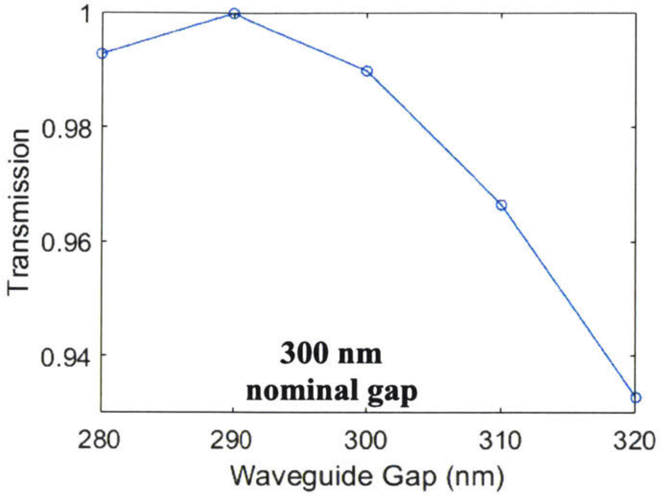

Figure 6-5: Transmission tolerance analysis in a 2x2 directional coupler with respect to coupler gap

6.1.3 Si Layer Height Variations

Similar to the increased width, a taller Si layer results in more confined modes in the waveguide cores. As a result, the coupling coefficient between the two modes decreases. Therefore, 100 % coupling at the design wavelength requires a longer coupler. Alternatively, an increased layer height results in reduced coupling at the design wavelength of 2300 nm. With a ±20 nm change in the layer height, the coupled power shown in Figure 6-6 changes by about ±2 %. The small change compared to similar amounts of width and gap variation can be attributed to the TE modes indices being less dependent on the layer height.

Although the tolerance analyses show that typical fabrication-induced changes in waveguide geometry change the performance of the directional coupler by a few %, it is desirable to reduce the effects of such changes to a minimum. A previously proposed and implemented approach is utilized in the next section, for a broader-band wavelength-sensitive coupler.

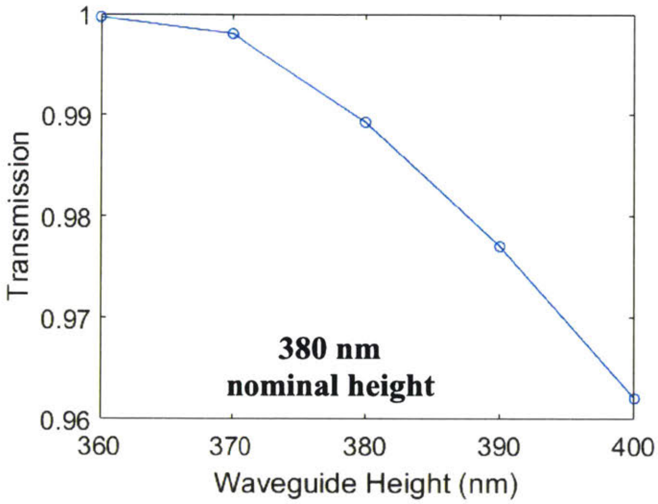

Figure 6-6: Transmission tolerance analysis in a 2x2 directional coupler with respect to Si layer height

6.2 Transfer Matrix Representation

Following the form of equation (5.35), a directional coupler can be represented by the transfer matrix

$$M = \begin{bmatrix} t & -jq \\ -jq & t \end{bmatrix} \tag{6.1}$$

where t and q are the amplitude coefficients for the transmitted and coupled (or reflected depending on the device type) waves. M is symmetric since coupling from one waveguide to another is a symmetric phenomenon. M is also unitary due to conservation of power where we have

$$M^{\dagger}M = \begin{bmatrix} t & jq \\ jq & t \end{bmatrix}\begin{bmatrix} t & -jq \\ -jq & t \end{bmatrix} = \begin{bmatrix} |t|^2 + |q|^2 & 0 \\ 0 & |t|^2 + |q|^2 \end{bmatrix} = I \tag{6.2}$$

For symmetric waveguides, we know that the propagation constants are the same ($\delta = 0$), and $S = \kappa$. Then, by pairing the transfer matrix M with the more general description from equation (5.35), we can represent the amplitude coefficients in terms of the waveguide parameters as

$$t = \cos \kappa z \qquad \text{and} \qquad q = \sin \kappa z \tag{6.3}$$

In the case of a varying coupling coefficient κ along the propagation direction, equation (6.3) takes the following form

$$t = \cos \int \kappa(z)dz \qquad \text{and} \qquad q = \sin \int \kappa(z)dz \tag{6.4}$$

Any variations in the geometry such as waveguide widths, gap, or even height can be lumped in to changes in the coupling coefficient κ. Consequently, the description in (6.4) allows us to treat a general family of couplers with the same transfer matrix given in equation (6.1). For instance, the input and output S-bends shown in Figure 6-1 can be represented by transfer matrices of their own with the same format, regardless of the varying waveguide gap.

Using the generalized transfer matrix representation in equation (6.1), we can then represent the full transfer matrix of the input S-bends, the directional coupler, and the output S-bends as

$$\begin{aligned} M_{\mathrm{DC}} = SMS &= \begin{bmatrix} t_S & -jq_S \\ -jq_S & t_S \end{bmatrix} \begin{bmatrix} \cos \kappa L_c & -j\sin \kappa L_c \\ -j\sin \kappa L_c & \cos \kappa L_c \end{bmatrix} \begin{bmatrix} t_S & -jq_S \\ -jq_S & t_S \end{bmatrix} \\ &\equiv \begin{bmatrix} t_{\mathrm{DC}} & -jq_{\mathrm{DC}} \\ -jq_{\mathrm{DC}} & t_{\mathrm{DC}} \end{bmatrix} \end{aligned} \tag{6.5}$$

where we defined the transmission and coupling amplitude coefficients for a single directional coupler as t_{DC} and q_{DC} respectively. For a given coupling gap and a waveguide geometry, the amount of coupling through just the input and output S-bends can be solved from the transfer matrix of the 2 S-bends given by

$$M_{\mathrm{S}} = SS = \begin{bmatrix} t_S & -jq_S \\ -jq_S & t_S \end{bmatrix} \begin{bmatrix} t_S & -jq_S \\ -jq_S & t_S \end{bmatrix} = \begin{bmatrix} t_S^2 - q_S^2 & -2jt_Sq_S \\ -2jt_Sq_S & t_S^2 - q_S^2 \end{bmatrix} \tag{6.6}$$

Then, using the FDTD simulation results from Figure 6-3 of just the input and output S-bends, t_S, q_S, and the power coupled in the S-bends Q_S can be related by

$$\left| M_{\mathrm{S}} \begin{bmatrix} 1 \\ 0 \end{bmatrix} \right|^2 = \begin{bmatrix} (t_S^2 - q_S^2)^2 \\ 4t_S^2 q_S^2 \end{bmatrix} = \begin{bmatrix} 1 - Q_S \\ Q_S \end{bmatrix} \tag{6.7}$$

where we imposed power conservation by setting the transmitted power to $1 - Q_S$. This is equivalent to having $t_S^2 + q_S^2 = 1$. Here, one can safely assume $t_S > q_S$ for a typical S-bend as majority of the power remains in the input waveguide.

6.3 A Pair of Cascaded, Point-Symmetric, Unbalanced MZIs as a Broadband Wavelength Splitter

In this section, we study the design of a different class of ultra-broadband couplers based on directional couplers and unbalanced MZIs. The main goal here is to overcome the bandwidth limitations of typical directional couplers without having to use long adiabatic couplers as in the previous section. The overarching design approach is shown in Figure 6-7 where a pair of 50/50 couplers are cascaded to form a 100/0 coupler at the desired design wavelength. Such a coupler can be used in many different applications that require spectral filtering, splitting, or combining. Specifically, Figure 6-7 outlines the use of the device in a 1f-2f frequency locking scheme where an octave-wide supercontinuum (SC) is separated to its 1f and 2f parts by the broadband splitter. Then, an integrated 2nd harmonic generator (SHG) converts the input 1f signal into 2f, preparing it for beat-note analysis with the corresponding 2f signal from the supercontinuum.

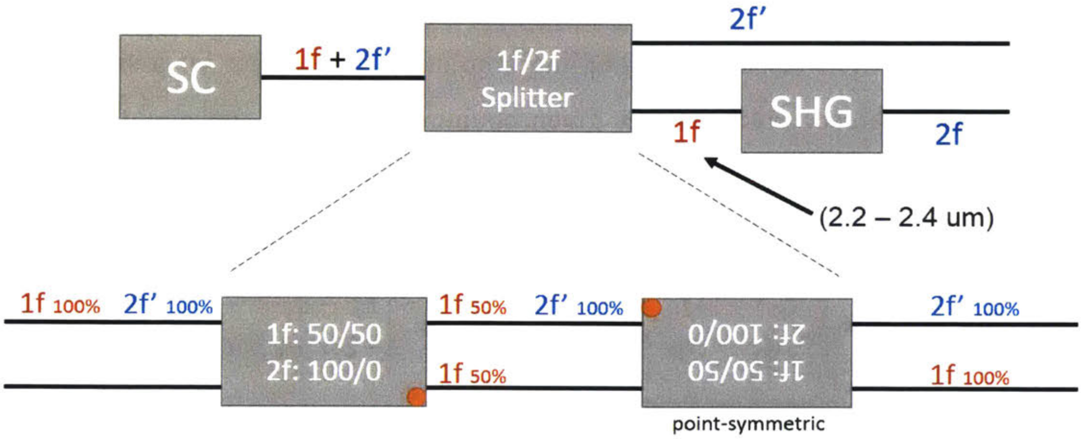

Figure 6-7: Design of a broadband wavelength splitter made from cascaded point-symmetric MZIs (SC: supercontinuum, SHG: 2nd harmonic generator)

6.3.1 Point-Symmetric Cascading of Couplers

The specific reason why a point-symmetric cascade is employed in Figure 6-7 lies in the resulting bandwidth of the overall coupler. This is demonstrated in Figure 6-8 where the cascaded response from a 50/50 coupler shows less power variation from the 100 % goal across the pass-band, and therefore a wider bandwidth [114]. The transmission response shown here is different than the example of the typical directional coupler shown in Figure 5-5. That's because the response used here belongs to a different family of couplers called wavelength insensitive couplers [115], as detailed in the next section.

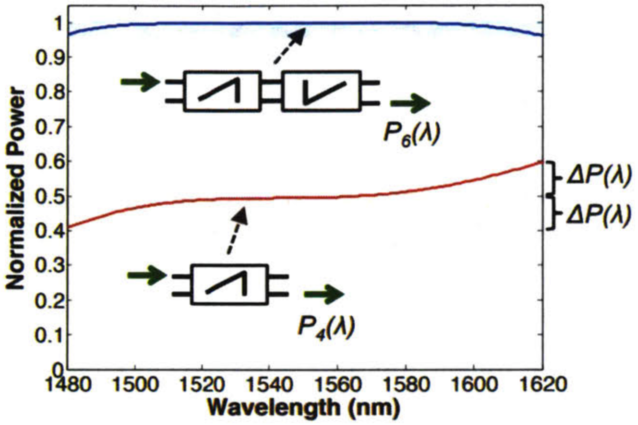

Figure 6-8: Spectral responses from a single 50/50 coupler, and a cascaded pair of the same coupler, reproduced from [114]

6.3.2 Wavelength-Insensitive Couplers

Cascading couplers with different properties is one of the most versatile techniques used in integrated photonics. A set of cascaded couplers can perform functionalities that a single directional coupler, Y-branch, or MMI coupler cannot perform on its own. Wavelength-insensitive couplers are an important example of such cascaded devices that can achieve wider-band operation than conventional directional couplers. An example of a wavelength-insensitive coupler schematic is shown in Figure 6-9 where a phase difference is introduced in one of the arms of a Mach-Zehnder interferometer. This phase difference can be designed to mitigate the narrowband response from a typical directional coupler.

In the wavelength-insensitive coupler, the two directional couplers together with the phase difference introduced between them have to satisfy certain transmission amplitude coefficients in order for the overall coupler response to be 50/50. The overall transfer function for the whole coupler is given by

$$\begin{aligned} M_{\mathrm{MZI}} &= M_{\mathrm{DC}} M_{\mathrm{taper}} M_{\mathrm{P}} M_{\mathrm{taper}} M_{\mathrm{DC}} \\ &= (SMS) M_{\mathrm{taper}} \begin{bmatrix} e^{-j\theta_1} & 0 \\ 0 & e^{-j\theta_2} \end{bmatrix} M_{\mathrm{taper}} (SMS) \\ &\equiv \begin{bmatrix} t_{\mathrm{MZI}} & -jq_{\mathrm{MZI}} \\ -jq_{\mathrm{MZI}} & t_{\mathrm{MZI}} \end{bmatrix} \end{aligned} \tag{6.8}$$

where we expanded the phase section in the two arms by defining the effective indices in the two arms as n_1 and n_2, and defining the angles $\theta_1 = (2\pi n_1/\lambda)L_p$ and $\theta_2 = (2\pi n_2/\lambda)L_p$. In this design, the phase difference is achieved by changing the waveguide width in the two arms as opposed to physically adding a longer top arm in the MZI. This can potentially provide finer control of the phase difference as dn/dw only exhibits minute changes. Specifically, for a nominal width of 650 nm in a 380 nm thick Si layer, MZIs with 700/600 nm, 675/625 nm, and 660/640 nm top/bottom arms have been designed.

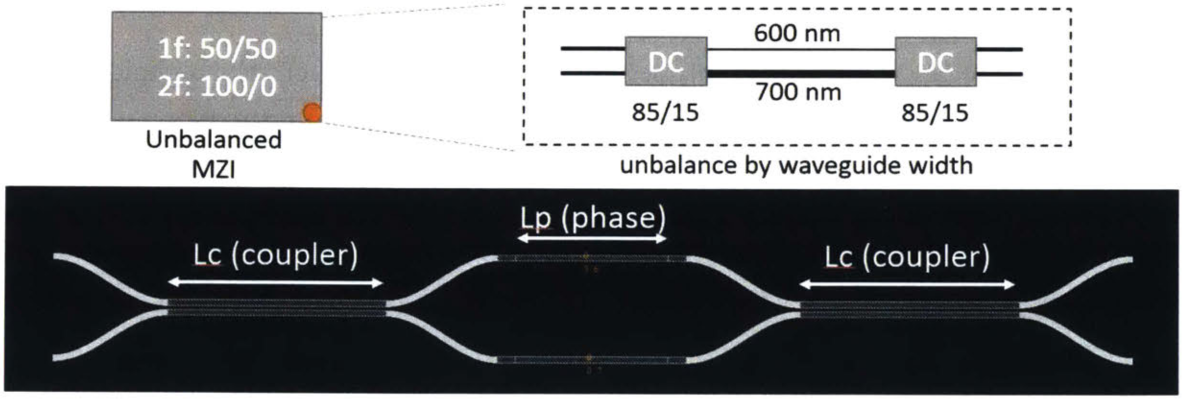

Figure 6-9: Design of an unbalanced MZI with phase-section in between two directional couplers

The overall transfer matrix also includes tapers of length L_t for either side of the phase section. Designing the tapers with a linear change in waveguide width, we can write the phase acquired by going through the tapers as

$$\begin{aligned} \theta_t &= \frac{2\pi}{\lambda}\int_0^{L_t} n(z)dz = \frac{2\pi}{\lambda}\int_0^{L_t}\left(n_0 + \frac{z}{L_t}(n_{1,2} - n_0)\right)dz \approx \frac{2\pi}{\lambda}\sum_{i=1}^{m} n_{w_m}\frac{L_t}{m} \\ &= \frac{2\pi}{\lambda}L_t\sum_{i=1}^{m}\frac{n_{w_m}}{m} = \frac{2\pi}{\lambda}\bar{n}L_t \end{aligned} \tag{6.9}$$

Here, we evaluated the phase in each infinitesimally short part of the taper section by defining $n(z)$, and then used a piecewise-constant approximation to the linearly changing taper. The result is that the phase acquired through the taper is equivalent to the phase acquired through a straight waveguide whose effective index is the average effective index in the tapered section. It is important to note that the average effective index $\bar{n}$ is different for the top and bottom tapers since the widths in the phase section are different. Therefore, the transfer matrix for the taper section is given by

$$M_{\text{taper}} = \begin{bmatrix} e^{-j\frac{2\pi}{\lambda}\overline{n_{\text{top}}}L_t} & 0 \\ 0 & e^{-j\frac{2\pi}{\lambda}\overline{n_{\text{bot}}}L_t} \end{bmatrix} \tag{6.10}$$

where $\overline{n_{\text{top}}}$ and $\overline{n_{\text{bot}}}$ the average effective indices in the top and bottom arms of the MZI respectively.

It is also important to point out that the two tapers in the top arm have the same transfer function even though one is simply the reverse of the other. By equation (6.9), even though the transition is reversed from one taper to the other ($n_1 \rightarrow n_0$ instead of $n_0 \rightarrow n_1$), the average effective index is the same in the two linear tapers. Therefore, the same amount of phase is picked up when light goes through the tapers; and the transfer matrix stays the same. It would be incorrect to invert the transfer function and use M_{taper}^{-1} as this results in the acquired phase being lost, and does not represent the physical propagation in this coupler. Also, one could simply show that in the case of a complex effective index to represent loss, an inverse transfer function would compensate for the loss by introducing gain, which again does not represent the physical processes in this device.

The coupler in Figure 6-9 can be designed with a specific polarization in mind, or for different coupling coefficients. For a given coupling coefficient, the coupling lengths required for different polarizations are significantly different due to the difference in their effective indices [116]. This fact has been previously used to design a broadband polarization beamsplitter where the fundamental TM mode coupled to the adjacent waveguide much quicker than the fundamental TE mode [114]. Here, we propose a similar mechanism to exploit the fact that longer wavelengths in a directional coupler are more strongly coupled than shorter wavelengths. Due to the increased coupling coefficient κ, the interaction length for longer wavelengths is therefore shorter. Then, in order to separate the 1f and 2f signals generated by the supercontinuum in Figure 6-7, the coupler can be designed to fully couple the long wavelength 1f signal to the adjacent port while maintaining the 2f signal at the input waveguide. This is supported by the FDTD results previously shown in Figure 6-2 where the transmission at 2f (1150 nm) is approximately 30 dB less than the transmission at 1f (2300 nm).

6.3.3 Coupling Ratio of the Unbalanced MZI

In order to design the correct coupler with the 50/50 coupling ratio, we solve for the remaining power in the input waveguide Q_{MZI} from

$$\left|M_{\mathrm{MZI}}\begin{bmatrix}1\\0\end{bmatrix}\right|^2=\begin{bmatrix}Q_{\mathrm{MZI}}\\1-Q_{\mathrm{MZI}}\end{bmatrix} \tag{6.11}$$

where the MZI transfer matrix M_{MZI} is given in equation (6.8), in the same manner that the splitting ratio is solved for in [116]. Of the three lengths in the transfer matrices, we set the taper length $L_t = 2$ µm, and plot the expected transmission Q_{MZI} as a function of the directional coupler length L_c and the phase section length L_p. The result is shown in Figure 6-10 at $\lambda_0 =$ 2300 nm.

We can interpret the results by analyzing the transfer response for the two different lengths separately: First we analyze the case where $L_p = 0$ µm, as we consider a slice along the horizontal axis of the contour plot. For a very short coupling length in the directional couplers, over 90 % of the input power remains in the same waveguide as indicated by the yellow region near the origin. With increasing coupling length, the remaining power oscillates following the expected $|t|^2 = \cos^2 \kappa L$ response from equation (6.3). Now, in order to analyze the effects of a changing phase section length L_p, we consider a vertical around $L_c = 30$ µm where most of the light is coupled to the adjacent waveguide when $L_p = 0$ µm. However, with a changing L_p the coupled power again oscillates due to the expected response of a typical MZI. The changing phase difference modulates the percentage of coupled power between the two output ports, as in a conventional MZI.

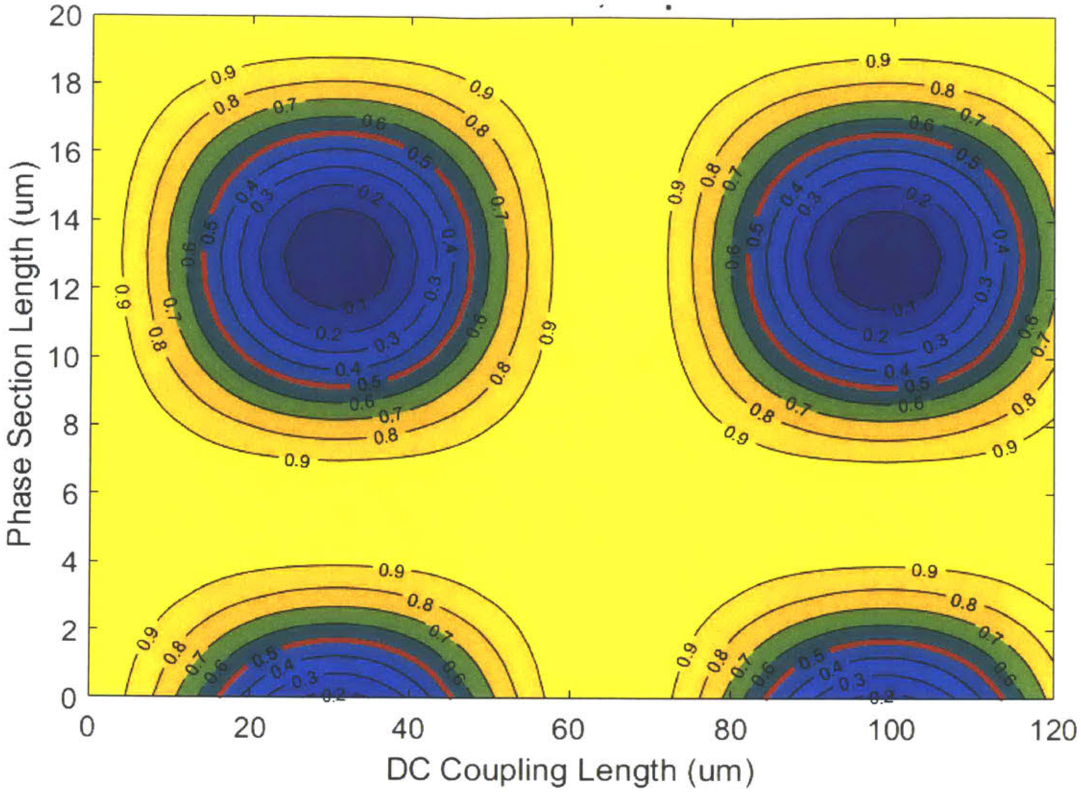

Figure 6-10: Power remaining the input waveguide of unbalanced MZI as a function of the DC coupling length and the phase section length

Since the device shown in Figure 6-7 requires a 50/50 coupling ratio for the MZI, the 0.5 contour line is highlighted with red in Figure 6-10. That means any pair of (L_c, L_p) along this red contour line would result in a 50/50 splitting ratio at the output ports of the MZI. However, in order to make the coupler as broadband as possible, only the first order solution with the shortest coupling and phase section lengths must be used. Therefore, we limit the device design to the bottom left red contour.

Then, following the method used in [116], we repeat the transfer matrix calculation as a function of wavelength around the desired center wavelength of $\lambda_0 = 2300$ nm. Simulations at each wavelength produce their own power splitting ratios similar to the plot in Figure 6-10. To calculate how much the power splitting ratio can change within the simulated wavelengths, we evaluate the absolute value of the maximum difference in Q_{MZI} between the simulated wavelengths and plot $|Q_{\mathrm{MZI}}(\lambda_0) - Q_{\mathrm{MZI}}(\lambda)|_{\max}$ in Figure 6-11.

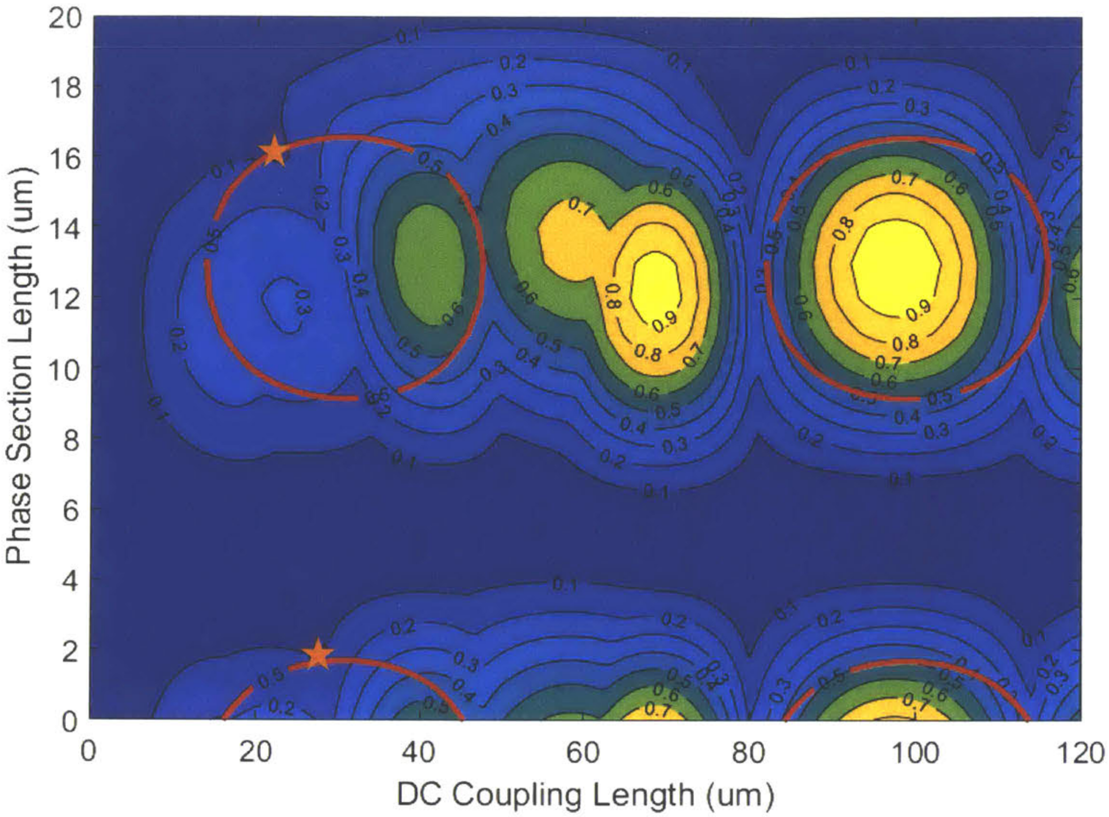

Figure 6-11: Maximum difference in coupled power of the unbalanced MZI as a function of the DC coupling length and the phase section length

Here, the red contours showing the 50/50 power splitting parameters are overlaid on top of the maximum difference in the power splitting ratio. As expected from the bandwidth analysis in Section 5.2, the minimum change in the coupled power is observed around the shortest possible length of the directional coupler. For this first order solution, as the response with changing L_p is periodic, there are multiple (L_c, L_p) pairs marked by the orange stars in Figure 6-11 that result in minimal changes in the power coupling ratio. However, the smallest change is again obtained at the first order solution at the bottom left corner, where $L_c = 22.25$ µm and $L_p = 16.14$ µm.

6.3.4 FDTD Simulations of Coupled Power

In order to verify the results from the transfer matrix based design above, the response of the designed 50/50 MZI is simulated using 3D FDTD. The result is plotted in Figure 6-12 showing the transmission in the top and bottom output ports. For this simulation, a transform-limited pulse of 300 nm spectral width has been launched into the top port of the MZI with a time-step of 0.07 fs, a non-uniform conformal mesh with a discretization of approximately 120 nm, and PML boundaries. As the expected response from the MZI is 50/50 at the center wavelength, the 3 dB bandwidth corresponds to 0.25 of the power coupled to the bottom port. According to the simulation results, the device's 3 dB bandwidth is wider than the launched 300 nm wide pulse, as the transmitted power at the bottom port does not drop below 0.3. Accordingly, we characterize the 1 dB bandwidth where the power at the bottom port drops to $0.5 \times 10^{-1/10} = 0.397$. This is achieved with a bandwidth of approximately 235 nm which is much larger than what can be achieved with a single directional coupler.

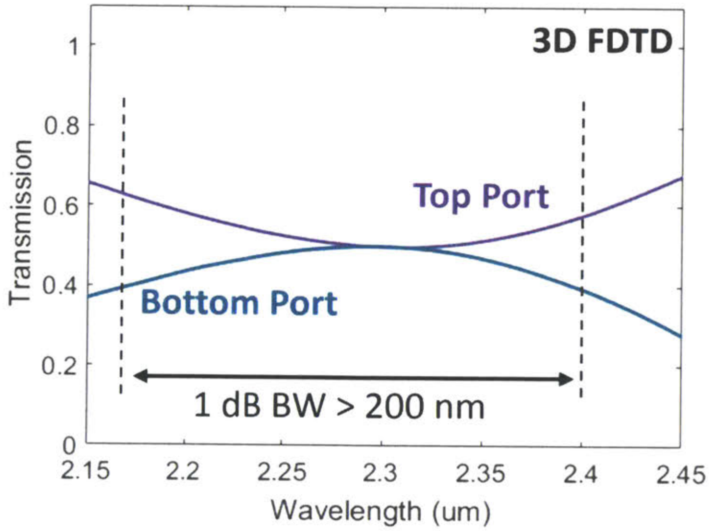

Figure 6-12: 3D FDTD simulation result of the 50/50 MZI around $\lambda_0 = 2300$ nm

The wideband operation is also clearly seen in the top-down view of the field profiles plotted in Figure 6-13. The profiles are shown at wavelengths of 2216 nm, 2300 nm, and 2388 nm. The 50/50 splitting ratio shows minimal change across the ±80 nm wavelength region, verifying the wideband response of the designed MZI.

6.3.5 Power Splitting in the Cascaded Coupler

So far, we have only simulated the response for one of the MZIs proposed in the design of the broadband wavelength splitter in Figure 6-7. Here, we complete the simulation results by calculating the expected transmission for the cascaded coupler using the point-symmetric MZI. Due to the length of the three dimensional FDTD simulation used just for half of the device, the results in this section are evaluated by the transfer matrix method.

The general form of the transfer matrix for an arbitrary circuit is given by the unitary matrix

$$G = \begin{bmatrix} a(\lambda) & -b^*(\lambda) \\ b(\lambda) & a^*(\lambda) \end{bmatrix} \tag{6.12}$$

The point-symmetric version where the device is reflected around the origin or its center is then given by

$$G_{PS} = \begin{bmatrix} a^*(\lambda) & -b^*(\lambda) \\ b(\lambda) & a(\lambda) \end{bmatrix} \tag{6.13}$$

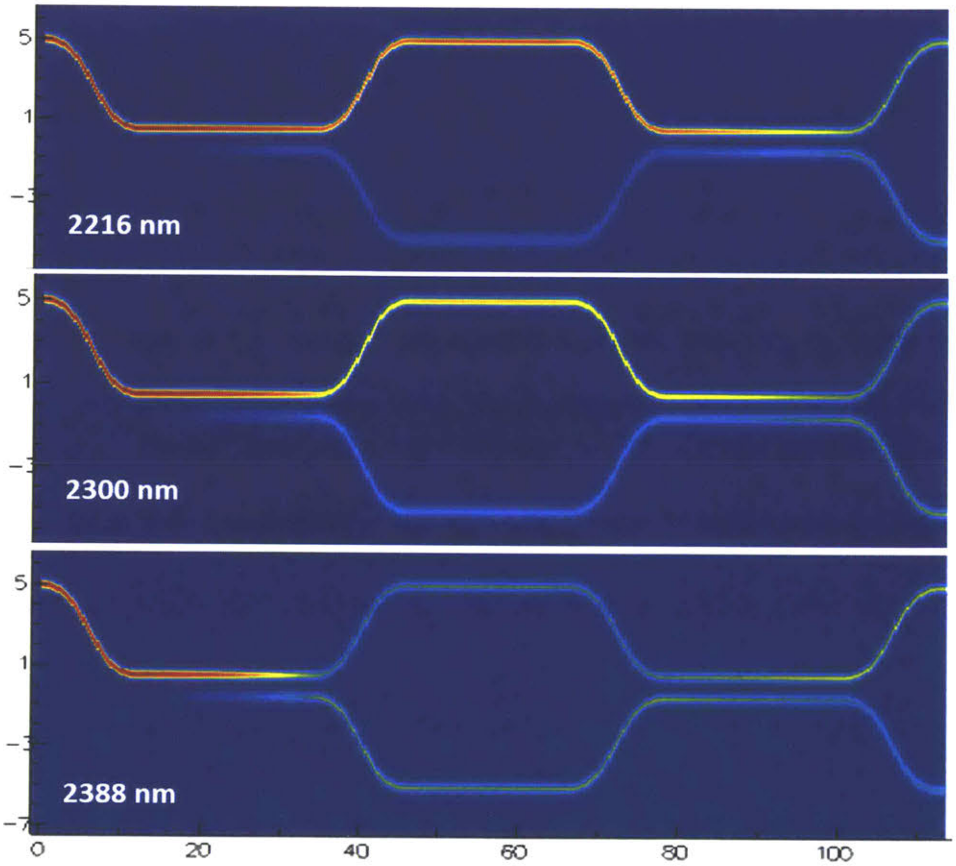

Figure 6-13: Top-down view of the field profiles for the unbalanced MZI with a 50/50 transmission at 2300 nm

From the form of G in equation (6.12), and the transfer matrices for S-bends, directional couplers, or MZIs studied in previous sections, we know that the parameters $t_S, t_{\mathrm{DC}}, t_{\mathrm{MZI}}, q_S, q_{\mathrm{DC}}, q_{\mathrm{MZI}}$ are all real. Therefore, in the case of the MZI pair studied here, we can calculate the overall transfer function using the definition in equation (6.8), which yields

$$\begin{aligned} M_{\mathrm{MZI}_{PS}} M_{\mathrm{MZI}} &= \begin{bmatrix} t^*_{\mathrm{MZI}} & -jq_{\mathrm{MZI}} \\ -jq_{\mathrm{MZI}} & t^*_{\mathrm{MZI}} \end{bmatrix} \begin{bmatrix} t_{\mathrm{MZI}} & -jq_{\mathrm{MZI}} \\ -jq_{\mathrm{MZI}} & t_{\mathrm{MZI}} \end{bmatrix} \\ &= \begin{bmatrix} t_{\mathrm{MZI}} & -jq_{\mathrm{MZI}} \\ -jq_{\mathrm{MZI}} & t_{\mathrm{MZI}} \end{bmatrix}^2 = \begin{bmatrix} t^2_{\mathrm{MZI}} - q^2_{\mathrm{MZI}} & -2jt_{\mathrm{MZI}}q_{\mathrm{MZI}} \\ -2jt_{\mathrm{MZI}}q_{\mathrm{MZI}} & t^2_{\mathrm{MZI}} - q^2_{\mathrm{MZI}} \end{bmatrix} \end{aligned} \tag{6.14}$$

The coupled and remaining power then are given by

$$\left| M_{\mathrm{MZI}_{PS}} M_{\mathrm{MZI}} \begin{bmatrix} 1 \\ 0 \end{bmatrix} \right|^2 = \begin{bmatrix} (t^2_{\mathrm{MZI}} - q^2_{\mathrm{MZI}})^2 \\ 4t^2_{\mathrm{MZI}} q^2_{\mathrm{MZI}} \end{bmatrix} \tag{6.15}$$

In order to evaluate the response of the cascaded coupler in equation (6.14), we first extract the parameters t^2_{MZI} and q^2_{MZI} from the top and bottom port transmissions in Figure 6-12. We can the plot the result of the transfer matrix calculation for the expected 100/0 transmission as shown in Figure 6-14.

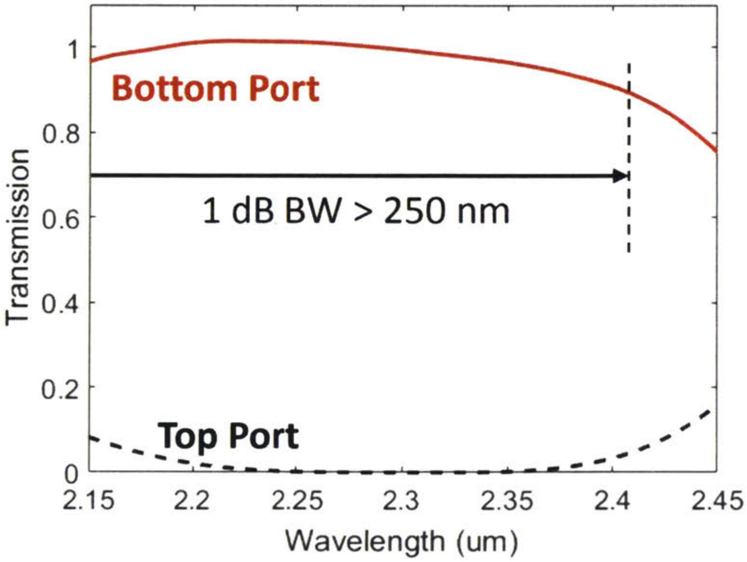

Figure 6-14: Spectral transmission of the cascaded coupler showing more than 250 nm of 1 dB bandwidth around 2300 nm

As expected, from the combination of two 50/50 couplers, a 100/0 coupler is obtained. Since each one of the 50/50 couplers is broadband, the resulting 100/0 coupler is ultra-broadband. The 1 dB bandwidth between the wavelengths where transition to the bottom port remains greater than $10^{-1/10} = 0.794$ can be estimated as larger than 250 nm from the shown response.

6.3.6 Time-Domain Response of the Broadband MZI Pair

Such a broadband device is crucial for the proper operation of any downstream devices in the photonic circuit. In this specific case, the extremely wide bandwidth of the proposed coupler ensures that the second harmonic generator following the coupler in Figure 6-7 functions properly. As the Si-based second harmonic generator makes use of a grating, its phase matching condition is significantly affected by any width and height changes due to fabrication. This is similar to the center wavelength shift observed in Bragg gratings due to imperfect fabrication that results in non-ideal waveguide widths and layer heights. The main goal of the broadband response is to mitigate any changes that might deteriorate the input power to the second harmonic generator, which in turn reduces its conversion efficiency.

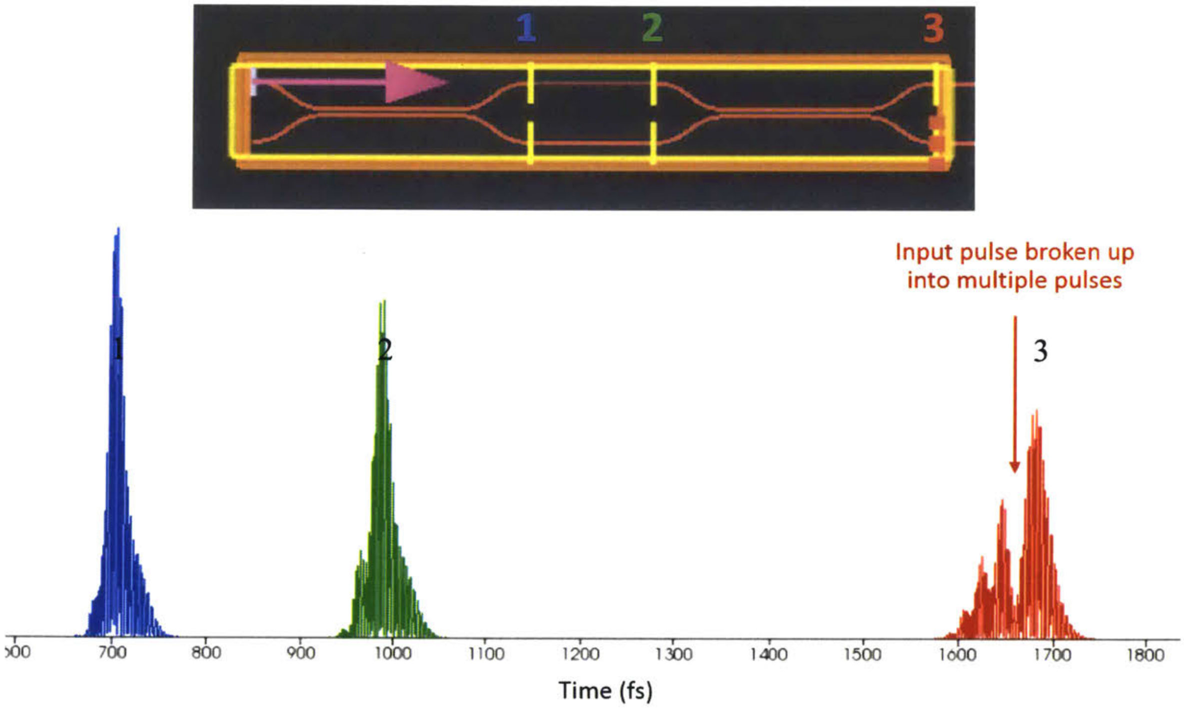

Figure 6-15: Time-domain response of the 50/50 unbalanced MZI

Depending on the target application, it is also important to analyze the time-domain behavior of designed components. Although the above proposed MZI pair functions perfectly from a spectral perspective, due to the phase delays introduced in the arms of the coupler, the time-domain response may cause issues for downstream devices.

The power recorded at the output of the unbalanced MZI can be extracted from time-domain monitors in the FDTD simulations. The result is shown in Figure 6-15, where the electric field in the propagating pulse is plotted at three separate monitors. All monitors are located in the top arm of the MZI; however, they are placed at different points along the propagation direction. After the first directional coupler, the input pulse retains its Gaussian envelope for the most part (1-blue). After going through the phase section, no significant changes are observed in the pulse shape other than the expected broadening due to material and waveguide dispersion (2-green). However, when the pulse goes through the second directional coupler, some of the light from the bottom port couples back to the top port. Due to the phase difference between the two arms, coupling in the second directional coupler introduces a delay between the parts of the pulse propagating in the top arm. The result is a pulse that is broken up largely into two segments (3-red).

The delay is also visibly observed from the FDTD snapshot in Figure 6-16. Due to the wider waveguide in the bottom arm of the MZI, the guided mode has a larger effective index, and therefore propagates slower than the mode in the top arm. At the beginning of the second directional coupler seen in Figure 6-16, when the two pulses meet, their phase difference results in the broken output pulse from the bottom output port of the MZI.

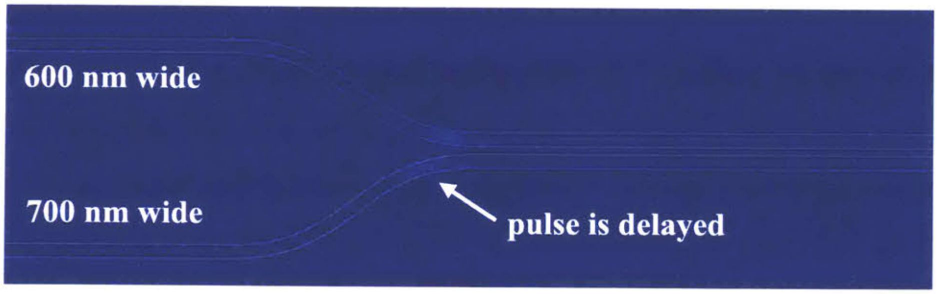

Figure 6-16: FDTD snapshot of propagating pulse in the unbalanced MZI coupler at the beginning of the second directional coupler, where the pulse in the bottom arm is delayed

Since the pulse energy is then distributed over a longer and non-Gaussian pulse, the peak power is reduced. Simpler circuits such as communication networks with on-off keying or low-order modulation schemes may be able to tolerate decreases in the input power. However, for more advanced circuits such as the 1f-2f lock described here, a decrease in peak power directly influences the conversion efficiency of the second harmonic generator. As a result, using this coupler instead of a simple directional coupler in this network may require stronger pumping of the upstream supercontinuum generator, or amplifiers in between the individual components.

6.4 Conclusion

We studied the design of directional couplers in relation to their spectral response, and showed how they can be used as wavelength splitter/combiner structures. By making use of waveguide dispersion, we designed an example directional coupler in Si that can separate 1f & 2f signals at 2300 nm and 1150 nm with an extinction of more than 30 dB, and a 3 dB bandwidth of over 250 nm at the output port where the 1f signal is expected. The large bandwidth shown here is due to the first order solution of the coupling length, which results in the shortest device with the largest possible bandwidth. Then, we designed an even broader-band wavelength splitter by making use of the unbalanced MZI architecture proposed earlier for splitting TE/TM modes. Here, utilizing the fact that the coupling length is different for 1f and 2f signals due to waveguide dispersion, we proposed, simulated, and analyzed a coupler that achieves near 100 % transmission around 2300 nm with a 1 dB bandwidth of more than 250 nm. The shorter wavelength, due to its more confined mode profile and increased necessary interaction length stays at the input port, and is therefore separated from the 1f signal at the output. Time domain simulations suggest that the phase unbalance utilized in this MZI coupler can break up the input pulse and reduce the peak power at the longer wavelength. This may be important to consider in cases where downstream devices such as a second harmonic generator may require a high peak power in order to operate efficiently. In other words, gaining bandwidth at the splitter stage might adversely affect system operation due to the reduced peak power. One will have to test specific combinations of splitters and frequency doublers to evaluate the overall system performance according to application specific metrics.

7 SUMMARY AND OUTLOOK

In this thesis, various types of integrated silicon photonic devices were studied in regards to applications that require generation, stabilization, and efficient manipulation of light. Objectives including creating a CMOS-compatible light source, an integrated stabilization reference, and ultra-broadband spectral separation mechanisms have been achieved. Additionally, methods for characterizing gain media have been developed and utilized.

The lower temperature deposition of Al_2O_3 at 250 °C was first demonstrated using substrate bias assistance. The surface mobility that is achieved at high temperatures was compensated for by bombarding the surface with Ar^+ ions during deposition, acting as a polishing agent. As a result, resultant films yielded much smoother surfaces with scattering losses below 0.2 dB/cm. Resulting films were used in designing and fabricating a DFB laser that can be integrated in a full silicon photonics platform with other active components such as modulators and detectors. Using the fabrication experience developed with the erbium-doped lasers, thulium was investigated as a dopant ion for gain at longer wavelengths. The thulium-doped aluminum oxide required material characterization as it was being studied for the first time. Dopant concentration, absorption cross-sections, and lifetime were characterized. More generally, a new method was developed for characterizing the full transfer function of solid state gain media. Magnitude and phase responses were identified for erbium- and thulium-doped fibers, verifying the validity of the newly developed frequency-domain method. The same method can also be used in measuring other systems that exhibit low-pass behavior such as experiments used in measuring minority carrier lifetimes.

For on-chip coherent communications, linewidths on the order of 1 MHz are sufficient due to the short propagation distances required. However, for applications in long-haul communications, or various synthesis systems where frequency stability is key, linewidths wider than MHz levels are not suitable. Although rare-earths provide narrower-band lasing signals than those commonly achieved with semiconductors, an on-chip frequency stabilization system still had to be implemented. Typically, stabilization in free space is achieved by using an ultra-low expansion glass resonator with quality factors of over 10^{10}. Similar on-chip quality factor performance is currently not possible due to internal loss in microcavities. However, thermal stability can still be addressed without having to build resonators with extremely high quality factors. It was shown that typical SiN ring resonators are thermally limited in their noise performance. In order to address the thermal fluctuations, materials with opposite signs of thermo-optic coefficients were used. Titanium dioxide was utilized as the negative thermo-optic coefficient material due to its CMOS-compatibility. A resonator was created with just the right design that allowed for the resonances in the C-band to be athermal within 5-10 degree temperature ranges. On either side of the athermal operation region, thermal shifts were reduced by more than 200 times when compared with the typical shifts observed in Si resonators. Then, a benchtop laser with typical MHz-level linewidth was locked to the athermal resonator using the Pound-Drever-Hall technique. Frequency stability of the locked laser was measured by beating it with a comb reference whose repetition rate and carrier envelope offset were stabilized. Results showed a linewidth narrowing by a factor of almost 13 times, with single side band phase noise improvements of over 25 dB at 1 MHz offset from the CW lasing frequency. This was an important step towards a full integrated stabilization loop that can take an integrated erbium-based CW laser, stabilize it to an also integrated athermal cavity, and output the stable light for use in frequency-sensitive applications like RF or optical synthesis.

The second half of the thesis focused on development of technologies that can be immediately implemented with existing CMOS capabilities without needing new materials. One of the missing functionalities in the silicon photonics platform was identified in the area of optical filters. Although many wavelength division multiplexing systems existed, none of the current solutions provided broadband response with sharp filter roll-offs that one expects form ideal filters. With such limitations in mind, a new waveguide cross-section was designed to confine different wavelengths of light into different spatial regions. Analysis of the newly invented spectrally-selective waveguides was performed using coupled mode theory where power in each waveguide was solved for as a function of the propagation constants. We then used the spectrally-selective waveguide idea to design an on-chip, 1x2 dichroic filter that works just like free-space dichroic filters, but in transmission. In other words, the transmissive dichroic filter can direct inputs at all wavelengths to respective output ports without reflecting onto the same waveguide unlike a Bragg filter that works using interferometric principles. Filters were fabricated in a standard CMOS process. The experimental results showed that the filters functioned as intended, and the sharpest roll-offs achieved to date were recorded (~2.8 dB/nm). With broadband responses, the fabricated filters became the first examples of dichroic filters on-chip, and established the general theory and approach for spectrally selective waveguides.

For applications where an extremely large transmission bandwidth is required, but the device footprint has to remain small, directional coupler based approaches were studied. By utilizing several ideas developed previously, a coupler was designed to operate as a wavelength splitter. We made use of the fact that the 100 % coupling length in a directional coupler is significantly different for wavelengths separated by an octave. We then designed a broadband 50/50 coupler at 1f, that simply acted as a straight waveguide at 2f due to the tightly confined mode. By cascading two of these 50/50 couplers, we created an extremely broadband 1f/2f wavelength splitter within an approximately 20 μm by 100 μm footprint. These couplers of course are not expected to provide sharp roll-offs as the spectrally selective waveguides. However, in applications where ultra-wide bandwidths and small footprints are required, such devices can be utilized.

Overall, contributions in the light generation and stabilization areas can be combined with the ultra-wideband and ultra-sharp filters demonstrated here. Resulting systems with light generation and efficient multiplexing/routing technologies can be used in filter arrays, switch networks, display systems, and sensors. As the amount of data we process and need grows every day, photonic communication and computation systems that can utilize such devices will be the driving force behind innovation.

8 APPENDICES

APPENDIX A: PRISM COUPLING TECHNIQUE

Prism coupling is a convenient technique for determining the thickness and refractive index of thin films by making use of the guided modes in the material. It was pioneered by Tien and Ulrich in the 1970s [117-119]. The information found here pertains specifically to the Metricon 2010/M prism coupler, but the basic ideas are the same for all prism couplers. More details about this specific coupler can be found in the user manual [120].

The operation principle is illustrated below in Figure 8-1. Here, the film is brought in contact with a prism with the use of a coupling head. The assembly is placed on a rotating table that rotates around the vertical axis going through the prism. In general, the incident light reflects from the prism-air interface due to total internal reflection. However, as the angle of incidence varies, at certain angles, incident light couples into the guided modes of the film, causing sharp drops in the intensity recorded at the photodetector placed behind the prism. This intensity is plotted with respect to the prism angle where the film coupling angles depend on the thickness and the refractive index of the film measured. As a result, each pair of modes can be used to calculate the index and thickness. For more than two modes, the calculation is repeated with each available pair of modes, and yields a confidence interval.

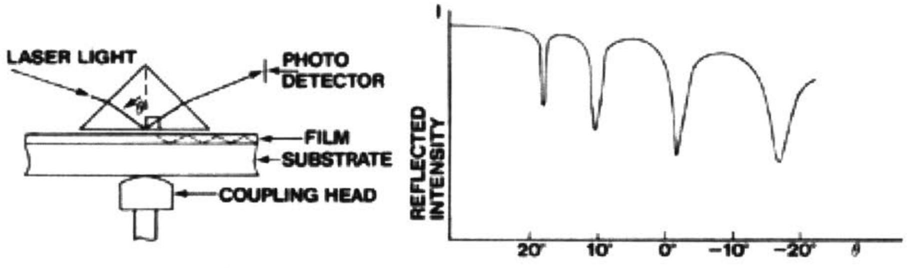

Figure 8-1: Basics of the prism coupling technique with reflected intensity changing as a function of laser incidence angle, reproduced from [120], also available at metricon.com

A photo of the laser beam propagating in the film is given in Figure 8-2. For films with propagation losses less than 15-20 dB/cm, the continuous streak of light is clearly observed as the mode travels in the slab waveguide formed by the film. This is usually easier to see for films placed on substrates with smaller refractive indices, hence forming the slab waveguide. The streak of scattered light can then be used to measure the propagation loss in the film. A fiber is mounted on a motorized stage, and is placed at normal angle to the propagating mode. This fiber stage slowly moves in the propagation direction and records the measured intensity as a function of position. The resulting dataset is then analyzed with an exponential fit to determine the power loss per unit length in the slab mode. When measuring the scattered light intensity, it is crucial to subtract any intensity from background lighting. This is achieved by adjusting the reading offset so that the reading stays just above zero when the laser is turned off.

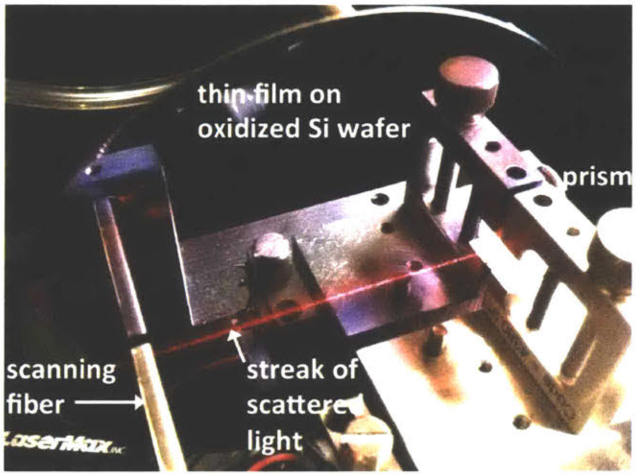

Figure 8-2: Prism coupler with a 632 nm laser beam coupled to the fundamental TE guided mode in an Al_2O_3 thin film

Next, we look at two example measurements: In Figure 8-3, the intensity read by the moving fiber is plotted against the propagation distance. The measured intensity and the resulting fit follow a clear exponential decay. In this case, the propagation loss is easily and confidently determined.

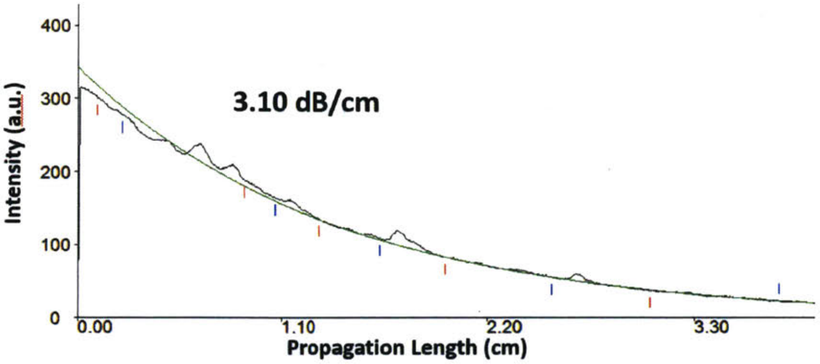

Figure 8-3: Example prism coupling loss measurement with a clear exponential decay and a well-matched exponential fit yielding 3.10 dB/cm loss

On the other hand, when films have very low loss (less than 0.4-0.5 dB/cm), the measured intensity becomes much harder to interpret. In this case, most surface scatterers dominate the intensity plot, as seen in Figure 8-4. The decaying line is masked by the peaks, and cannot be accurately identified. Such measurements are observed for films with less than 0.1 dB/cm loss, as most films with 0.2-0.3 dB/cm can still be characterized. When the propagation intensity data looks like the example in Figure 8-4, one can then conclude that the loss in the film is lower than what can be confidently characterized with this equipment. One important point here is to make sure that the light is actually coupled into the film by turning the laser off, and making sure that the recorded intensity goes to zero.

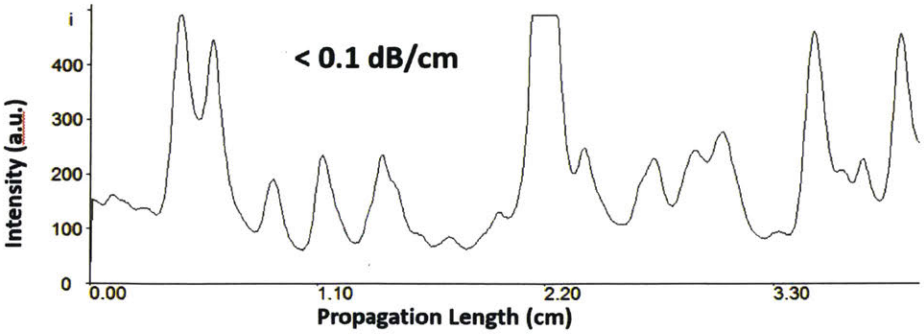

Figure 8-4: Another example prism coupling measurement from a film with much lower propagation loss. The predicted loss is less than the minimum loss of approximately 0.1 dB/cm that can be measured with the instrument

APPENDIX B: SPECTRAL SIMULATIONS IN COUPLED MODE THEORY

Most designs in integrated photonics have to satisfy various bandwidth requirements around a central operation wavelength. Typically, designers first design the structure at the desired central wavelength using eigenmode solutions, coupled mode theory, or other semi-analytical methods. Only then, more advanced numerical simulations such as FDTD are performed to evaluate the response of the designed structure to a broadband pulse. Spectral bandwidth is then determined from these FDTD simulations.

Although FDTD is extremely powerful, it can sometimes be the slowest step in the design process. Hours and days spent waiting for simulations to finish can be used for doing more valuable design or analysis tasks. It is therefore convenient to incorporate some wavelength-dependent parameters into the conventional single wavelength design flow. This can be possible if the effective index of a waveguide with a given geometry can be somehow calculated without having to run simulations at each wavelength. The solution, although not as elegant as one might like, lies in constructing a lookup table or an empirical description (like a polynomial fit) of the effective index as a function of variables such as waveguide width, height, and wavelength.

Here, instead of having a variable height, this procedure is performed for two families of waveguides. Heights of 220 nm and 380 nm were assumed for applications at telecom wavelengths and other longer wavelength or mid-IR applications respectively. (The longer wavelength standard is forming around 380-400 nm, so the choice here is natural.) For each waveguide, we use Lumerical MODE Solutions to solve for the first two guided modes' effective indices as a function of wavelength. It is important to mention that the two modes with the highest effective indices in both cases are the fundamental TE and TM modes, even with the widest widths used. Each wavelength sweep is performed for the following lists of widths:

- 220 nm tall Si waveguide: $\lambda = 1.15\text{-}1.85$ μm; 0.350-0.550 μm widths
- 380 nm tall Si waveguide: $\lambda = 2.00\text{-}2.70$ μm; 0.525-0.775 μm widths

Resulting effective indices are empirically fit using polynomials, according to the equation

$$n(\lambda, w) = n_0 + p_{10}w + p_{01}\lambda + p_{20}w^2 + p_{11}w\lambda + p_{02}\lambda^2 \tag{8.1}$$

It is of course possible to use polynomials of higher order for more accurate fits. However, at that point, it is probably more convenient to save the fit as an interpolation or a table that MATLAB can look up from. Such a lookup table can expedite many design tasks, especially those requiring use of waveguides with different widths, or various tolerance analyses.

For the two types of waveguides mentioned above, the coefficients are given in Table 8-1 and Table 8-2 assuming units of μm for both the waveguide width and wavelength. All modes have been solved with Lumerical's MODE using a maximum discretization of 10 nm, and metal boundaries.

220 nm tall waveguide		
Coefficient	TE Mode Value	TM Mode Value
n_0	3.839193677620065	6.158188704144765
p_{10} (μm^{-1})	3.703245512405442	3.120885494418312
p_{01} (μm^{-1})	-2.381885992576637	-5.614133495493068
p_{20} (μm^{-2})	-5.787801833049692	-1.433603273793527
p_{11} (μm^{-1})	2.388779048956228	-0.726798999163976
p_{02} (μm^{-2})	0.017628731650978	1.532487578196586

Table 8-1: Coefficients for 2nd order polynomial fit to effective indices in a 220 nm-tall Si waveguide (standard for most CMOS processes)

380 nm tall waveguide		
Coefficient	TE Mode	TM Mode
n_0	3.278710820590256	5.510187085678632
p_{10} (μm^{-1})	3.054300882726142	2.430401971164335
p_{01} (μm^{-1})	-1.280236259139003	-3.006957511123038
p_{20} (μm^{-2})	-3.372095445363865	-0.826780308246657
p_{11} (μm^{-1})	1.271491011560636	-0.295018161602444
p_{02} (μm^{-2})	-0.072941200655685	0.484127392526984

Table 8-2: Coefficients for 2nd order polynomial fit to effective indices in a 380 nm-tall Si waveguide (becoming more common for mid-IR or longer wavelength devices)

Similarly, it is also useful to work out the polynomial coefficients for a pair of symmetric, coupled waveguides using the standard 220 nm and 380 nm layer heights. Here, instead of varying the width, we change the gap between the two coupled waveguides while keeping waveguide widths constant. The following parameters are used for the waveguide pairs:

- 220 nm tall Si waveguide pair: λ = 1.15-1.85 μm; 0.450 μm constant width; 0.100-0.550 μm gaps
- 380 nm tall Si waveguide pair: λ = 2.00-2.70 μm; 0.650 μm constant width; 0.200-0.650 μm gaps

Then, the following 2nd order polynomial fit is applied to estimate the effective indices of the even and odd supermodes as a function of gap and wavelength:

$$n(\lambda, w) = n_0 + p_{10}g + p_{01}\lambda + p_{20}g^2 + p_{11}g\lambda + p_{02}\lambda^2 \qquad (8.2)$$

Results are given in Table 8-3 and Table 8-4. Note that in all cases, both the even and odd supermode are quasi-TE.

220 nm tall waveguide pair		
Coefficient	Even Supermode	Odd Supermode
n_0	4.241001015443410	4.090384350903875
p_{10} (μm^{-1})	0.171067109901610	-0.136790891383538
p_{01} (μm^{-1})	-1.261774314827927	-0.935342513928238
p_{20} (μm^{-2})	0.307490203053179	-0.132706519613238
p_{11} (μm^{-1})	-0.307349963814832	0.186199702853994
p_{02} (μm^{-2})	0.059307251544209	-0.136724393032963

Table 8-3: Coefficients for 2nd order polynomial fit to effective indices of even and odd supermodes in a pair of symmetric, 220 nm-tall, 450 nm-wide Si waveguides

380 nm tall waveguide pair		
Coefficient	Even Supermode	Odd Supermode
n_0	3.828131260876320	3.563946305640901
p_{10} (μm^{-1})	0.208691415497634	-0.144695957611208
p_{01} (μm^{-1})	-0.517394888415840	-0.179699559258982
p_{20} (μm^{-2})	0.287071802467296	-0.102955784004880
p_{11} (μm^{-1})	-0.228846933714607	0.121118523414583
p_{02} (μm^{-2})	-0.026260171892248	-0.148421849559391

Table 8-4: Coefficients for 2nd order polynomial fit to effective indices of even and odd supermodes in a pair of symmetric, 380 nm-tall, 650 nm-wide Si waveguides

APPENDIX C: DIRECTIONAL COUPLER PARAMETER DESIGN VIA TRANSFER MATRIX

Since most couplers use some type of cosine or S-bends to bring waveguides closer and farther, it is important to include the effects of these bends in the simulations. If neglected, the coupling in the bends can shift responses out of specifications, especially for devices where the required coupling is just a few percent. Given below is a generic Mathematica script that can be used to cascade transfer matrices of the form given in equation (6.1). Here, S and M can be cascaded as required, and the appropriate lengths for satisfying some κL product can be easily solved. Mathematica is advantageous here in that it can multiply all the transfer matrices first, and then solve for the required variables afterwards. This is much more difficult to do in MATLAB and would have taken much longer due to limited symbolic capability.

Input Parameters: A (amount of power coupled in the input and output S-bends, comes from separate FDTD simulation), Q (desired coupled power after the whole coupler with the bends and the coupling section)

```
ClearAll["Global`*"]

(*2 S-bend sections only*)
S = {{ts, -I*qs}, {-I*qs, ts}};
mySsol =
 NSolve[Abs[S.S.{1, 0}]^2 == {1 - A, A} && A == 0.048205 && qs > 0 && ts > 0 && ts > qs]
ts = ts /. mySsol[[1]];
NumberForm[ts, 12]
qs = qs /. mySsol[[1]];
NumberForm[qs, 12]

(*S-bend/coupler/S-bend*)
M = {{tc, -I*qc}, {-I*qc, tc}};
myDCsol = NSolve[Abs[S.M.S.{1, 0}]^2 == {1 - Q, Q} && Q == 1 && qc > 0 && tc > 0]
tc = tc /. myDCsol[[1]]
qc = qc /. myDCsol[[1]]

(*find the angle for Lc *)
myAngle = NSolve[Cos[ϕ] == tc]
ϕ = ϕ /. myAngle[[2]]
```

Here, t_S and t_C are the transmitted amplitude coefficients for the S-bends and the coupler respectively. It is important to specify that both $t_S > 0$ and $t_C > 0$, and that $t_C > t_S$. Otherwise, Mathematica will output multiple solutions among which it can be difficult to identify which one corresponds to the real physical phenomena.

After this script is evaluated, one can then check what happens in case of cascading a number of these couplers. This can be evaluated by a few lines like

```
(*check 2 DCs together*)
S.M.S.S.M.S.{1, 0};
Abs[S.M.S.S.M.S.{1, 0}]^2
```

where we cascaded two directional couplers with S bends on either side, and used only the top port as the input. Since the matrices can be easily replaced, this script provides a convenient way to evaluate coupler parameters. Moreover, as the amplitude coefficients are symbolically multiplied, and only numerically solved at the final stage, the solutions are much more accurate than what can be obtained using only numerical simulations where one would most likely have to look for intercepts between curves.

APPENDIX D: STANDARD OPERATION PROCEDURE FOR KJL SPUTTER TOOL

Given below is the standard procedure to start a deposition on the KJL sputter tool. This should be used as a first reference when interacting with the tool:

1. Clean the samples using IPA and acetone.
2. Fix samples on the back of a blank Si wafer using the silver paste. Only use a small amount of paste. Do not press the samples all the way since they will be impossible to detach afterwards.
3. Bake on the hotplate at 250C for 2 hours.
4. Vent the loadlock using the "Vent LL" button.
5. Physically load the samples, i.e. place the wafer upside down inside the wafer holder in the loadlock.
6. Close the loadlock cover and use "Pump LL" to pump the loadlock.
7. Once the pressure reaches below 1e-5 in the loadlock, use "Load Samples" to transfer the wafer from the loaclock into the process chamber.
8. Make sure the turbo pump speed setpoint is at 100 %, and the gate valve is open.
9. Engage "PC Turbo High Vac Throttle". This partially closes the gate valve and allows for much easier pressure control.
10. Start substrate rotation by clicking "Drive Motor Continuous Fwd" button in the "Platen Motion" tab.
11. Start the substrate heater by turning on the On/Off switch in the Heating tab.
12. Give the desired setpoint in the "SP deg C" field.
13. Start the temperature ramp by clicking "Auto" next to the substrate heater on/off switch.
14. Wait for the temperature to reach the desired value. This will take 10C/min, as set by the ramp rate.
15. You may reduce the temperature ramp rate as desired, but 10C/min is max.
16. Outgas at the deposition temperature for 2 hours by simply waiting with the substrate rotation turned on. This will reduce the pressure in the chamber and eliminate potential contaminant gases introduced by loading a new set of samples.

17. Open all gas valves: “Source 3 Gas”, “MFC1 Iso valve”, and “MFC2 Iso valve”.
18. Open “Gas Injection” valve.
19. Make sure the “Ion Source Program Number” is set to 2 in the deposition tab. This is the idle setting with minimum flow (0.1 sccm).
20. Turn on “Ion Source Power Supply”
21. Set Ion Source Program Number to 3 (this gives 10 sccm)
22. More Ar flow is required: Set the Capman pressure setpoint to 11 mT, and the MFC1 flow mode to 4. This will introduce Ar gas and keep the pressure at the setpoint.
23. Ar flow should stabilize to around 65 sccm.
24. Wait for the pressure to stabilize in the chamber (~1 min).
25. Open the cover, and check behind the monitor to make sure all power supplies and matching networks are turned on.
26. For Al, set Power Supply 2 setpoint as 50 W, but do not turn it on yet.
27. Open Shutter 2 before attempting to start plasma.
28. Turn on Power Supply 2, and watch the forward power go up to ~50 W.
29. Reflected power should be 0 or 1 W.
30. DC bias should be around 45 V.
31. If plasma doesn’t start, turn off the power supply, and repeat the last 6 steps.
32. Start plasma on any other gun using the same procedure.
33. Switch to the deposition pressure by changing Capman pressure setpoint to 5 mT.
34. Wait for the pressure to stabilize.
35. Ramp the power supplies one by one to the desired power: Click “Ramp”. Set 5 or 10 V/s, and then give it a new setpoint. The gun will ramp to the setpoint with the specified rate. After the ramp is complete, the “Ramp” field will go to zero.
36. Presputter for 5 min on the back of the substrate shutter.
37. Set the reactive gas flow using MFC2 setpoint. If this is the first time determining the proper reactive gas flow rate, start around 0.5 sccm. Go up in increments of 0.1 or 0.2 sccm, and observe the bias voltage on the target for 1-2 min. It is important to wait this amount of time because the bias usually doesn’t immediately drop. So if the reactive gas flow is just slightly over the “knee”, it might drop the bias 10 min into deposition, and it is important to know that before starting the run.

38. Adjust the reactive gas flow during deposition if necessary to keep the target voltage bias at the “knee” point.
39. Open the substrate shutter to start deposition. The target shutters should already be open at this point, since you don’t close them after igniting plasma.
40. Wait for amount of time required for the deposition to complete.
41. Close the substrate shutter.
42. Traverse through the rest of the steps in the reverse order to finish deposition.

9 LIST OF PUBLICATIONS

Invited Talks

[1] E. S. Magden, C.V. Poulton, N. Li, D. Vermeulen, A. Ruocco, N. Singh, G. Leake, D. Coolbaugh, L.A. Kolodziejski, M.R. Watts, "Integrated, Mode-Evolution Based Dichroic Filter with 2.5 dB/nm Rolloff for Silicon Photonics", OSA Nanophotonics Technical Group 20x20 Talks, Lasers and Electro-Optics (CLEO), 2017 Conference on.

Journal Articles

[13] E. S. Magden, P.T. Callahan, N. Li, K. Shtyrkova, A. Ruocco, N. Singh, D. Vermeulen, J.D.B. Bradley, L.A. Kolodziejski, F.X. Kaertner, E.P. Ippen, M.R. Watts, "Spontaneous Emission Lifetime Characterization in Rare-Earth-Doped Gain Media via Frequency-Domain Analysis" in preparation, Applied Physics Letters (2017).

[12] E. S. Magden, M. Peng, N. Li, Purnawirman, G. Leake, D. Coolbaugh, E.P. Ippen, F.X. Kaertner, M. R. Watts, and L.A. Kolodziejski, "Laser frequency stabilization and phase noise enhancement using pound-drever-hall technique with an integrated TiO_2 athermal resonator." in preparation, Optics Letters (2017).

[11] E. S. Magden, N. Li, A. Ruocco, N. Singh, C.V. Poulton, D. Vermeulen, E.P. Ippen, L.A. Kolodziejski, M.R. Watts, " Integrated, Transmissive Dichroic Filters Based on Mode-Evolution Coupler" submitted to Nature Communications (2017).

[10] N. Li, G. Singh, E. S. Magden, Z. Su, N. Singh, M. Moresco, G. Leake, J. D. B. Bradley, M. Watts, “Reliable Integrated Photonic Light Sources Using Curved $Al_2O_3:Er^{3+}$ Distributed Feedback Lasers”. IEEE Photonics Journal, 9(4), pp.1-9 (2017).

[9] E. S. Magden, Purnawirman, N. Li, J. D. B. Bradley, G. Petrich, G. Leake, D.

Coolbaugh, E.P. Ippen, M. R. Watts, and L.A. Kolodziejski, "Monolithically-integrated distributed feedback laser compatible with CMOS processing." Optics Express 25.15 (2017): 18058-18065.

[8] Purnawirman, N. Li, E. S. Magden, G. Singh, A. Baldycheva, E. S. Hosseini, J. Sun, M. Moresco, T. N. Adam, G. Leake, D. Coolbaugh, J. Bradley, M. R. Watts, "Ultra-narrow-linewidth $Al_2O_3:Er^{3+}$ lasers with a wavelength-insensitive waveguide design on a wafer-scale silicon nitride platform", Optics Express 25.12 (2017): 13705-13713.

[7] N. Li, Z. Su, Z. Su, E. S. Magden, C. V. Poulton, A. Ruocco, N. Singh, M. J. Byrd, J. Bradley, G. Leake, and M. R. Watts, "Athermal Synchronization of Laser Source with WDM Filter in a Silicon Photonic Platform," Applied Physics Letters 110.21 (2017): 211105.

[6] Purnawirman, N. Li, E. S. Magden, G. Singh, M. Moresco, T. N. Adam, G. Leake, D. Coolbaugh, J. Bradley, M. R. Watts, "Wavelength division multiplexed light source monolithically integrated on a silicon photonics platform." Optics Letters 42.9 (2017): 1772-1775.

[5] N. Li, Purnawirman, Z. Su, E. S. Magden, P. T. Callahan, K. Shtyrkova, M. Xin, A. Ruocco, C. Baiocco, E. P. Ippen, F. X. Kaertner, J. D. B. Bradley, D. Vermeulen, and M. R. Watts, "High-power Thulium Lasers on a Silicon Photonics Platform," Optics Letters 42, 1181-1184 (2017).

[4] N. Li, E. Timurdogan, C. V. Poulton, M. Byrd, E. S. Magden, Z. Su, G. Leake, D. D. Coolbaugh, D. Vermeulen, and M. R. Watts, "C-band swept wavelength erbium-doped fiber laser with a high-Q tunable interior-ridge silicon microring cavity," Optics express 24, 22741-22748 (2016).

[3] Z. Su, N. Li, E. S. Magden, M. Byrd, T. N. Adam, G. Leake, D. Coolbaugh, J. D. Bradley, and M. R. Watts, "Ultra-compact and low-threshold thulium microcavity laser monolithically integrated on silicon," Optics Letters 41, 5708-5711 (2016).

[2] G. Singh, J. Bradley, N. Li, E. S. Magden, M. Moresco, T. Adam, G. Leake, D. Coolbaugh, and M. Watts, "Resonant pumped erbium-doped waveguide lasers using distributed Bragg reflector cavities," Optics letters 41, 1189-1192 (2016).

[1] D. DeMeo, C. Shemelya, C. Downs, A. Licht, E. S. Magden, T. Rotter, C. Dhital, S. Wilson, G. Balakrishnan, and T. E. Vandervelde, "GaSb Thermophotovoltaic Cells Grown on GaAs Substrate Using the Interfacial Misfit Array Method," Journal of electronic materials 43, 902 (2014).

Conference Presentations

[17] N. Li, Purnawirman, G. Singh, E. S. Magden, M. Moresco, T. Adam, G. Leake, D. Coolbaugh, J. D. B. Bradley, M. Watts, “Reliable Silicon Photonic Light Source Using

Curved Distributed Feedback Lasers". in Integrated Photonics Research, Silicon and Nanophotonics, 2017 (pp. ITu2A-5). Optical Society of America.

[16] E. S. Magden, P.T. Callahan, N. Li, K. Shtyrkova, A. Ruocco, N. Singh, M. Xin, D. Vermeulen, J.D.B. Bradley, G. Leake, D. Coolbaugh, L.A. Kolodziejski, F.X. Kaertner, E.P. Ippen, M.R. Watts "Frequency-Domain Measurement of Spontaneous Emission Lifetime in Rare-Earth-Doped Gain Media." Lasers and Electro-Optics (CLEO), 2017 (pp. SM1K.3), Optical Society of America.

[15] P.T. Callahan, K. Shtyrkova, N. Li, E. S. Magden, Purnawirman, C. Baiocco, D. Coolbaugh, E.P. Ippen, M.R. Watts, F.X. Kaertner, "Fully-Integrated CMOS-Compatible Q-Switched Laser at 1.9μm Using Thulium-Doped Al_2O_3" Lasers and Electro-Optics (CLEO), 2017 Conference on, (pp. STh3N.2), Optical Society of America.

[14] N. Singh, M. Xin, D. Vermeulen, K. Shtyrkova, E. S. Magden, P.T. Callahan, N. Li, A. Ruocco, G. Leake, D. Coolbaugh, E. P. Ippen, F.X. Kaertner, M.R. Watts "Octave spanning supercontinuum generation in silicon from 1.1 μm to beyond 2.4 μm." Lasers and Electro-Optics (CLEO), 2017 Conference on, (pp. Stu4J.7), Optical Society of America.

[13] E. S. Magden, C.V. Poulton, N. Li, D. Vermeulen, A. Ruocco, N. Singh, G. Leake, D. Coolbaugh, L.A. Kolodziejski, M.R. Watts, "Mode-Evolution-Based, Broadband 1x2 Port High-Pass/Low-Pass Filter for Silicon Photonics" In Optical Fiber Communication Conference 2017 (pp. Th1G.2). Optical Society of America.

[12] J. D. Bradley, Z. Su, E. S. Magden, N. Li, M. Byrd, P. Purnawirman, T. N. Adam, G. Leake, D. Coolbaugh, and M. R. Watts, "1.8-μm thulium microlasers integrated on silicon," in SPIE OPTO, (International Society for Optics and Photonics, 2016), 97440U-97440U-97446.

[11] Z. Su, J. Bradley, N. Li, E. S. Magden, P. Purnawirman, D. Coleman, N. Fahrenkopf, C. Baiocco, T. Adam, and G. Leake, "Ultra-Compact CMOS-Compatible Ytterbium Microlaser," in Integrated Photonics Research, Silicon and Nanophotonics, (Optical Society of America, 2016), IW1A. 3.

[10] E. S. Magden, N. Li, G. Singh, J. D. Bradley, G. S. Petrich, G. Leake, D. D. Coolbaugh, M. R. Watts, and L. A. Kolodziejski, "Fully CMOS-compatible integrated distributed feedback laser with 250° C fabricated $Al_2O_3:Er^{3+}$ gain medium," in Lasers and Electro-Optics (CLEO), 2016 Conference on, (IEEE, 2016), 1-2.

[9] E. S. Magden, M. Y. Peng, J. D. Bradley, G. Leake, D. D. Coolbaugh, L. A. Kolodziejski, F. X. Kärtner, and M. R. Watts, "Laser frequency stabilization using pound-drever-hall technique with an integrated TiO 2 athermal resonator," in Lasers and Electro-Optics (CLEO), 2016 Conference on, (IEEE, 2016), 1-2.

[8] J. D. Bradley, P. Purnawirman, E. S. Hosseini, Z. Su, E. S. Magden, N. Li, G. Singh, J. Sun, T. N. Adam, and G. Leake, "(Invited) On-Chip and Silicon-Compatible Er-Doped Aluminum Oxide Lasers," in Meeting Abstracts, (The Electrochemical Society, 2016), 2114-2114.

[7] N. Li, Z. Su, E. S. Magden, P. T. Callahan, K. Shtyrkova, M. Xin, A. Ruocco, N. Fahrenkopf, C. Baiocco, and G. Leake, "High-power CMOS-compatible photonic integrated thulium-doped distributed feedback laser," in Photonics Conference (IPC), 2016 IEEE, (IEEE, 2016), 702-703.

[6] N. Li, J. D. Bradley, G. Singh, E. S. Magden, J. Sun, and M. R. Watts, "Self-pulsing in Erbium-doped fiber laser," in Optoelectronics Global Conference (OGC), 2015, (IEEE, 2015), 1-2.

[5] C. M. Sorace-Agaskar, P. T. Callahan, K. Shtyrkova, A. Baldycheva, M. Moresco, J. Bradley, M. Y. Peng, N. Li, E. S. Magden, and P. Purnawirman, "Integrated mode-locked lasers in a CMOS-compatible silicon photonic platform," in CLEO: Science and Innovations, (Optical Society of America, 2015), SM2I.5.

[4] Z. Su, J. Bradley, E. S. Hosseini, A. Baldycheva, G. Singh, E. S. Magden, T. Adam, G. Leake, D. Coolbaugh, and M. Watts, "Compact Rare-Earth-Doped Microring Lasers Monolithically Integrated on Silicon Chips," in The European Conference on Lasers and Electro-Optics, (Optical Society of America, 2015), CK_12_2.

[3] E. S. Magden, V. Minden, C. Shemelya, and T. Vandervelde, "Micro-Photoluminescence for Optoelectronic Material Characterization," in APS Meeting Abstracts, 2012)

[2] H. Chen, E. S. Magden, C. Downs, and T. Vandervelde, "Efficiency Analysis and Demonstration of Split-Junction Photovoltaic Solar Cells," in APS Meeting Abstracts, 2012)

[1] E. S. Magden, H. Chen, C. Downs, and T. E. Vandervelde, "3+ 1 multijunction testing and operations platform for improved PV and TPV efficiencies," in Innovative Technologies for an Efficient and Reliable Electricity Supply (CITRES), 2010 IEEE Conference on, (IEEE, 2010), 116-120.

10 REFERENCES

1. Yaacobi, A., et al., *Integrated phased array for wide-angle beam steering.* Optics letters, 2014. **39**(15): p. 4575-4578.
2. Biberman, A., et al., *Ultralow-loss silicon ring resonators.* Optics letters, 2012. **37**(20): p. 4236-4238.
3. Sun, J., et al., *Large-scale nanophotonic phased array.* Nature, 2013. **493**(7431): p. 195-199.
4. Watts, M.R., et al. *Towards integrated polarization diversity: design, fabrication and characterization of integrated polarization splitters and rotators.* in *Optical Fiber Communication Conference.* 2005. Optical Society of America.
5. Watts, M.R., et al., *Adiabatic thermo-optic Mach–Zehnder switch.* Optics letters, 2013. **38**(5): p. 733-735.
6. Vermeulen, D., et al., *High-efficiency fiber-to-chip grating couplers realized using an advanced CMOS-compatible silicon-on-insulator platform.* Optics express, 2010. **18**(17): p. 18278-18283.
7. Worhoff, K., et al., *Reliable Low-Cost Fabrication of Low-Loss $\hbox {Al} _ {2}\hbox {O} {3}{:}\hbox {Er}^{3+} $ Waveguides With 5.4-dB Optical Gain.* IEEE Journal of Quantum Electronics, 2009. **45**(5): p. 454-461.
8. Kitagawa, T., et al., *Guided-wave laser based on erbium-doped silica planar lightwave circuit.* Electronics letters, 1991. **27**(4): p. 334-335.
9. Ortiz, A., et al., *Characterization of amorphous aluminum oxide films prepared by the pyrosol process.* Thin Solid Films, 2000. **368**(1): p. 74-79.
10. Palik, E.D., *Handbook of optical constants of solids.* Vol. 3. 1998: Academic press.
11. Miura, K., et al., *Photowritten optical waveguides in various glasses with ultrashort pulse laser.* Applied Physics Letters, 1997. **71**(23): p. 3329-3331.

12. Yan, Y., et al., *Erbium-doped phosphate glass waveguide on silicon with 4.1 dB/cm gain at 1.535 μm.* Applied Physics Letters, 1997. **71**(20): p. 2922-2924.
13. Kurokawa, Y., et al., *Photo-properties of rare earth ion (Er 3+, Eu 3+ and Sm 3+)-doped alumina films prepared by the sol–gel method.* Chemical physics letters, 1998. **287**(5): p. 737-741.
14. Bradley, J.D. and M. Pollnau, *Erbium-doped integrated waveguide amplifiers and lasers.* Laser & Photonics Reviews, 2011. **5**(3): p. 368-403.
15. Soulard, R., et al., *Detailed characterization of pump-induced refractive index changes observed in Nd: YVO 4, Nd: GdVO 4 and Nd: KGW.* Optics express, 2010. **18**(2): p. 1553-1568.
16. Vázquez-Córdova, S.A., et al., *Erbium-doped spiral amplifiers with 20 dB of net gain on silicon.* Optics express, 2014. **22**(21): p. 25993-26004.
17. Li, N., et al., *Athermal synchronization of laser source with WDM filter in a silicon photonics platform.* Applied Physics Letters, 2017. **110**(21): p. 211105.
18. Belt, M. and D.J. Blumenthal. *High temperature operation of an integrated erbium-doped DBR laser on an ultra-low-loss Si 3 N 4 platform.* in *Optical Fiber Communications Conference and Exhibition (OFC), 2015.* 2015. IEEE.
19. Bernhardi, E., et al., *Ultra-narrow-linewidth, single-frequency distributed feedback waveguide laser in Al 2 O 3: Er 3+ on silicon.* Optics Letters, 2010. **35**(14): p. 2394-2396.
20. Zhang, K. and J.U. Kang, *C-band wavelength-swept single-longitudinal-mode erbium-doped fiber ring laser.* Optics express, 2008. **16**(18): p. 14173-14179.
21. Li, N., et al., *Ultra-narrow-linewidth Al 2 O 3: Er 3+ lasers with a wavelength-insensitive waveguide design on a wafer-scale silicon nitride platform.* Optics Express, 2017. **25**(12): p. 13705-13713.
22. Belt, M., et al., *Arrayed narrow linewidth erbium-doped waveguide-distributed feedback lasers on an ultra-low-loss silicon-nitride platform.* Optics letters, 2013. **38**(22): p. 4825-4828.
23. Wong, J.H., et al., *Photonic Generation of Frequency-Tunable Microwave Signals Using an Array of Uniformly Spaced Optical Combs.* Journal of Lightwave Technology, 2012. **30**(19): p. 3164-3172.
24. Li, N., et al., *C-band swept wavelength erbium-doped fiber laser with a high-Q tunable interior-ridge silicon microring cavity.* Optics express, 2016. **24**(20): p. 22741-22748.
25. Song, Y., et al., *40-nm-wide tunable fiber ring laser with single-mode operation using a highly stretchable FBG.* IEEE Photonics Technology Letters, 2001. **13**(11): p. 1167-1169.
26. Li, N., et al., *High-power thulium lasers on a silicon photonics platform.* Optics Letters, 2017. **42**(6): p. 1181-1184.
27. Bradley, J., et al., *Gain bandwidth of 80 nm and 2 dB/cm peak gain in Al 2 O 3: Er 3+ optical amplifiers on silicon.* JOSA B, 2010. **27**(2): p. 187-196.
28. Hosseini, E.S., et al., *CMOS-compatible 75 mW erbium-doped distributed feedback laser.* Optics letters, 2014. **39**(11): p. 3106-3109.

29. Sorace-Agaskar, C.M., et al. *Integrated mode-locked lasers in a CMOS-compatible silicon photonic platform*. in *CLEO: Science and Innovations*. 2015. Optical Society of America.
30. Li, N., et al., *Wavelength division multiplexed light source monolithically integrated on a silicon photonics platform.* Optics Letters, 2017. **42**(9): p. 1772-1775.
31. Franke, A., et al. *Post-CMOS integration of germanium microstructures*. in *Micro Electro Mechanical Systems, 1999. MEMS'99. Twelfth IEEE International Conference on*. 1999. IEEE.
32. Takeuchi, H., et al., *Thermal budget limits of quarter-micrometer foundry CMOS for post-processing MEMS devices.* IEEE transactions on Electron Devices, 2005. **52**(9): p. 2081-2086.
33. Sedky, S., et al., *Experimental determination of the maximum post-process annealing temperature for standard CMOS wafers.* IEEE transactions on Electron Devices, 2001. **48**(2): p. 377-385.
34. Durusoy, H.Z., et al., *Influence of substrate temperature and bias voltage on the optical transmittance of TiN films.* Vacuum, 2003. **70**(1): p. 21-28.
35. Magden, E.S., *Rare-earth doped aluminum oxide lasers for silicon photonics*. 2014, Massachusetts Institute of Technology.
36. Bachari, E., et al., *Structural and optical properties of sputtered ZnO films.* Thin Solid Films, 1999. **348**(1): p. 165-172.
37. Hirata, G., et al., *Luminescence study in Eu-doped aluminum oxide phosphors.* Optical Materials, 2005. **27**(7): p. 1311-1315.
38. Gullapalli, S., et al., *Tungsten oxide (WO 3) thin films for application in advanced energy systems.* Journal of Vacuum Science & Technology A: Vacuum, Surfaces, and Films, 2010. **28**(4): p. 824-828.
39. Fortunato, E., et al., *High mobility amorphous/nanocrystalline indium zinc oxide deposited at room temperature.* Thin Solid Films, 2006. **502**(1): p. 104-107.
40. Singh, G., et al., *Resonant pumped erbium-doped waveguide lasers using distributed Bragg reflector cavities.* Optics letters, 2016. **41**(6): p. 1189-1192.
41. Belt, M. and D.J. Blumenthal, *Erbium-doped waveguide DBR and DFB laser arrays integrated within an ultra-low-loss Si 3 N 4 platform.* Optics express, 2014. **22**(9): p. 10655-10660.
42. Berg, S. and T. Nyberg, *Fundamental understanding and modeling of reactive sputtering processes.* Thin solid films, 2005. **476**(2): p. 215-230.
43. Bradley, J., et al. *1.8-µm thulium microlasers integrated on silicon*. in *Proc. of SPIE Vol.* 2016.
44. Agger, S.D. and J.H. Povlsen, *Emission and absorption cross section of thulium doped silica fibers.* Optics Express, 2006. **14**(1): p. 50-57.
45. Giles, C.R. and E. Desurvire, *Modeling erbium-doped fiber amplifiers.* Journal of lightwave technology, 1991. **9**(2): p. 271-283.
46. Barnard, C., et al., *Analytical model for rare-earth-doped fiber amplifiers and lasers.* IEEE Journal of Quantum Electronics, 1994. **30**(8): p. 1817-1830.

47. Agazzi, L., et al., *Spectroscopy of upper energy levels in an Er 3+-doped amorphous oxide.* JOSA B, 2013. **30**(3): p. 663-677.
48. Peterka, P., et al., *Theoretical modeling of fiber laser at 810 nm based on thulium-doped silica fibers with enhanced 3 H 4 level lifetime.* Optics express, 2011. **19**(3): p. 2773-2781.
49. Rustad, G. and K. Stenersen, *Modeling of laser-pumped Tm and Ho lasers accounting for upconversion and ground-state depletion.* IEEE Journal of Quantum Electronics, 1996. **32**(9): p. 1645-1656.
50. Bao, J., et al., *Controlled modification of erbium lifetime in silicon dioxide with metallic overlayers.* Applied Physics Letters, 2007. **91**(13): p. 131103.
51. Agazzi, L., *Spectroscopic excitation and quenching processes in rare-earth-ion-doped Al 2 O 3 and their impact on amplifier and laser performance.* 2012.
52. Karaveli, S., A.J. Weinstein, and R. Zia, *Direct modulation of lanthanide emission at sub-lifetime scales.* Nano letters, 2013. **13**(5): p. 2264-2269.
53. Zhang, Z., K. Grattan, and A. Palmer, *Fiber-optic high-temperature sensor based on the fluorescence lifetime of alexandrite.* Review of scientific Instruments, 1992. **63**(8): p. 3869-3873.
54. Ma, L., et al., *Singlet fission in rubrene single crystal: direct observation by femtosecond pump–probe spectroscopy.* Physical Chemistry Chemical Physics, 2012. **14**(23): p. 8307-8312.
55. Demas, J., *Excited state lifetime measurements.* 2012: Elsevier.
56. Brunel, M., et al., *Tunable two-frequency lasers for lifetime measurements.* Optical Review, 1997. **4**(5): p. 550-552.
57. Miniscalco, W.J., *Erbium-doped glasses for fiber amplifiers at 1500 nm.* Journal of Lightwave Technology, 1991. **9**(2): p. 234-250.
58. Barnes, W.L., et al., *Absorption and emission cross section of Er/sup 3+/doped silica fibers.* IEEE Journal of Quantum Electronics, 1991. **27**(4): p. 1004-1010.
59. Digonnet, M.J., *Rare-earth-doped fiber lasers and amplifiers, revised and expanded.* 2001: CRC press.
60. Guha, B., J. Cardenas, and M. Lipson, *Athermal silicon microring resonators with titanium oxide cladding.* Optics express, 2013. **21**(22): p. 26557-26563.
61. Watts, M.R., et al. *Adiabatic resonant microrings (ARMs) with directly integrated thermal microphotonics.* in *Lasers and Electro-Optics, 2009 and 2009 Conference on Quantum electronics and Laser Science Conference. CLEO/QELS 2009. Conference on.* 2009. IEEE.
62. Cocorullo, G. and I. Rendina, *Thermo-optical modulation at 1.5 mu m in silicon etalon.* Electronics Letters, 1992. **28**(1): p. 83-85.
63. Okada, Y. and Y. Tokumaru, *Precise determination of lattice parameter and thermal expansion coefficient of silicon between 300 and 1500 K.* Journal of applied physics, 1984. **56**(2): p. 314-320.

64. Arbabi, A. and L.L. Goddard, *Measurements of the refractive indices and thermo-optic coefficients of Si 3 N 4 and SiO x using microring resonances.* Optics letters, 2013. **38**(19): p. 3878-3881.
65. Qiu, F., A.M. Spring, and S. Yokoyama, *Athermal and High-Q Hybrid TiO2–Si3N4 Ring Resonator via an Etching-Free Fabrication Technique.* ACS Photonics, 2015. **2**(3): p. 405-409.
66. Retajczyk, T. and A. Sinha, *Elastic stiffness and thermal expansion coefficients of various refractory silicides and silicon nitride films.* Thin Solid Films, 1980. **70**(2): p. 241-247.
67. Materials, A. *Silica - Silicon Dioxide (SiO2).* 2001 [cited 2017 8-5-2017]; Available from: https://www.azom.com/properties.aspx?ArticleID=1114.
68. Wiechmann, S. and J. Müller, *Thermo-optic properties of TiO 2, Ta 2 O 5 and Al 2 O 3 thin films for integrated optics on silicon.* Thin solid films, 2009. **517**(24): p. 6847-6849.
69. Accuratus. *Aluminum Oxide, Al2O3 Ceramic Properties.* [cited 2017 8-6-2017]; Available from: http://accuratus.com/alumox.html.
70. Materials, A. *Titanium Dioxide - Titania (TiO2).* 2013 [cited 2017; Available from: https://www.azom.com/article.aspx?ArticleID=8521.
71. Teng, J., et al., *Athermal Silicon-on-insulator ring resonators by overlaying a polymer cladding on narrowed waveguides.* Optics express, 2009. **17**(17): p. 14627-14633.
72. Zhang, Z., et al., *Thermo-optic coefficients of polymers for optical waveguide applications.* Polymer, 2006. **47**(14): p. 4893-4896.
73. Schawlow, A.L. and C.H. Townes, *Infrared and optical masers.* Physical Review, 1958. **112**(6): p. 1940.
74. Lax, M., *Classical noise. V. Noise in self-sustained oscillators.* Physical Review, 1967. **160**(2): p. 290.
75. Numata, K., A. Kemery, and J. Camp, *Thermal-noise limit in the frequency stabilization of lasers with rigid cavities.* Physical review letters, 2004. **93**(25): p. 250602.
76. Drever, R., et al., *Laser phase and frequency stabilization using an optical resonator.* Applied Physics B, 1983. **31**(2): p. 97-105.
77. Black, E.D., *An introduction to Pound–Drever–Hall laser frequency stabilization.* American Journal of Physics, 2001. **69**(1): p. 79-87.
78. Black, E., *Notes on pound-drever-hall technique.* LIGO Technical notes, 1998.
79. Cygan, A., et al., *Pound-Drever-Hall-locked, frequency-stabilized cavity ring-down spectrometer.* Review of Scientific Instruments, 2011. **82**(6): p. 063107.
80. Wójtewicz, S., et al., *Line-shape study of self-broadened O 2 transitions measured by Pound-Drever-Hall-locked frequency-stabilized cavity ring-down spectroscopy.* Physical Review A, 2011. **84**(3): p. 032511.
81. Gatti, D., et al., *Fiber strain sensor based on a π-phase-shifted Bragg grating and the Pound-Drever-Hall technique.* Optics express, 2008. **16**(3): p. 1945-1950.
82. Liu, Q., T. Tokunaga, and Z. He, *Ultra-high-resolution large-dynamic-range optical fiber static strain sensor using Pound–Drever–Hall technique.* Optics letters, 2011. **36**(20): p. 4044-4046.

83. Haus, H.A., *Waves and fields in optoelectronics.* 1984: Prentice-Hall.

84. Yariv, A. and P. Yeh, *Photonics: optical electronics in modern communications.* Vol. 6. 2007: Oxford University Press New York.

85. Sun, X., H.-C. Liu, and A. Yariv, *Adiabaticity criterion and the shortest adiabatic mode transformer in a coupled-waveguide system.* Optics letters, 2009. **34**(3): p. 280-282.

86. Barwicz, T., et al., *Microring-resonator-based add-drop filters in SiN: fabrication and analysis.* Optics express, 2004. **12**(7): p. 1437-1442.

87. Sherwood-Droz, N., et al., *Optical 4× 4 hitless silicon router for optical networks-on-chip (NoC).* Optics express, 2008. **16**(20): p. 15915-15922.

88. Nitkowski, A., L. Chen, and M. Lipson, *Cavity-enhanced on-chip absorption spectroscopy using microring resonators.* Optics express, 2008. **16**(16): p. 11930-11936.

89. Lee, B.G., et al., *Beam combining of quantum cascade laser arrays.* Optics Express, 2009. **17**(18): p. 16216-16224.

90. Ryckeboer, E., et al., *Glucose sensing by waveguide-based absorption spectroscopy on a silicon chip.* Biomedical optics express, 2014. **5**(5): p. 1636-1648.

91. Subramanian, A.Z., et al., *Silicon and silicon nitride photonic circuits for spectroscopic sensing on-a-chip.* Photonics Research, 2015. **3**(5): p. B47-B59.

92. Ghosh, K.K., et al., *Miniaturized integration of a fluorescence microscope.* Nature methods, 2011. **8**(10): p. 871-878.

93. Trache, A. and G.A. Meininger, *Atomic force-multi-optical imaging integrated microscope for monitoring molecular dynamics in live cells.* Journal of biomedical optics, 2005. **10**(6): p. 064023-064023-17.

94. Xia, F., L. Sekaric, and Y. Vlasov, *Ultracompact optical buffers on a silicon chip.* Nature photonics, 2007. **1**(1): p. 65-71.

95. Dong, J., et al., *Ultrafast all-optical signal processing based on single semiconductor optical amplifier and optical filtering.* IEEE Journal of Selected Topics in Quantum Electronics, 2008. **14**(3): p. 770-778.

96. Jones, D.J., et al., *Carrier-envelope phase control of femtosecond mode-locked lasers and direct optical frequency synthesis.* Science, 2000. **288**(5466): p. 635-639.

97. Jones, R.J. and J.-C. Diels, *Stabilization of femtosecond lasers for optical frequency metrology and direct optical to radio frequency synthesis.* Physical review letters, 2001. **86**(15): p. 3288.

98. Magden, E.S., et al. *Laser frequency stabilization using pound-drever-hall technique with an integrated TiO 2 athermal resonator.* in *Lasers and Electro-Optics (CLEO), 2016 Conference on.* 2016. IEEE.

99. Thorlabs. *Longpass Dichroic Mirrors/Beamsplitters.* 2017.

100. Rasras, M.S., et al., *Demonstration of a tunable microwave-photonic notch filter using low-loss silicon ring resonators.* Journal of Lightwave Technology, 2009. **27**(12): p. 2105-2110.

101. Dong, P., et al., *GHz-bandwidth optical filters based on high-order silicon ring resonators.* Optics express, 2010. **18**(23): p. 23784-23789.

102. Doerr, C., et al., *Wideband arrayed waveguide grating with three low-loss maxima per passband.* IEEE photonics technology letters, 2006. **18**(21): p. 2308-2310.

103. Dwivedi, S., et al. *Coarse wavelength division multiplexer on silicon-on-insulator for 100 GbE.* in *Group IV Photonics (GFP), 2015 IEEE 12th International Conference on*. 2015. IEEE.

104. Qiu, M., et al., *Photonic crystal optical filter based on contra-directional waveguide coupling.* Applied Physics Letters, 2003. **83**(25): p. 5121-5123.

105. Qiang, Z., W. Zhou, and R.A. Soref, *Optical add-drop filters based on photonic crystal ring resonators.* Optics express, 2007. **15**(4): p. 1823-1831.

106. Winzer, P.J., M. Pfennigbauer, and R.-J. Essiambre, *Coherent crosstalk in ultradense WDM systems.* Journal of lightwave technology, 2005. **23**(4): p. 1734.

107. Xia, F., et al., *Ultra-compact high order ring resonator filters using submicron silicon photonic wires for on-chip optical interconnects.* Optics express, 2007. **15**(19): p. 11934-11941.

108. Luo, A.-P., et al., *Wavelength switchable flat-top all-fiber comb filter based on a double-loop Mach-Zehnder interferometer.* Optics express, 2010. **18**(6): p. 6056-6063.

109. Menchon-Enrich, R., et al., *Light spectral filtering based on spatial adiabatic passage.* Light: Science & Applications, 2013. **2**(8): p. e90.

110. Stanton, E.J., et al., *Multi-octave spectral beam combiner on ultra-broadband photonic integrated circuit platform.* Optics express, 2015. **23**(9): p. 11272-11283.

111. Snyder, A.W. and J. Love, *Optical waveguide theory.* 2012: Springer Science & Business Media.

112. Watts, M. and H. Haus, *Integrated mode-evolution-based polarization rotators.* Optics letters, 2005. **30**(2): p. 138-140.

113. Giuntoni, I., et al., *Tunable Bragg reflectors on silicon-on-insulator rib waveguides.* Optics express, 2009. **17**(21): p. 18518-18524.

114. Lu, Z., et al., *Wideband silicon photonic polarization beamsplitter based on point-symmetric cascaded broadband couplers.* Optics express, 2015. **23**(23): p. 29413-29422.

115. Jinguji, K., et al., *Two-port optical wavelength circuits composed of cascaded Mach-Zehnder interferometers with point-symmetrical configurations.* Journal of lightwave technology, 1996. **14**(10): p. 2301-2310.

116. Lu, Z., et al., *Broadband silicon photonic directional coupler using asymmetric-waveguide based phase control.* Optics express, 2015. **23**(3): p. 3795-3808.

117. Tien, P., *Light waves in thin films and integrated optics.* Applied optics, 1971. **10**(11): p. 2395-2413.

118. Tien, P., R. Ulrich, and R. Martin, *Modes of propagating light waves in thin deposited semiconductor films.* Applied Physics Letters, 1969. **14**(9): p. 291-294.

119. Ulrich, R. and R. Torge, *Measurement of thin film parameters with a prism coupler.* Applied Optics, 1973. **12**(12): p. 2901-2908.

120. Metricon, *Model 2010/M User Manual.* 2010: Metricon Corporation.